# Nachweis von Zuschauernukleonen im HERMES – Experiment

# Identification of Spectator Nucleons at HERMES

Den Naturwissenschaftlichen Fakultäten der
Friedrich–Alexander–Universität Erlangen–Nürnberg
zur
Erlangung des Doktorgrades

vorgelegt von
**Klaus T. Fiedler**
aus München.

Als Dissertation genehmigt von den Naturwissenschaftlichen Fakultäten der Universität
Erlangen–Nürnberg

# Contents

# Introduction

The investigation of the internal structure of matter is one of the focal points in particle physics research. Over the past three decades, deep–inelastic lepton–nucleon scattering has been proven as an important tool to gain experimental insight into the fundamental constituents of matter and their interactions. These complex measurements require the collaboration of international research teams and the design of technically sophisticated particle accelerators and detectors.

The HERMES experiment utilizes the HERA accelerator facility at the DESY research center in Hamburg to probe the spin structure of the nucleon, i.e. the way in which the total spin of the nucleon can be derived from the angular momenta of its constituents. To achieve this goal, several novel technologies, like an internal storage cell target and a longitudinally polarized electron beam in a high energy storage ring, had to be employed. As a result, the HERMES experiment allows a unique access to a multitude of physics processes, which also extend well beyond its initial program.

In this thesis, a new Silicon detector system is introduced, which is scheduled for installation in the vacuum of the HERMES target chamber in close proximity to the interaction point. This so–called HERMES *Recoil Detector* substantially extends the acceptance of the HERMES spectrometer and enables the tagging of exclusive reactions like deep virtual Compton scattering and diffractive meson production, thereby giving experimental access to the rapidly developing field of Off–Forward Parton Distributions. Furthermore, the possibility of particle identification and momentum reconstruction in the low–energy domain allows to detect spectator nucleons, which constitutes an unprecedented approach to the investigation of nuclear effects in deep–inelastic scattering.

The main focus of this thesis is on the detection of spectator nucleons at HERMES . To prove the feasibility of this challenging project, a fully functional detector prototype has been designed, installed and operated in the HERMES target chamber.

## Structure of the Thesis

The content of this thesis is structured in the following way:
Chapter 1 introduces the physics program and the experimental setup of the HERMES experiment. Subsequently, the advantages of an additional detector in the HERMES target region are presented for the tagging of exclusive processes as well as for the investigation of nuclear effects.

In Chapter 2, the boundary conditions for the installation of a detector in the specific vacuum environment at HERMES are presented, and the choice of a Silicon strip telescope is motivated. Using Monte Carlo simulations, the predicted detector response and the detection yield for different detector designs are described. Based on these calculations, the estimated statistical accuracy of the proposed measurements can be specified. Finally, a possible design for the implementation of the Recoil Detector into the HERMES experiment is shown.

To gain experience with the operation of a Silicon telescope in the environment of the HERMES target chamber, a small test detector was installed and operated during several months of regular HERMES data taking. Chapter 3 presents the design of this device and the initial tests that were carried out at the tandem accelerator at the University of Erlangen. Furthermore, the results of Monte Carlo simulations concerning the test detector response at HERMES are summarized.

The operation parameters of the test detector and the structure of the analysis chain developed to study the detector response are shown in Chapter 4. In the remaining part, the results of measurements with different target types are presented, together with the reconstruction of the relevant angular and momentum distributions and a summary of the conclusions.

# 1 Physics Motivation

In this chapter, the physics motivation for the proposed addition of the HERMES Recoil Detector to the HERMES spectrometer is described. Section 1.1 gives an overview of the physics program of the HERMES experiment and depicts the setup of the target and the spectrometer. The physics cases which would be newly or superiorly accessible with the implementation of the planned detector are highlighted in section 1.2.

## 1.1 The HERMES Experiment

The HERMES experiment is situated at the *Deutsches ElektronenSYnchrotron* (DESY) research center in Hamburg, Germany. It has been operational since 1995 and uses the 27.5 GeV electron/positron beam of the *Hadron–Elektron–Ringanlage* (HERA) collider for polarized deep–inelastic scattering off a gaseous internal target to determine the nucleon spin structure.

### 1.1.1 Deep Inelastic Scattering at HERMES

In the standard model of elementary particle physics, a nucleon can be treated as a system of fundamental constituents denoted as *quarks*, which are bound by the strong interaction via the exchange of *gluons*. The three quarks which determine the quantum numbers of the nucleon are described as *valence* or *constituent quarks* and carry only a small fraction of the nucleon mass. The remaining energy is assigned to the gluons, which split into virtual pairs of quarks and anti–quarks forming a cloud of *sea quarks*.

Since more than three decades, deep–inelastic lepton–nucleon scattering has been used as a powerful technique to analyse the substructure of the nucleon. Hereby, an incoming charged lepton interacts with a nucleon of mass $M$ via the exchange of a virtual photon with four–momentum $q$. The squared four–momentum transfer is defined as

$$Q^2 := -q^2 \, ,$$

while the energy transfer in the laboratory system is the difference of the lepton energy before and after the interaction,

$$\nu := E - E' \, .$$

In the case of *elastic* scattering, the unchanged invariant mass $W$ of the target nucleon leads to the relation

$$2M\nu - Q^2 = 0 \, ,$$

whereas the *inelastic* scattering process results in an invariant mass $W > M$, and therefore

$$2M\nu - Q^2 > 0 \, .$$

The inelasticity of a scattering process is thus given by the dimensionless *Bjorken scaling variable*

$$x := Q^2/2M\nu \, .$$

The internal composition of the nucleon can be described by two unpolarized structure functions $F_1(x, Q^2)$ and $F_2(x, Q^2)$, which are related to the experimentally accessible differential cross section by

$$\frac{d^2\sigma}{d\Omega dE'} = \left(\frac{d\sigma}{d\Omega}\right)_{\text{Mott}} \left[\frac{F_1}{M} \tan^2 \frac{\theta}{2} + \frac{F_2}{\nu}\right] \, .$$

Hereby, $\theta$ is the polar angle of the scattered electron, and $(d\sigma/d\Omega)_{\text{Mott}}$ describes the scattering cross section of a charged lepton on a point–like target with spin 0.

An intuitive interpretation of the structure functions is made possible by the so–called *quark–parton model*, which was introduced by Feynman [Fey:72] and Bjorken [Bjø:69, BP:69]. Under the assumption of point–like constituents (quarks) in the nucleon target, and with $Q^2 \gg M^2$, the scaling variable $x$ gives the fraction of the total target four–momentum $P$ the struck quark is carrying. $F_2$ can then be interpreted as the charge–weighted sum of the quark distribution functions $q_f(x)$

$$F_2(x) = x \sum_f z_f^2 \, q_f(x) \, ,$$

where $f$ denotes the different types (flavours) of quarks in the nucleon and $z_f$ is the corresponding charge in units of the elementary charge $e$. In the case of spin-$\frac{1}{2}$ partons, $F_1$ and $F_2$ are connected by the Callan–Gross relation

$$2xF_1(x) = F_2(x) \, .$$

While the quark–parton model predicts an independence of $F_2$ from $Q^2$ for point–like quarks, the small deviation (*scaling violation*) observed in the experimental data [NMC:97] can be understood by taking QCD effects like gluon radiation into account.

While $F_1(x)$ and $F_2(x)$ characterize the momentum distribution, the spin structure of a nucleon is given by the spin structure functions $g_1(x)$ and $g_2(x)$. In the quark–parton model, $g_1(x)$ can be related to the polarized quark distributions $\delta q_f(x)$ by

$$g_1(x) = \frac{1}{2} \sum_f z_f^2 \delta q_f(x) \, .$$

Hereby, $\delta q_f(x)$ is defined as the difference of the probability functions $q_f^+(x)$ and $q_f^-(x)$, which are a measure of the probability of finding a quark with flavour $f$ and momentum fraction $x$ with a spin orientation parallel (+) and antiparallel (-) to the nucleon spin:

$$\delta q_f(x) = q_f^+(x) - q_f^-(x) \, .$$

The spin contribution of a quark of flavour $f$ to the total nucleon spin is then given by

$$\Delta q_f = \int_0^1 [\delta q_f(x) + \delta \bar{q}_f(x)] \mathrm{d}x \, .$$

In the early phase of the nucleon substructure analysis, it was assumed that the total nucleon spin $s_z^N = \frac{1}{2}$ originates from the spins $\Delta q_v$ of the three valence quarks. However, experimental data [EMC:88] indicated a distinct deviation from this prediction. From the measurements, the valence quark contribution was extracted to a value commensurate with zero, and many efforts were made to solve the resulting *spin crisis*. It has been shown that additional contributions from the sea quarks ($\Delta q_s$), the gluons ($\Delta G$) and the orbital angular momenta of quarks ($L_z^q$) and gluons ($L_z^g$) have to be considered to describe the nucleon spin $s_z^N$:

$$s_z^N = \frac{1}{2} = \frac{1}{2} \left( \Delta q_v + \Delta q_s \right) + \Delta G + L_z^q + L_z^g.$$

The main goal of the HERMES experiment is the high–precision measurement of these spin contributions.

To gain experimental access to the spin structure of the nucleon by means of deep–inelastic scattering, it is necessary to carry out measurements with a longitudinally polarized lepton beam and target. The spin dependent part $\Delta \sigma$ of the cross section can then be expressed in terms of $\Delta \sigma_\parallel$ and $\Delta \sigma_\perp$, where $\Delta \sigma_\parallel$ is the difference in cross section for parallel and anti–parallel spin orientation of lepton and target, and $\Delta \sigma_\perp$ likewise for perpendicular spin orientation of the target. The polarized structure functions $g_1(x, Q^2)$ and $g_2(x, Q^2)$ can then be calculated from the measured cross section asymmetries $A_\parallel$ and $A_\perp$.

For the experimental determination of the structure functions, solely the kinematics of the scattered lepton have to be measured. With these so–called *inclusive* measurements, the HERMES experiment has extracted the proton spin structure function $g_1^p$ [HERMES:98d] and the neutron spin structure function $g_1^n$ [HERMES:97a]. Furthermore, the inclusive data were used to determine the difference in the virtual photon cross section for the proton and the neutron [HERMES:98a].

One of the outstanding features of the HERMES spectrometer (see next section) is the ability to detect and identify part of the hadronic final state of the scattering process. These *semi–inclusive* measurements allow the investigation of several physics quantities which would otherwise be unaccessible. Some examples are the flavour asymmetry of the light sea quarks [HERMES:98b], the nuclear transparency measured in the exclusive production of $\rho$–mesons [HERMES:99c] and the polarized quark distribution functions

[HERMES:99b]. Further measurements include the asymmetry in the production of $\rho$-mesons [HERMES:00a] and the photoproduction of hadrons with high transverse momenta [HERMES:00c], which for the first time enabled a determination of the polarized gluon polarization $\Delta G$.

Using the HERMES data from unpolarized nuclear targets, the cross section ratio $\sigma_N/\sigma_D$ at small $x$ was found to be significantly smaller than expected [HERMES:00b]. This deviation, which can be interpreted as a dependency of the ratio $R = \sigma_L/\sigma_T$ on the nuclear medium, is still theoretically unexplained and referred to as the *HERMES effect*.

A detailed description of the HERMES physics program can be found in [HER:90, Due:95, HER:00].

## 1.1.2   Experiment Setup

The technical setup of the HERMES experiment can be divided into three major components: the polarized lepton beam, the polarized internal gaseous target and the spectrometer, which allows to detect the scattered lepton as well as part of the hadronic final state. An overview of these components is presented in the following.

### The Lepton Beam

The HERMES experiment is one of the four experiments installed at the HERA electron–proton collider (see figure 1.1) at DESY, which stores electrons[1] of 27.5 GeV and protons of 920 GeV in a bunched structure. Two of the other experiments, H1 and ZEUS, investigate collisions of the two beams, while the third, HERA–B, utilizes only the proton beam for fixed–target scattering. HERMES , on the other hand, uses only the electron beam with typical currents of 30–50 mA at injection.

As stated in section 1.1.1, the physics program of HERMES requires a longitudinally polarized lepton beam. Due to a spin–flip asymmetry in the emission of synchrotron radiation [ST:64], an electron beam in a storage ring can build up a transverse polarization. To achieve the desired longitudinal polarization, two sets of magnets installed in the front and the back of the HERMES interaction region rotate the spin into the longitudinal direction and back to transverse. The feasibility of this technique has been proven for the first time at HERA [B+:95], and polarizations of more than 50 % are routinely reached. Two polarimeters serve the purpose of measuring the transverse and longitudinal polarization.

### The Internal Target Cell

As the HERMES experiment uses the electron beam of a storage ring, it is necessary to install a target which minimizes the distortion of the beam while still providing a sufficient

---

[1]HERA is capable of storing electrons as well as positrons. In the following text, the term electrons denotes both possibilities.
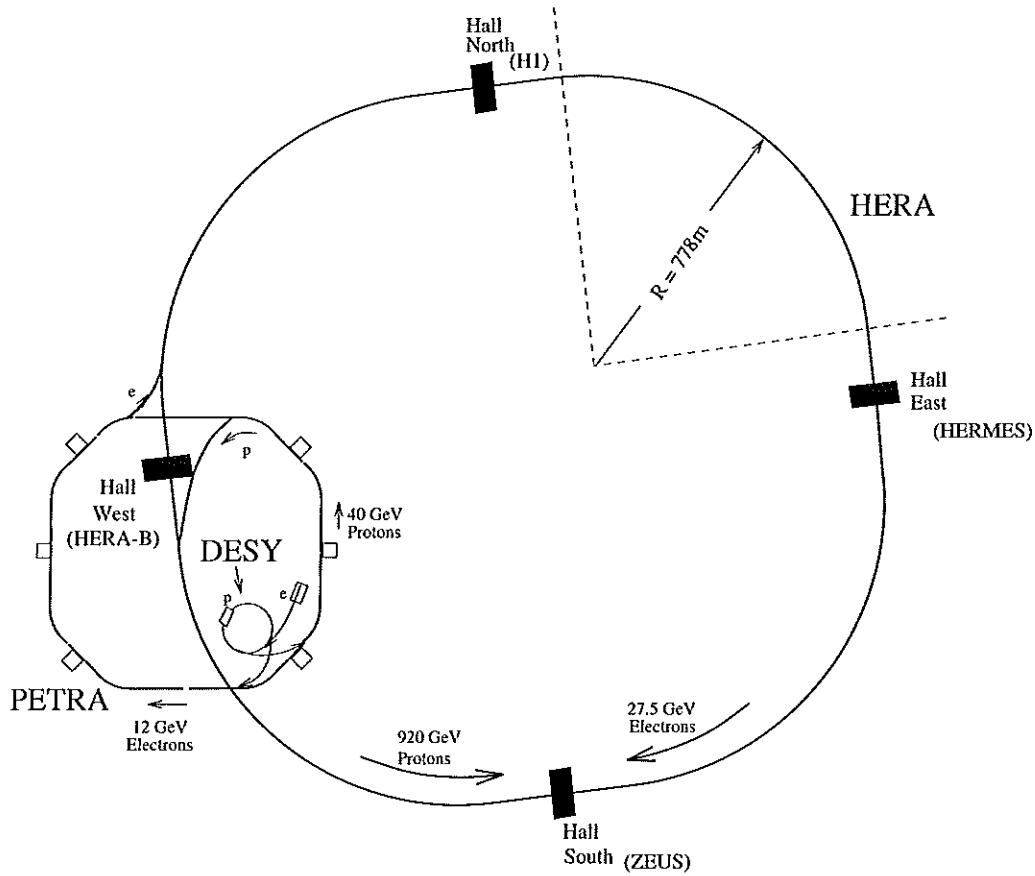
**Figure 1.1:** Schematic top view of the HERA accelerator.

target density. For this purpose, the novel technique of a storage cell has been employed, which increases the achievable target densities by two orders of magnitude as compared to those reachable with a gas jet target. Furthermore, in contrast to solid state targets, a high polarizability of the target material can be realized. The available targets include polarized atomic Hydrogen, Deuterium, $^3$He and, for the case of unpolarized measurements, also heavier nuclei like Nitrogen and Krypton.

With the storage cell technique, the beam passes through a thin–walled, open–ended tube into which the target atoms are injected. The advantage lies in an increased residence probability of the target atoms in the interaction region, resulting in increased target densities as compared to jet targets. In the case of polarized targets, the polarization is sustained by a special coating of the cell walls and a magnetic holding field [HERMES:99a]. Strong vacuum pumps at both ends of the cell ensure that the storage ring vacuum is not deteriorated. As all scattering products have to pass the storage cell wall, it is kept as thin as possible to minimize the impact.

target gas (H, D, He, ...)

e beam

ρ

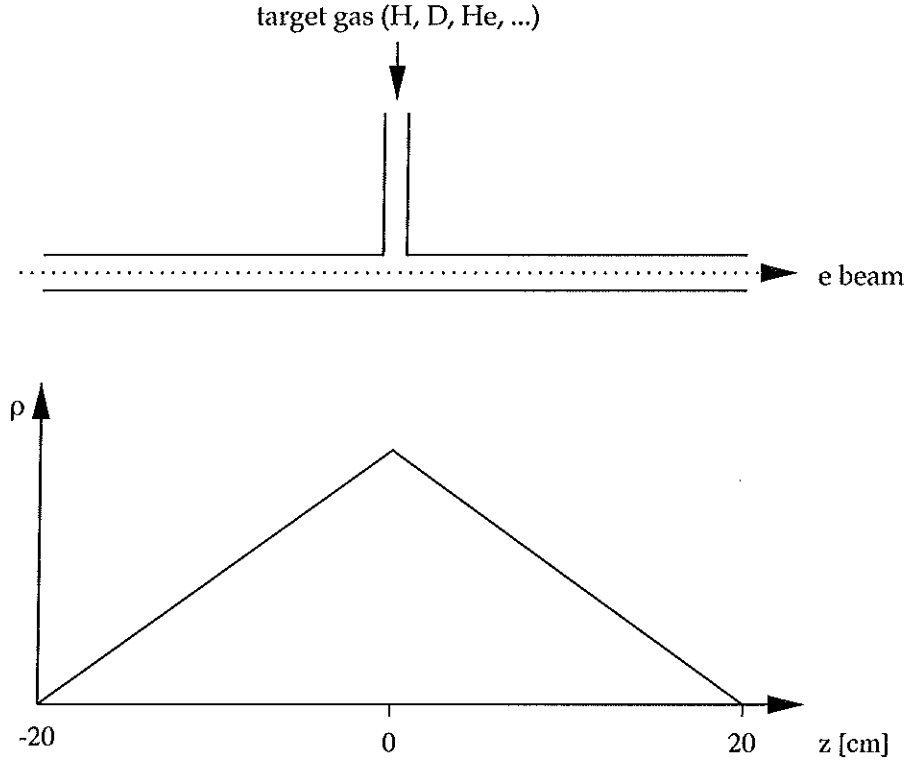-20                           0                        20      z [cm]

Figure 1.2: Schematic design of the HERMES storage cell. On the top, a side view of the cell is shown, while the bottom graph depicts the density distribution.

In the top part of figure 1.2, a side view of the schematic design of the HERMES storage cell is shown. The cell consists of an elliptical aluminum tube ($\sigma_x = 1.46$ cm, $\sigma_y = 0.50$ cm) with a wall thickness of 75 $\mu$m and a total length of 40 cm. As the target atoms are injected at the center of the cell, the target density $\rho$ peaks at $z = 0$ and drops linearly to both ends (see bottom part of figure 1.2)[2]. For longitudinal polarized operation, a magnetic holding field of 350 mT is applied along the $z$-direction.

Since 1996, an atomic beam source (ABS) has been used at HERMES to provide polarized Hydrogen and Deuterium targets at typical densities of $\rho_H = 7 \cdot 10^{13}$ nucleons/cm$^2$ and $\rho_D = 1 \cdot 10^{14}$ nucleons/cm$^2$. However, the limit imposed by electron beam life time considerations is more than an order of magnitude higher, which means that dedicated unpolarized measurements can be carried out at a significantly increased luminosity. Densities of up to $10^{17}$ nucleons/cm$^2$ have been used in this case. Typical values for unpolarized operation are $\rho_H = 1 \cdot 10^{15}$ nucleons/cm$^2$ for Hydrogen and

---

[2]All positions are given in a right-handed coordinate system with the $z$-axis along the electron beam direction and $z = 0$ at the center of the target cell.

$\rho_D = 2 \cdot 10^{15}$ nucleons/cm$^2$ for Deuterium.

## The Spectrometer

The HERMES spectrometer [HERMES:98c], which is shown in a three-dimensional view in figure 1.3, is designed to identify the scattered electron as well as the particles generated in the interaction, and to measure their corresponding momenta. It consists of two symmetrical parts positioned above and below the HERA beam lines. The electron beam line passes through the middle of the detector, while the proton beam line runs parallel at a distance of $\Delta x = 71.4$ cm. The acceptance of the spectrometer is optimized for the detection of particles scattered in the forward direction, with 40 mrad $< |\theta_y| < 140$ mrad in the vertical and $|\theta_x| < 170$ mrad in the horizontal direction.

Figure 1.3: Three–dimensional view of the HERMES spectrometer.

The individual components of the HERMES spectrometer are illustrated in figure 1.4. The detector systems are divided into a front and a back region by the spectrometer magnet, which produces a dipole field with an integrated magnetic flux of 1.3 Tm. In both

Luminosity Monitor

Calorimeter

Hodoscope H2
(Preshower)

TRD

Hodoscope H1

BC4

BC3

RICH

BC2

BC1

MC3

MC2

Magnet

MC1

FC2

FC1

Hodoscope H0

DVC

VC1/2

Target

8000 mm

7000

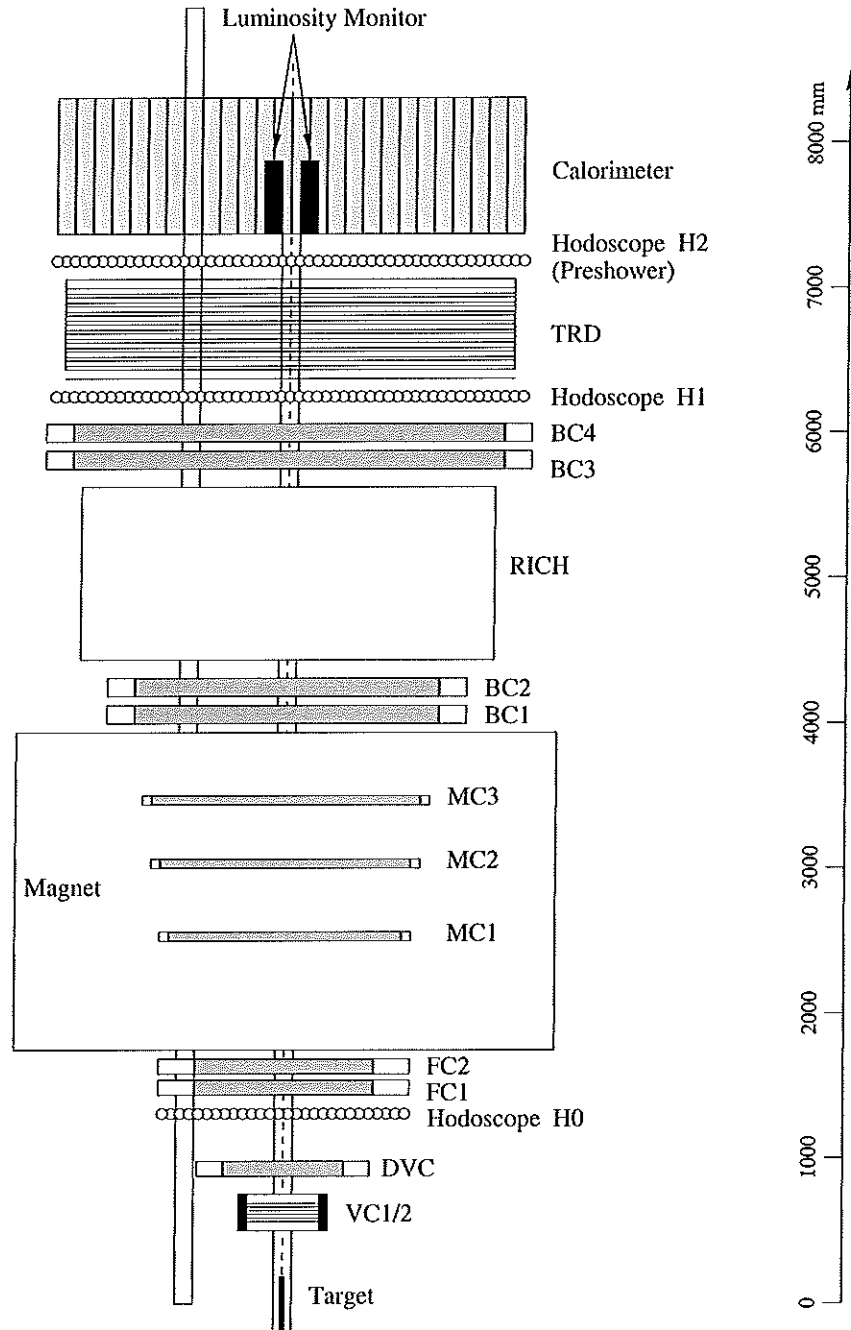6000

5000

4000

3000

2000

1000

0

Figure 1.4: Schematic top view of the HERMES spectrometer.

regions, several sets of tracking detectors determine the position of the traversing particle. Directly after the target region, a set of high–resolution micro–strip gas chambers (VC 1/2) is installed, with two drift chamber systems (DVC and FC 1/2) completing the tracking in the front region. Inside the magnet, three proportional chambers (MC 1–3) provide the link to the back region track, which is measured using further drift chambers (BC 1/2 and BC 3/4). A new set of silicon strip tracking devices (Lambda Wheels), which is scheduled for installation inside the target chamber vacuum, will substantially increase the acceptance for slowly decaying particles like the $\Lambda^0$ hyperon.

Along with the tracking chambers, a set of detectors in the back region provide for the identification of the scattered particles. A newly installed ring imaging Čerenkov counter (RICH) enables the identification of hadrons over almost the full energy range encountered at HERMES , while a transition radiation detector (TRD) allows to distinguish between electrons and hadrons. The lead glass calorimeter determines the energy deposition of a particle and, together with the pre–shower hodoscope (H2), further improves the electron–hadron separation. In total, an electron identification efficiency of 98 % with a hadron contamination of less than 1 % is reached. Two small calorimeters measure the coincidence rate of electron pairs produced by Møller scattering off the target atoms, thereby determining the luminosity.

The HERMES trigger electronics ensure the suppression of background signals and irrelevant events. While several different signal combinations can represent a valid event, the main HERMES trigger consists of correctly timed signals in the three hodoscopes (H0, H1, H2) and an above–threshold signal ($E > 3.5$ GeV) in the calorimeter. After the reception of a trigger signal, the HERMES data acquisition (DAQ) stores the event information for subsequent reconstruction and analysis. Hereby, the collected data is divided into so–called *runs*, which correspond to roughly $10^5$ triggered events.

## 1.2 Additional Acceptance in the Target Region

As outlined in section 1.1, the acceptance of the HERMES experiment is optimized for deep–inelastic scattering off a fixed target, i.e. for the detection of forward–going leptons and hadrons. However, many semi–inclusive and exclusive measurements would greatly benefit from the simultaneous detection of hadrons at larger angles. By installing an additional detector in the HERMES target region close to the storage cell, the signature of several physics processes would be improved, thereby allowing access to reactions which are beyond the current capabilities of the HERMES spectrometer. As many of these measurements involve the detection of a recoiling target nucleon, the proposed detector is referred to as the HERMES *Recoil Detector*.

The measurements described in this section require the detection of particles over a broad range in angle and momentum. Especially for low–energy scattering products, it is of high importance to minimize the amount of material between the interaction region and

the detector to avoid energy straggling or absorption. While these low–energy particles remain undetectable with a solid state target, the HERMES technique of using a thin–walled storage cell with a low–density gas target permits the installation of a detector inside the vacuum chamber, thereby giving access to the detection of particles with energies of only a few MeV. Furthermore, the solid angle is maximized by positioning the device as close as possible to the interaction region.

In the following, the two major physics cases which would benefit from the installation of the HERMES *Recoil Detector* are presented. Section 1.2.1 describes the process of diffractive vector meson production and its relation to the concept of off–forward parton distributions (OFPDs). Subsequently, the impact of nuclear effects in deep–inelastic scattering and its verification via the measurement of spectator nucleons is explained in section 1.2.2.

## 1.2.1   Exclusive Vector Meson Production and OFPDs

### Diffractive Vector Meson Production and Recoil Detection

In deep–inelastic charged lepton–nucleon scattering, the lepton interacts with the target via the exchange of a virtual photon $\gamma^*$. Instead of a direct coupling to the nucleon constituents, the photon can fluctuate into a virtual hadronic $q\bar{q}$ state with four–momentum $v$ and photon quantum numbers, i.e. into a vector meson with spin 1. In the Vector Meson Dominance Model (VDM) [Sak:60], the scattering process can then be described as a hadron–hadron interaction of a superposition of the lightest vector mesons ($\rho$, $\omega$, $\phi$) with the nucleon (see figure 1.5). During the interaction, the vector meson is shifted on its mass shell and is found in the final state of the reaction. The process is therefore denoted as *diffractive*[3] vector meson production (see [For:96] for a summary).

The cross section of the diffractive vector meson production is mainly dependent on the four–momentum transfer $t$ to the nucleon, which is given by

$$t := (q - v)^2 .$$

In the lab frame, the energy transfer $\Delta E$ to the target can then be expressed as

$$\Delta E = \nu - E_v + \frac{t}{2M} ,$$

where $E_v$ is the energy of the vector meson.

By means of the energy transfer $\Delta E$, the final states of diffractive vector meson production can be divided into two groups. In the first case, the invariant mass of the target

---

[3]The term *diffractive* results from the similarities in the angle and energy dependence of the cross section for hadron–hadron scattering and diffraction in classical optics.
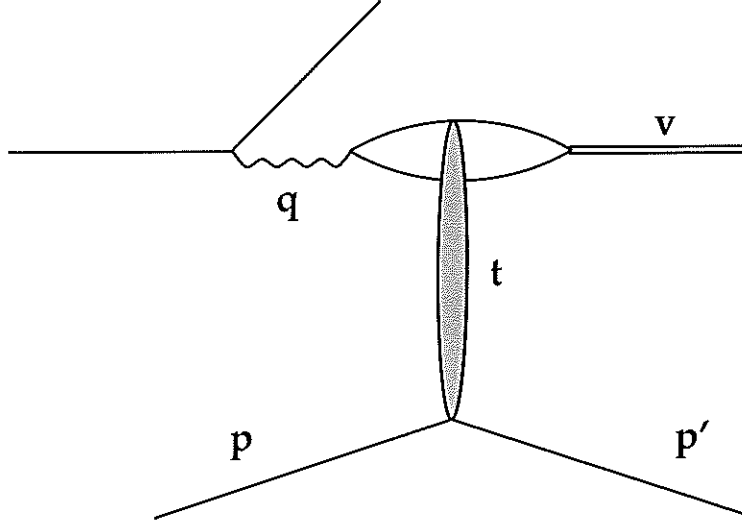
**Figure 1.5:** Schematic graph of diffractive vector meson production.

nucleon remains unchanged ($\Delta E \approx 0$), i.e. the target final state consists of a nucleon recoiling without excitation. This process is denoted as *exclusive* or *elastic* diffractive vector meson production,

$$e + p \to e' + v + p' .$$

If the recoiling nucleon is excited or broken up ($\Delta E > 0$), the process is called *inelastic* diffractive vector meson production,

$$e + p \to e' + v + X .$$

The hadron identification capabilities of the HERMES spectrometer allow, besides the detection of scattered leptons, to also measure reactions with a hadronic final state. In the case of diffractive scattering, the produced vector mesons can be observed in the HERMES experiment by means of identifying their corresponding decay products. As it will be outlined later in this section, the comparison of the measured cross sections with theoretical predictions requires a clear separation of elastic and inelastic processes. Since the recoiling nucleon is unobserved at HERMES, this is achieved by applying a kinematical cut on $\Delta E$. However, there remains a background contribution from DIS fragmentation processes, which has to be estimated and subtracted using Monte Carlo methods [HERMES:00a]. Figure 1.6 shows the measured spectra of the missing energy $\Delta E$ for $\rho^0$ production off $^1$H in comparison to Monte Carlo simulations of the background. As the calculations do not include inelastic nucleon excitations or internal radiative effects for the exclusive channel, the region $0.5\,\text{GeV} < \Delta E < 2.5\,\text{GeV}$ is not properly described.
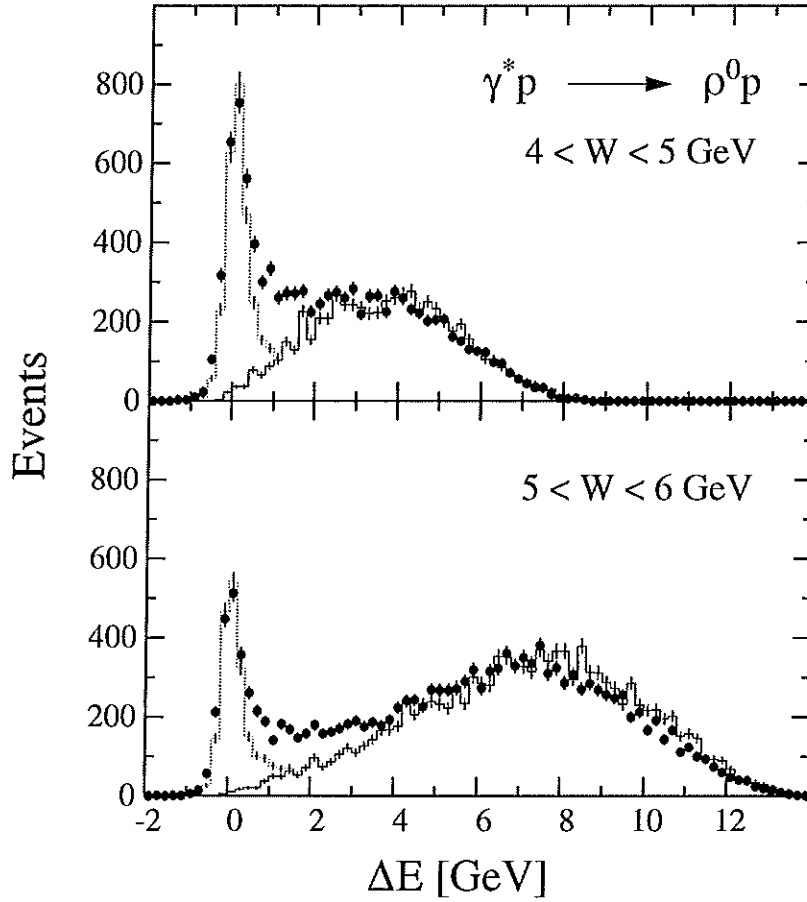
Figure 1.6: Missing energy spectra for $\rho^0$ production off $^1$H at HERMES for two different $W$ ranges [HERMES:00a]. The histograms show a Monte Carlo simulation of the background without (solid) and with (dotted) the inclusion of exclusive $\rho^0$ production.

In the exclusive diffractive process, the reaction can be treated as the elastic scattering of the vector meson with the target nucleon, i.e. a clear correlation exists between the kinematics of the outgoing vector meson and the recoiling nucleon. The range in momentum and angle of recoil nucleons corresponding to a detected vector meson in the HERMES acceptance is shown in figure 1.7 for the cases of $\rho$– and $J/\Psi$–production. It can be observed that the bulk of the recoil nucleons occur at large angles outside the acceptance of the HERMES spectrometer, and therefore cannot be used for the identification of an elastic process.

However, this situation can be improved with the installation a HERMES *Recoil Detector*, which due to its proximity to the target cell covers a large solid angle outside the HERMES spectrometer acceptance. Since the vector meson and the recoil nucleon occur in
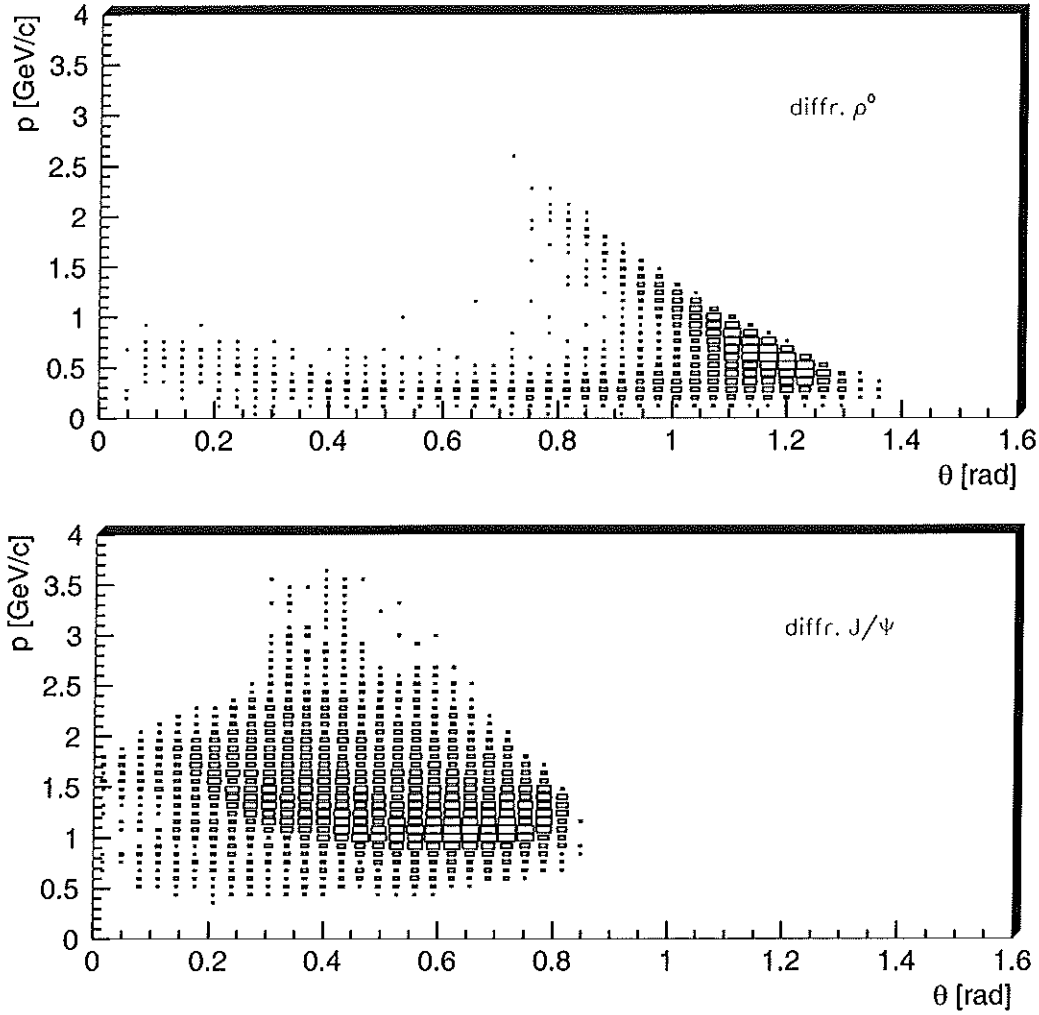
**Figure 1.7:** Correlation of angle and momentum for recoil nucleons in elastic diffractive vector meson production.

one geometrical plane, even the additional detection of the recoil vertex alone results in a clean signature for an exclusive diffractive event. Thus, the complete final state of elastic diffractive vector meson production is accessible, and a truly exclusive cross section can be obtained. Moreover, the yield of diffractive vector meson events will be increased substantially, as they can be identified by detecting the recoil nucleon and only one of the meson decay products.

In the following, the large physics potential of these measurements is motivated by outlining an experimental access to the gluon spin contribution through $J/\Psi$ production and to the so-called *Off-Forward Parton Distributions* through deep virtual Compton scat-

tering and $\rho^0$ production.

## $J/\Psi$ Production

The experimental access to the gluon contribution $\Delta G$ of the nucleon spin is very difficult to achieve in the HERMES energy domain. One of the processes with a clean signature and a reasonable analysing power is inelastic diffractive $J/\Psi$ production [VM:98], which is tagged using the electronic and muonic decay channels of the meson.

Basically, three production mechanisms contribute to the total cross section: *elastic* diffractive, *inelastic* diffractive and *non*–diffractive scattering. Unpolarized inelastic $J/\Psi$ production has for many years been successfully modelled by the Color Singlet Mechanism (CSM) [BJ:81], and a relation of the double spin asymmetry to $\Delta G$ can be calculated [Gui:88]. However, to be able to use the full diffractive event sample for the determination of the asymmetry, it is of crucial importance to establish the ratio of elastic to inelastic $J/\Psi$ production. As outlined in the previous section, the HERMES Recoil Detector allows to detect the complete final state of the vector meson production process, which results in a very clean distinction between the two contributions. Furthermore, the additional acceptance in the target region significantly increases the number of detectable $J/\Psi$ events.

The standard signature of a $J/\Psi$ event in the HERMES spectrometer is the detection of both leptonic decay products $J/\Psi \rightarrow l^+l^-$. However, this condition is only fulfilled for a small fraction of the total event sample. Using the additional information from a recoil proton in the HERMES Recoil Detector acceptance, a tagging of elastic $J/\Psi$ events with only one lepton track in HERMES acceptance can be realized. Detailed Monte Carlo studies [HERMES:97b] indicate that with the use of a Phase I HERMES Recoil Detector (see section 2.2.1), the total number of $J/\Psi$ events is thus increased by a factor of four.

## Off-forward Parton Distributions and DVCS

As described in section 1.1.1, a nucleon travelling with a velocity near the speed of light can be viewed as a beam of massless, noninteracting partons. The parton distributions introduced by Feynman can then be interpreted as number densities depending on the momentum fraction $x$ the parton carries. In its rest frame, however, the nucleon can certainly no longer be regarded as consisting of free partons. Up to now, a calculation of the distributions based on the fundamental theory of strong interaction, Quantum Chromo-dynamics (QCD), has not been achieved, as QCD in the low–energy domain involves an infinite number of degrees of freedom.

Recently, much attention has been put on a new theoretical concept of so–called skewed or *Off–Forward Parton Distributions* (OPFDs), which were first introduced almost two decades ago [BL:82, GLR:83] (see e.g. [dJ:98] for an introduction). These distributions constitute a generalization of those introduced by Feynman, since they reflect both the high- and the low–energy structure of the nucleon and are suitable to give a unifying description of

such different quantities like nucleon form factors and parton densities. However, most of the latest interest is based on the fact that OFPDs are also related to the spin structure of the nucleon and allow to determine the total angular momentum of quarks and gluons, $J_q$ and $J_G$ [dJ:97].
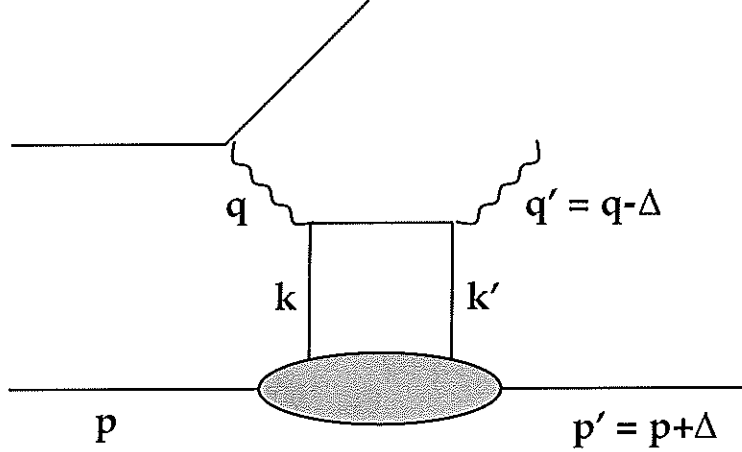


Figure 1.8: Schematic graph of deep virtual Compton scattering.

The concept of off–forward parton distributions can be illustrated by means of figure 1.8, which shows the process of Deep Virtual Compton Scattering (DVCS)[4]. A nucleon of momentum $p$ absorbs a virtual photon of momentum $q$ and produces an outgoing *real* photon of momentum $q' = q - \Delta$ together with a recoiling nucleon of momentum $p' = p + \Delta$, where $\Delta := p' - p = q - q'$ and $t := \Delta^2$. The usual parton distributions correspond to the forward case of $t = 0$, i.e. a parton is emitted from the nucleon with momentum $k$ and returned with the same momentum and spin. In the off–forward case of $t \neq 0$, however, the parton lines on the left and right side of the nucleon carry different momenta or spin, introducing an imbalance to the graph. This skewedness is expressed by the variable

$$\xi := \frac{-\Delta}{P+} ,$$

where $P+$ is the longitudinal light–cone component of the initial nucleon momentum[5]. Likewise, the longitudinal momentum fractions of the exchange partons are defined as

$$x := \frac{k}{P+} \quad \text{and} \quad x' := \frac{k'}{P+} .$$

Because of their dependence on the momentum transfer $\Delta$, the OFPDs contain two more scalar variables than the forward parton distribution; a common set is $x, \xi, t$ [dJ:97].

---

[4]Due to their characteristic shape, these diagrams are referred to as *handbag diagrams*

[5]For an introduction to the formalism of light–cone variables, see e.g. [Col:97].

For each quark flavour, the nucleon structure is then parameterized by four off–forward parton distributions: the spin–independent $H_q$ and $E_q$, and the spin–dependent $\tilde{H}_q$ and $\tilde{E}_q$. The large information content of the OFPDs is reflected in the fact that both the forward parton distributions and the nucleon form factors can be extracted. At $t \to 0$ and $\xi \to 0$, $H_q$ and $\tilde{H}_q$ reduce to

$$H_q(x, \xi \to 0, t \to 0) = q(x) \quad \text{and} \quad \tilde{H}_q(x, \xi \to 0, t \to 0) = \delta q(x) ,$$

while the first moments of the OFPDs are related to the elastic Dirac, Pauli, axial–vector and pseudo–scalar form factors

$$\int_{-1}^{1} dx\, H(x, \xi, t) = F_1(t),$$

$$\int_{-1}^{1} dx\, E(x, \xi, t) = F_2(t),$$

$$\int_{-1}^{1} dx\, \tilde{H}(x, \xi, t) = G_A(t),$$

$$\int_{-1}^{1} dx\, \tilde{E}(x, \xi, t) = G_P(t).$$

Since there is little experimental data on OFPDs, the above relations are important constraints for theoretical models.

Currently, the analysis of experimental data on the nucleon spin structure allowed the extraction of the spin content originating from quark and gluon spins, but not from orbital angular momenta. In the limit of $t \to 0$, the second moment of the sum of $E_q$ and $H_q$ is related to the total angular momentum of quarks $J_q$ [dJ:97]:

$$\lim_{t \to 0} \int_{-1}^{1} dx\, x\, [H_q(x, \xi, t) + E_q(x, \xi, t)] = J_q.$$

With the measurement of $E_q$ and $H_q$, it would therefore be possible to give a complete experimental determination of the nucleon spin structure.

## Experimental Access

The large physics potential of OFPDs has resulted in various theoretical studies investigating processes that are sensitive to the new distributions. Currently, the most promising types of experiments are DVCS, which depends on both the polarized and the unpolarized OFPDs, and diffractive meson production, which is sensitive to the unpolarized OFPDs in the vector meson channels and to the polarized OFPDs in the pseudo–scalar channels.

While model calculations exist for both processes [VGG:98, VGG:99], the DVCS reaction is difficult to observe because of the low cross section and the interference with the Bethe–Heitler amplitude. Meson production, on the other hand, has a clean experimental signature and a relatively high cross section. However, the QCD factorization of the scattering process in a hard scattering and a nucleon structure part only applies for longitudinally polarized vector mesons and requires the selection of purely exclusive events [CFS:97].

Again, the HERMES Recoil Detector can facilitate this task by detecting the recoiling target nucleon in addition to the decay products of the meson. The predicted accuracy can be illustrated by means of figure 1.9, which shows the predicted statistical error in the longitudinal cross section $\sigma_L$ for exclusive $\rho^0$ production in comparison to calculations based on the OFPD model [vdS:99]. The error bars are based on an integrated luminosity of 270 pb$^{-1}$ and a Phase I HERMES Recoil Detector (see section 2.2.1).
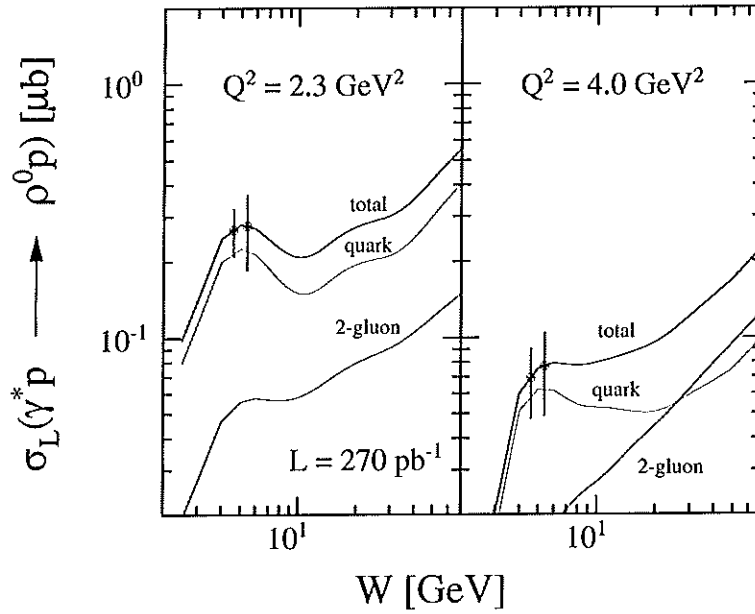


Figure 1.9: Longitudinal component of the exclusive diffractive cross section for $\rho^0$ production versus $W$ for two average values of $Q^2$ as accessible with the HERMES Recoil Detector. The solid lines represent the results of calculations based on the OFPD model [VGG:98] for the total cross section and the quark and 2–gluon contributions [vdS:99]. The error bars are based on a predicted integrated luminosity of 270 pb$^{-1}$.

## 1.2.2 Nuclear Effects

### Nuclear Corrections

Due to the lack of a free neutron target, the neutron structure function $F_2^n$ is usually measured by subtracting the data taken with $^2$H and $^1$H targets. To allow for the binding of the neutron in $^2$H, the evaluation of the structure function from the scattering data requires the application of nuclear corrections. While in general Fermi motion, binding and off-shell effects have to be considered, a standard correction method is for example the smearing algorithm by Bodek and Ritchie [BR:81a, BR:81b], which assumes a correspondence between the off-shell and the free structure function and considers only the Fermi motion of the neutron and proton.

These corrections are reasonably well under control for $x < 0.5$, but become questionable at higher $x$ as they depend strongly on the employed nuclear dynamics model. Consequently, the values of $F_2^n/F_2^p$ extracted in this region have a substantial model uncertainty [MT:96]. The experimental determination of this ratio in the limit of $x \to 1$ is of high theoretical interest, as several different predictions exist.

Under the simple assumption of SU(6) spin–flavour symmetry, the $u$ and $d$ quarks in the nucleon are identical apart from charge and flavour quantum numbers, and the neutron to proton structure function ratio amounts to $F_2^n/F_2^p = 2/3$. Since the same assumption also leads to e.g. identical masses for the nucleon and the $\Delta$ isobar, this prediction can however be neglected. In a perturbative QCD framework, $F_2^n/F_2^p$ should approach a value of 3/7 [BBS:95], while models based on the dominance of a scalar valence di–quark component $(ud)_{s=0}$ expect it to converge to 1/4 [Car:75]. Because of the relatively large nuclear corrections at high $x$, the existing data cannot distinguish between these conflicting predictions. Furthermore, theoretical developments suggest that off–shell effects in light nuclei cannot be neglected. This is demonstrated in figure 1.10, which shows the extraction of $F_2^n/F_2^p$ from the same recent SLAC data for the two different approaches. With the current method of applying nuclear corrections based on theoretical calculations only, it is not possible to distinguish between the different predictions for $x \to 1$.

Hence, it is desirable to obtain reliable measurements of $F_2^n$ at high $x$, which are less sensitive to the ambiguities in nuclear corrections. Given the experimental conditions at HERMES , this can be achieved by *tagging* the neutron structure function, i.e. by measuring the deep–inelastic scattering off a deuteron target with the simultaneous detection of the spectator proton, which constitutes the nuclear remnant:

$$e + {}^2\text{H} \to e' + p_{spec} + X .$$

In this so–called *spectator mechanism* [FS:81], the proton acts as a spectator in the scattering off the bound neutron and, due to momentum conservation, is emitted with the Fermi momentum of the $^2$H system. As it will be shown, this technique not only provides for a clean signature of the neutron scattering process, but allows to correct for nuclear effects
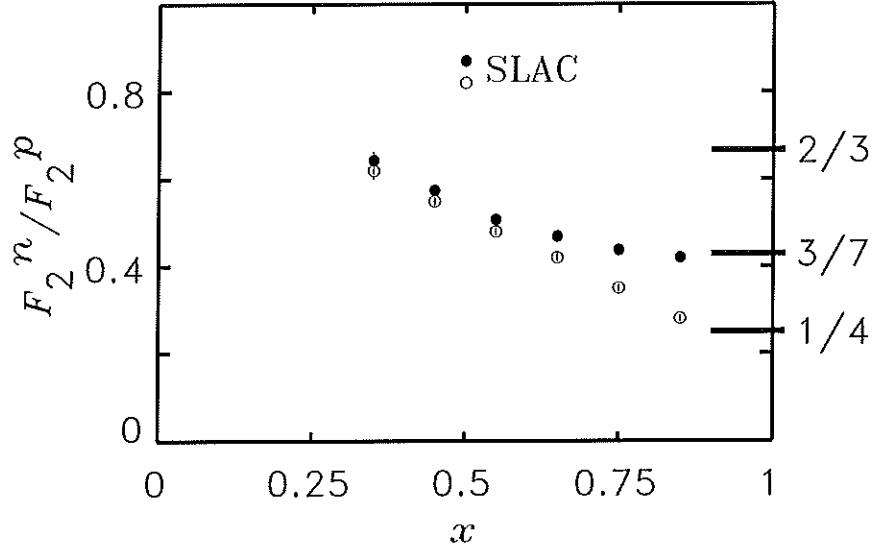
Figure 1.10: Extraction of $F_2^n/F_2^p$ from SLAC $^1$H and $^2$H data with (full circles) and without (open circles) accounting for off-shell effects [MT:96].

on an event–by–event basis by using the spectator kinematics as an additional experimental input.
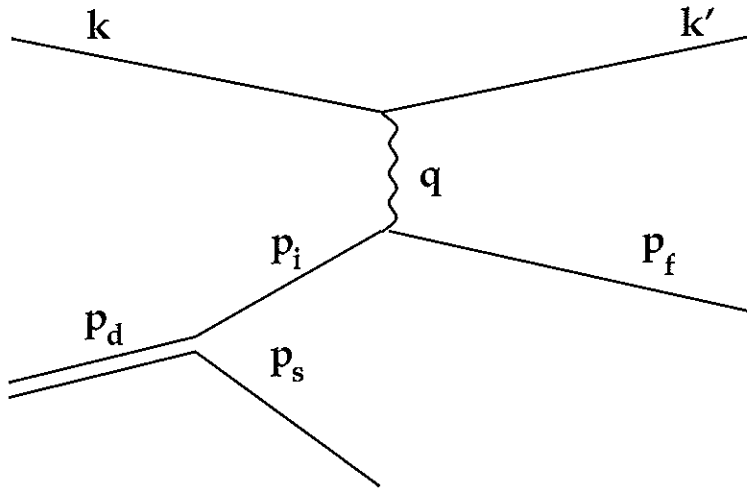


Figure 1.11: Feynman graph of the spectator mechanism in lepton–deuteron scattering.

The Feynman graph of the spectator mechanism in lepton–deuteron scattering is shown in figure 1.11. In the impulse approximation, the detected spectator nucleon with the four–momentum $p_s$ and the energy $E_s$ is on the mass shell and is totally unaffected by the

interaction, i.e.

$$p_s = (\mathbf{p}_s, E_s)$$
$$p_s^2 = m_p^2 .$$

To ensure energy and momentum conservation, the interacting nucleon with the four-momentum $p_i$ must therefore be off the mass shell, its invariant mass being less than the free nucleon mass:

$$p_i = (-\mathbf{p}_s, m_d - E_s)$$
$$p_i^2 = (m_d - E_s)^2 - \mathbf{p}_s^2 .$$

Compared to scattering off a free nucleon, the bound state of the struck nucleon does not change the momentum transfer $Q^2$, but affects the final state invariant mass $p_f^2$ and the quantity $p_f \cdot q$. This results in a shift of the Bjorken scaling variable $x$ to

$$x^* = \frac{Q^2}{Q^2 + p_f^2 - m_p^2}$$

or, in terms of experimentally accessible quantities,

$$x^* = \frac{Q^2}{Q^2 + (\nu + m_d - E_s)^2 - (\mathbf{q} - \mathbf{p}_s)^2 - m_p^2} .$$

In the Bjorken limit $Q^2 \rightarrow \infty$, the variable $x^*$ can be written in terms of the light–cone momentum fraction[6]

$$z_s = \frac{E_s - \mathbf{p}_s \cdot \hat{\mathbf{q}}}{m_p}$$

of the spectator nucleon as

$$x^* = \frac{x}{2 - z_s} .$$

Hereby, $\mathbf{p}_s \cdot \hat{\mathbf{q}}$ denotes the projection of the spectator momentum $\mathbf{p}_s$ on the dimensionless unit vector $\hat{\mathbf{q}}$ of the virtual photon.

Using this formalism, the cross section for tagging the neutron structure function using a deuterium target can be written as

$$\sigma_{tagging}(x, Q^2, p_s) \propto F_2^n \left( \frac{x}{2 - z_s} \right) |\psi(|\mathbf{p}_s|)|^2 .$$

---

[6]In publications, the variables $\alpha_s$ or $y$ are frequently used for describing the light–cone momentum fraction.

Hereby, $\psi(|\mathbf{p}_s|)$ essentially represents the nucleon wave function of the deuteron, with $|\psi(|\mathbf{p}_s|)|^2 \cdot \mathbf{p}_s^2$ being the resulting deuteron momentum density as shown in figure 1.12. In a non–relativistic approach, $\rho(|\mathbf{p}_s|) = |\psi(|\mathbf{p}_s|)|^2$ can be expressed in terms of the S– and D–state components of the deuteron wave function and has been mapped out with high precision by low–energy electron scattering experiments (see e.g. [B$^+$:81]).
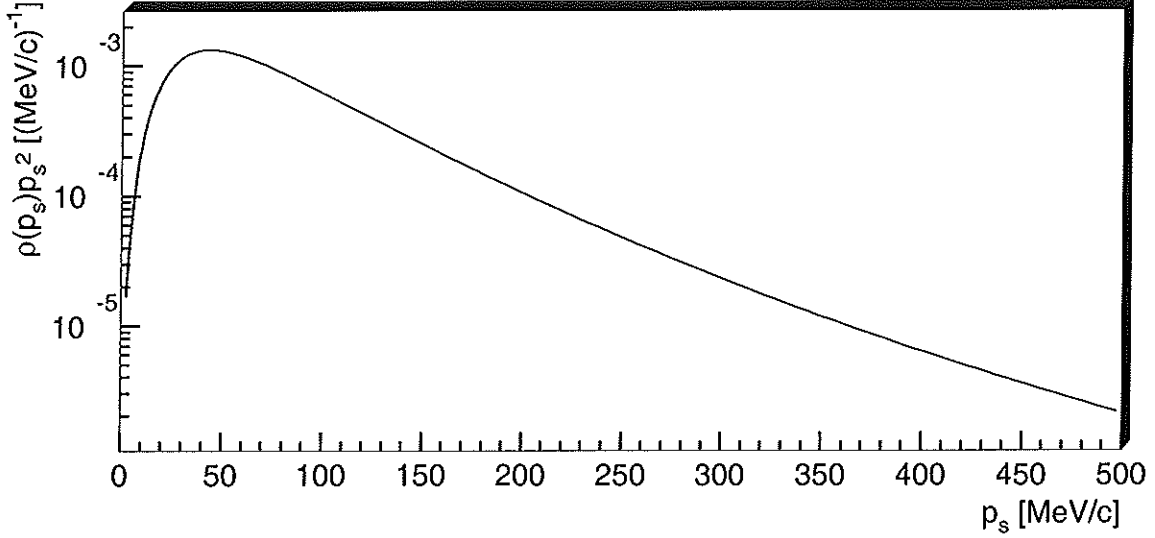


Figure 1.12: The deuteron momentum density $|\psi(|\mathbf{p}_s|)|^2 \cdot \mathbf{p}_s^2$ as a function of the spectator nucleon momentum [Kra:76].

The yield of a tagging experiment largely depends on the lower and upper limits in the integral

$$\int_{p_{min}}^{p_{max}} |\psi(|\mathbf{p}_s|)|^2 \, |\mathbf{p}_s|^2 \, \mathrm{d}|\mathbf{p}_s| \, ,$$

i.e. on the experimentally accessible spectator momentum range. In the case of the detection of spectator protons, the lower limit is set by detector and target parameters like e.g. the type and thickness of the used material. A detailed study on the achievable yield at HERMES can be found in section 2.2.

The feasibility of a tagged structure function measurement is closely related to the validity of the spectator mechanism. In [Sim:96a], this topic has been addressed in detail for the kinematics at CEBAF, i.e. for values of $Q^2$ which are lower than those reached at HERMES . While only minor violations of the spectator mechanism are expected, it is possible to check its validity by introducing a spectator scaling function

$$F^{(sp)}(x^*, Q^2, p_s) \equiv m_p |\mathbf{p}_s| n^{(D)}(|\mathbf{p}_s|) F_2^n(x^*, Q^2)/x^*$$

with $n^{(D)}$ being the nucleon spectral function in the deuteron.

At a fixed value of $p_s$, $F^{(sp)}$ only depends on $x^*$, i.e. different lepton and nucleon kinematics correspond to the same invariant mass produced on the struck nucleon. The scaling properties of $F^{(sp)}$ thereby allow an experimental observation of the dominance of the spectator mechanism. The breakdown of the spectator scaling due to relativistic effects determines the upper limit in the spectator momentum range, for which usually the start of the D–state dominance at $p_{max} \approx 300$ MeV/c is taken.

In summary, the simultaneous detection of the scattered lepton and a spectator nucleon allows a unique experimental insight into nuclear effects in deep–inelastic scattering off the deuteron. As an aside, it is mentioned that the the detection of spectator neutrons as a means of determining the proton structure function would, while experimentally complicated, enable a direct comparison between a free proton target and the bound deuteron system.

## EMC Effect in the Deuteron

The neutron–tagging technique described in the previous section can be extended to investigate the possible origin of the EMC effect [MSS:97], i.e. the observation of an $A$ dependence of the unpolarized structure function $F_2(x)$ [EMC:83]. This effect is approximately proportional to the nuclear density, and a wide range of models with very different underlying assumptions have been developed to describe the $x$ and the $A$ dependence. While the EMC effect is usually stated as the deviation relative to the deuteron structure function, an investigation of the theoretical models can also be achieved by tagged scattering off the deuteron.

Due to the low nuclear density in $^2$H, one should expect much smaller nuclear effects in deuterium compared to heavier nuclei. By using the tagging method, however, it is possible to isolate configurations of the two nucleons which correspond to high momenta and therefore to small distances. A further advantage of using a deuterium target is the clean signature of the tagging process, while with heavier nuclei secondary interactions and nucleon–nucleon correlations have to be taken into account [Sim:96a].

In [MSS:97], several theoretical approaches[7] for the EMC effect are presented together with the corresponding predictions for the tagged structure functions. The main differences between the models stem from different assumptions about the deformation of the bound nucleon wave function and the contribution of mesonic degrees of freedom. While *binding models* predict a dominance of the latter effect and an almost unchanged nucleon structure function [MST:94], the *rescaling model* assumes a more efficient gluon radiation in the bound nucleon due to quark delocalization [CRR:83, NP:84]; non–baryonic degrees of freedom play no role in this theory. A different approach is taken in [FS:88], where it is assumed that weakly interacting point–like 3–quark configurations (PLC) are the dominant contribution to the free nucleon structure function at large $x$. The *suppression of point–like*

---

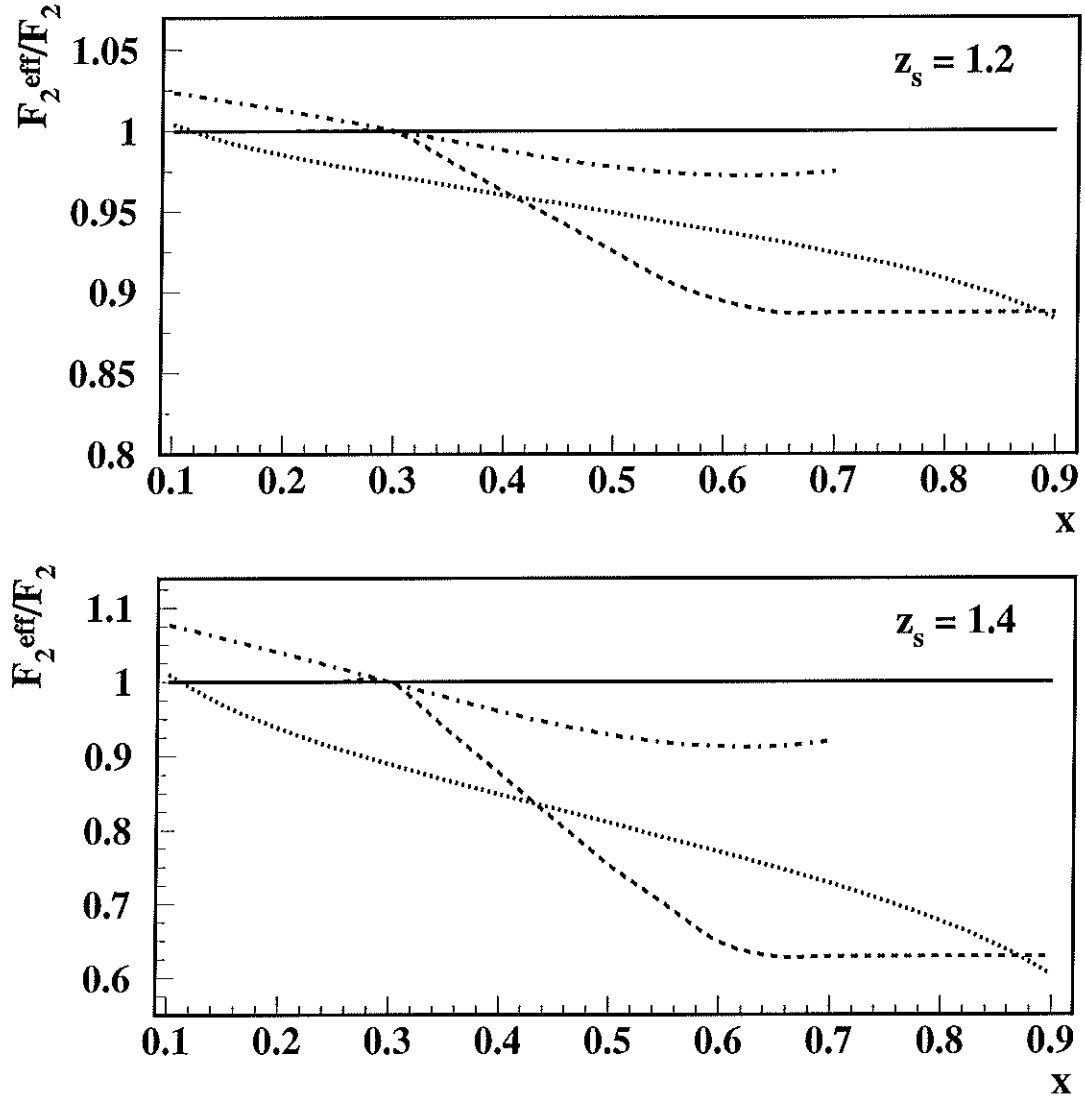[7]One major class of models not discussed in this summary are the six–quark cluster models [CLS:91, dAS:95].

Figure 1.13: The $x$–dependence of the ratio $F_2^{eff}(x)/F_2(x)$ at fixed $z_s$ for different models of the EMC effect [MSS:97].
*dashed:* PLC suppression
*dotted:* rescaling model
*dot–dashed:* off–shell model

*configurations* in the bound nucleon is then predicted to be the main source of the EMC effect.

The basic principle of the experimental verification of these models is the compari-

son of the neutron structure function $F_2^{eff}(x)$ at large light cone momenta $z_s$ to the free structure function $F_2(x)$. Figure 1.13 shows the predicted $x$–dependence of the ratio $F_2^{eff}(x)/F_2(x)$ for two fixed values of $z_s$. An alternative method of extracting the nuclear effects can be realized by observing the ratio

$$G^{eff}(z_s, p_s, x_1, x_2, Q^2) = \frac{F_2^{eff}(x_1/(2-z_s), p_s, Q^2)}{F_2^{eff}(x_2/(2-z_s), p_s, Q^2)} .$$

In this representation, the nuclear effects parameterized in the deuteron momentum distribution cancel, i.e. the measurement is not biased by a theoretical normalization of the deuteron wave function. The different theoretical predictions for $G(z_s)$ at fixed $x_1 = 0.2$ and $x_2 = 0.6$ are displayed in figure 1.14.

In summary, the selection of specific kinematical conditions in the measurement of tagged structure functions allows to distinguish between different theoretical models for the EMC effect. As the theoretical predictions are noticeably different, this new experimental insight will be valuable for understanding the origin of the EMC effect.

## Scattering off Heavy Nuclei

The previous discussions concerning the benefits of a HERMES Recoil Detector have been limited to the case of light target nuclei used for both polarized and unpolarized measurements. However, the HERMES target can also be operated with a wide range of unpolarized heavier nuclei, whereby the corresponding densities are only limited by electron beam life time considerations. Some of the applications of the recoil detector in scattering off heavy targets are presented in the following.

As described in the previous section, the experimental investigation of the reaction $^2H(e, e'p)X$ can be an effective tool to get information on the nuclear effects in the unpolarized structure function $F_2$. In [Sim:96b], an analogue approach to studying medium–dependent modifications in the process $A(e, e'p)X$ for $A > 2$ is presented.

In the interaction of a virtual photon with a nucleon of a correlated $NN$ pair, a recoiling spectator particle is emitted. The detection of this particle in the HERMES Recoil detector in coincidence with the observation of the scattered electron in the HERMES spectrometer again allows an event–by–event correction of the nuclear effects in the bound system. While the two–nucleon spectral function is not yet available for heavier nuclei in an exact form, realistic models taking into account the features relevant for the study of the semi–inclusive DIS process have been developed [dAS:95]. It is noted that due to center–of–mass motion of the correlated nucleon pair, the angular distribution is enhanced in the backward region.

An important application of the measurement of the spectator kinematics in DIS off heavy nuclei is the verification of several models describing the EMC effect. As an exam-
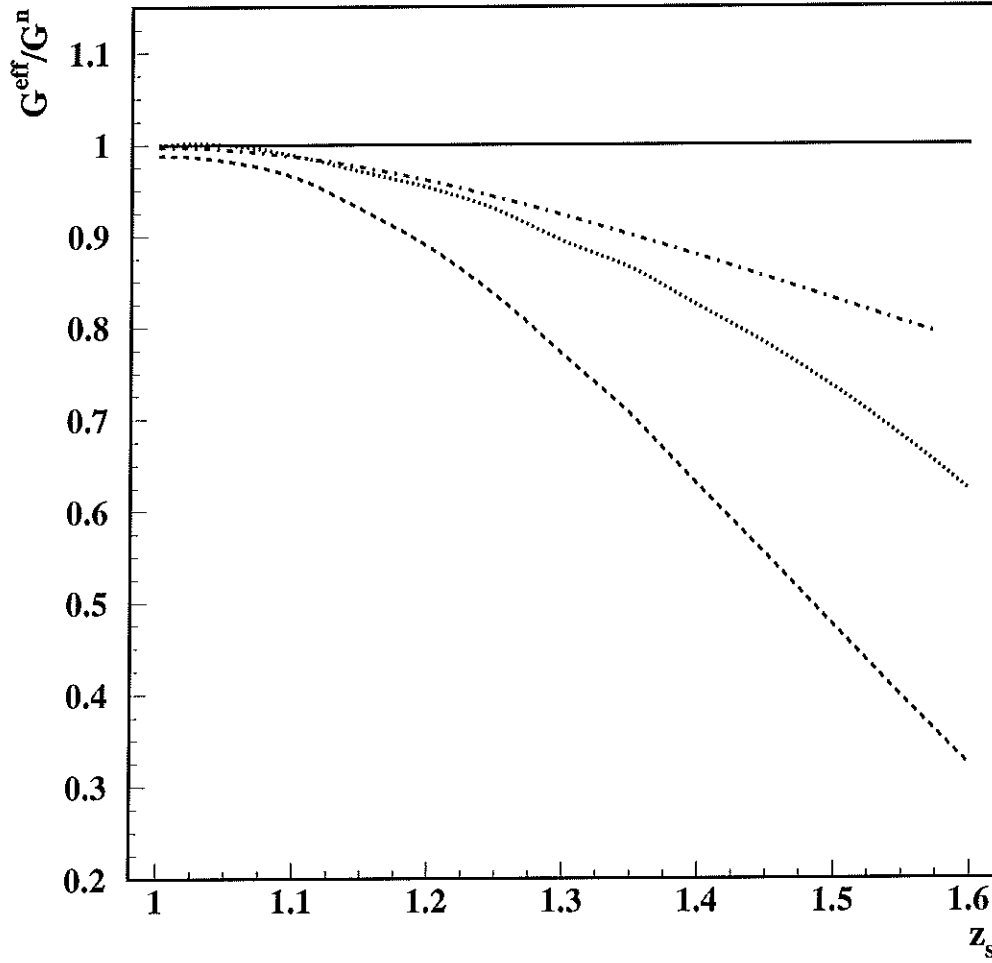
Figure 1.14: The $z_s$ dependence of $G^{eff}(z_s, p_s, x_1, x_2, Q^2)$ at fixed $x_1 = 0.2$ and $x_2 = 0.6$ for different models of the EMC effect [MSS:97]. $G^{eff}$ is normalized to the corrected neutron structure function ratio, i.e. to $G$ calculated with the free neutron structure function.
*dashed:* PLC suppression
*dotted:* rescaling model
*dot–dashed:* off–shell model

ple, figure 1.15 displays the ratio of the quantity

$$R_1(x_0, x, Q^2, \mathrm{p}_s) = \mathrm{d}^4\sigma(x, Q^2, \mathrm{p}_s) \,/\, \mathrm{d}^4\sigma(x_0, Q^2, \mathrm{p}_s)$$

for free and medium–modified structure functions based on the process $^{12}C(e, e'p)X$. Again, the ratio of the free to the medium–modified structure function shows a dependence on $x$ and $A$ which is distinct for each theoretical approach. Therefore, an unprecedented insight into nuclear effects in DIS can be achieved with the use of recoil detection
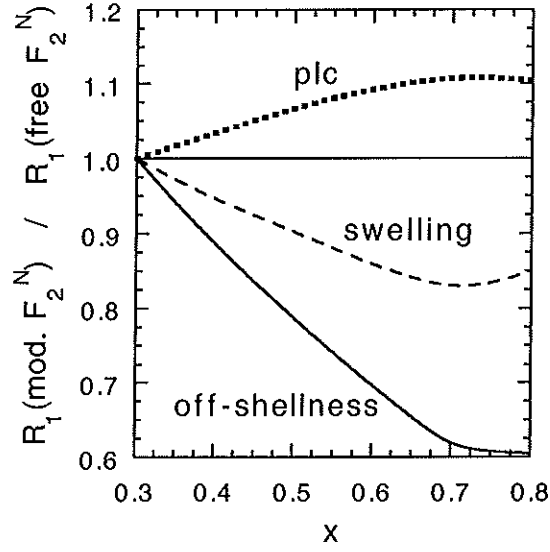
**Figure 1.15:** The ratio of the quantity $R_1(x_0 = 0.3, x, Q^2, p_s)$ calculated using free and medium–modified structure functions for different models of the EMC effect. The calculations are based on the process $^{12}C(e, e'p)X$ for $Q^2 = 10$ GeV, $p_s = 0.4$ GeV and backward spectator kinematics [Sim:96b].
*dotted:* PLC suppression
*dashed:* rescaling model
*solid:* off–shell model

at HERMES .

# 2 The HERMES Recoil Detector

In order to access to physics processes outlined in section 1.2, a detector has to feature certain capabilities, i.e.

- **tracking:** the reconstruction of the track of the registered particle

- **particle identification:** as far as possible, the determination of the particle type

- **energy / momentum reconstruction:** the determination of the particles energy / momentum.

The required detection of minimum ionizing particles (MIP) as well as low–momentum spectator nucleons requires a large dynamic range of the read-out system. As the latter particles cannot penetrate the beam pipe, it is necessary to mount the detector inside the vacuum of the HERMES scattering chamber. The special conditions inside the HERMES target vacuum vessel impose certain restrictions to the detectors design, i.e.

- **size:** the detector has to be compact enough to fit in between the wall of the HERMES target chamber and the storage cell. Furthermore, the acceptance of the HERMES spectrometer must not be obstructed.

- **UHV compatibility:** the detector has to be operational in an ultra high vacuum environment. In addition, the strict requirements of the HERA vacuum department concerning outgassing have to be met.

- **radiation hardness:** the detector and its read-out system have to tolerate the radiation and the RF field induced by the HERA electron beam.

- **reliability:** the HERMES spectrometer and especially the vacuum chamber cannot be accessed on a frequent basis. Therefore, the detector technology should be of proven reliability.

Taking these boundary conditions into account, it was decided to select a Silicon Telescope, i.e. a stack of Silicon detector layers, which will be mounted parallel to the HERMES storage cell. In the following, section 2.1 gives an overview of the concept of Silicon strip telescopes, while section 2.2 presents the results of Monte-Carlo simulations on the

expected detector performance and the background conditions. The corresponding statistical errors are shown in section 2.3. Section 2.4 eventually describes a possible design for the HERMES Recoil Detector.

## 2.1   Silicon Strip Telescopes

Since many years, Silicon detectors have found widespread applications in nuclear and high energy physics experiments. The high energy and position resolution, combined with the increasing availability of high-quality semiconductor material, make them an attractive choice, especially in areas with tight geometrical limits.
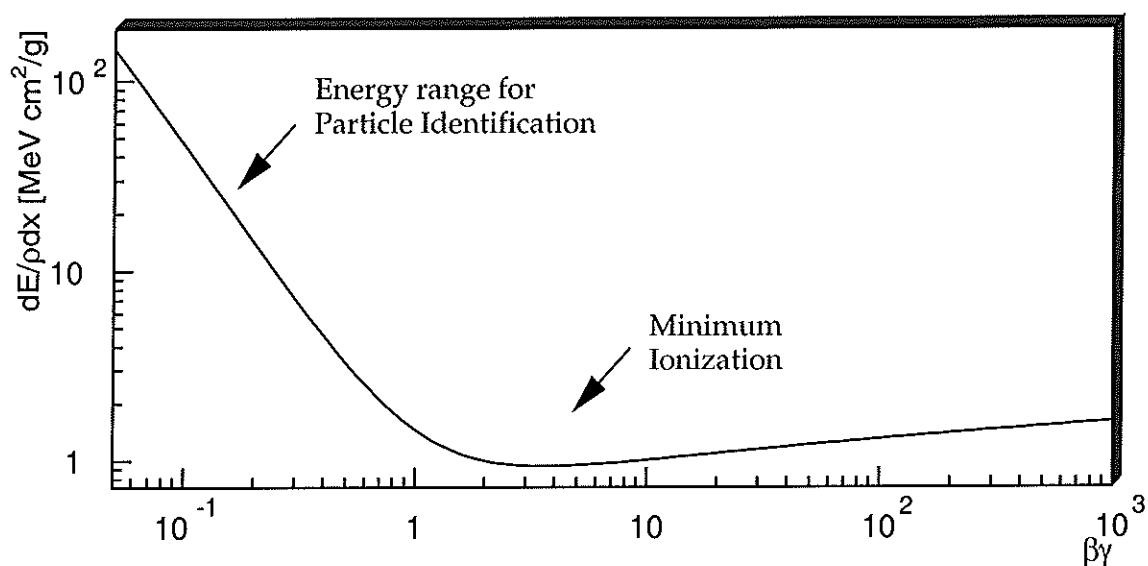


**Figure 2.1:** Schematic shape of the energy loss $S = dE/(\rho\,dx)$ of a charged particle in matter.

A Silicon detector can be described as a Silicon layer in which a $p$–$n$ transition is established parallel to the surface. By applying a reverse-bias voltage, the space charge region and therefore the active detector volume is maximized. For an impacting charged particle, two observables are experimentally accessible: the position and the energy deposition. The former is measured by dividing the detector into isolated strips on either one or, at an angle, both sides. The position resolution is then basically given by the strip pitch, which can be as low as several $\mu$m. As the particle passes through the Silicon layer, electron–hole pairs are created and separated in the space charge region. The current measured in this process is proportional to the energy deposition, which is therefore directly accessible once a detector calibration is established. However, for many physics applications it is necessary to determine the initial energy and the type of the observed particle.

The mean energy loss $S = dE/(\rho\,dx)$ of a moderately relativistic charged particle is mainly due to ionisation and can be described by the Bethe–Bloch equation [Par:96]. While $S$ depends on the properties of the particle as well as of the absorbing material, the basic shape, shown in figure 2.1 as a function of $\beta\gamma$, is conserved. For low particle energies, the energy loss drops steeply with the initial energy and reaches a broad minimum at about $\beta\gamma \approx 3$. Particles with energies corresponding to this minimum are usually referred to as *minimum ionizing particles* (MIP). As it will be explained in the following, the behaviour of $S$ at low energies can be utilized in measurements with Silicon telescopes to determine the type and initial momentum of low–energy charged particles.
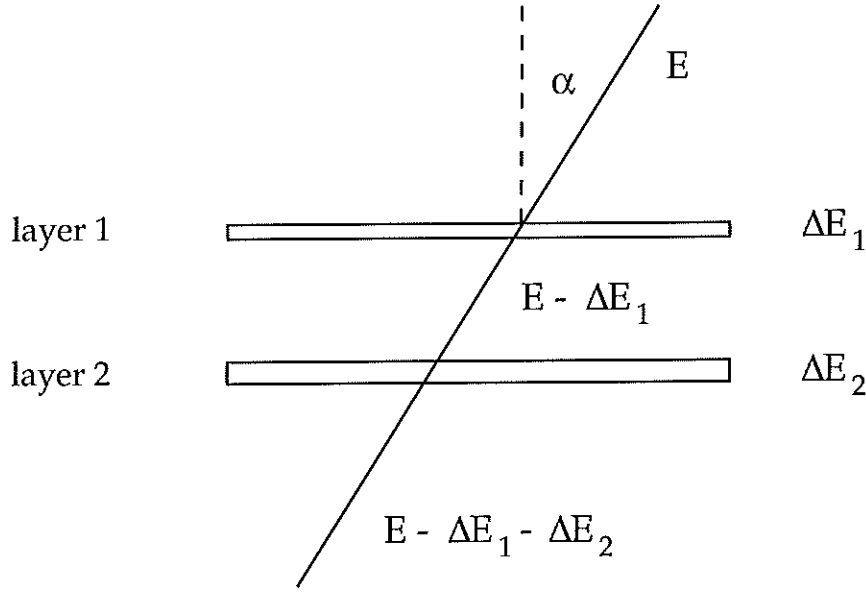


Figure 2.2: Energy deposition of a particle passing through a Silicon telescope.

A Silicon or $\Delta E$–$E$ telescope consists of a stack of two or more Silicon detector layers with usually different thickness. As depicted in figure 2.2, an impacting particle with the initial energy $E$ and an angle $\alpha$ relative to the detector surface will deposit the energy $\Delta E_1(E, \alpha)$ in the first layer, an energy $\Delta E_2(E - \Delta E_1, \alpha)$ in the second layer and so forth, until it is either stopped or passes the last layer of the telescope. This results in a dependence of $\Delta E_1$ on $\Delta E_2$ or, in general, $\Delta E_n$ on $\Delta E_{n+1}$, which is characteristic for each particle type. Therefore a particle identification for energies below minimum ionization can be performed. In the case of a MIP, it is still possible to determine the particle track.

Figure 2.3 shows the typical triangular shape of the energy deposition $\Delta E_2(E)$ versus $\Delta E_1(E)$. For low initial energies, the particle is stopped in the first layer and deposits its full energy (bottom horizontal line). With the increase of $E$, the *punch–through point* is reached, i.e. the particle passes the first layer and gets stopped in the second layer
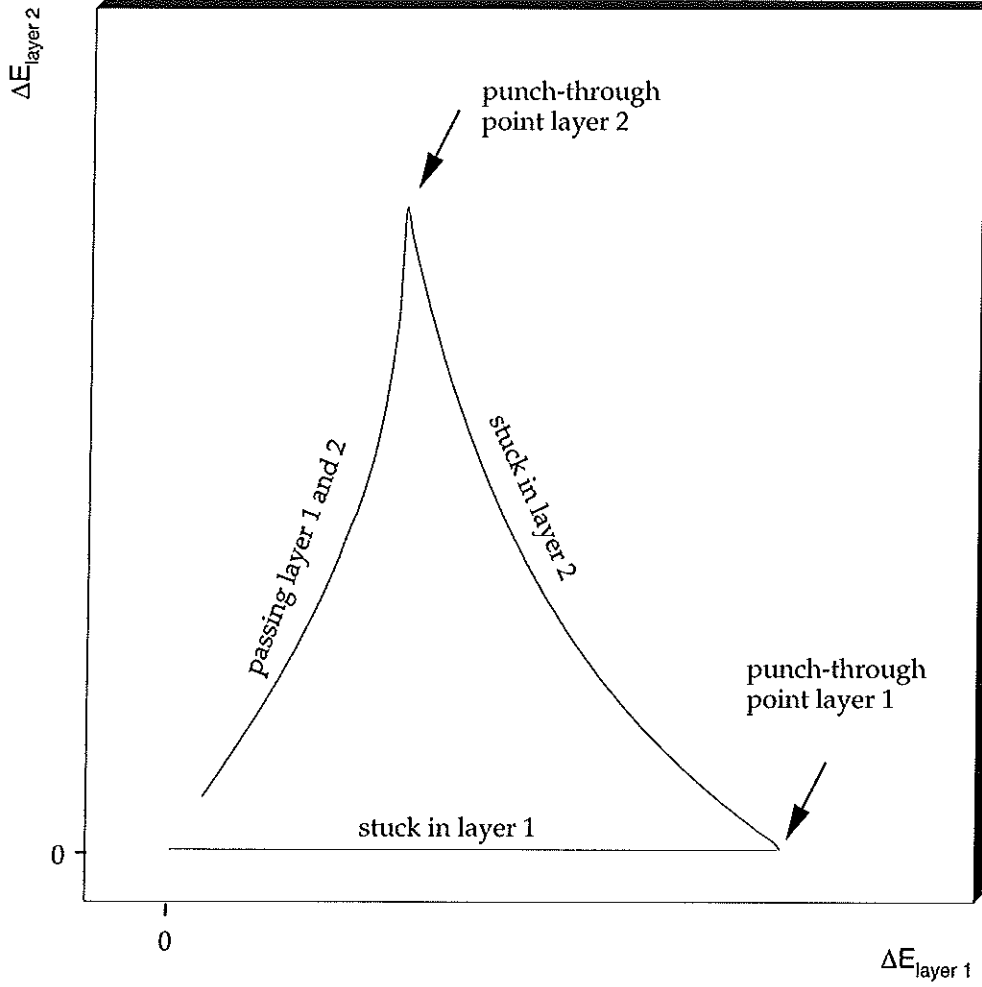
**Figure 2.3:** Schematic shape of the energy deposition $\Delta E_2(\Delta E_1)$ in a Silicon telescope.

(right curve). Again, the initial energy can be easily determined as the sum of $\Delta E_1(E)$ and $\Delta E_2(E)$. At even higher energies $E$, both layers are penetrated, and the total energy deposition decreases with $E$ (left curve). In this case, the initial energy can be calculated by inverting the dependence of the energy loss $S = dE/(\rho\,dx)$ on $E$ using numerical methods.

The effective value of the energy and mass resolution of a $\Delta E\!-\!E$ telescope is determined by several factors. As the energy deposition of a particle in a Silicon layer is obviously depending on the incidence angle $\alpha$, which is defined relative to the normal vector of the detector surface, an exact knowledge of $\alpha$ is of critical importance. Further contributions, which include energy straggling, thickness non–uniformities and electronic noise,

are discussed in detail in [B$^+$:97].

## 2.2 Monte Carlo Simulations

In order to reach a final design for a Silicon telescope to be installed in the HERMES target region, several detector parameters like the active area, the position, the number of layers, the layer thickness and the strip orientation and pitch have to be determined. Due to the large number of input parameters and physics processes to be considered in the detector response, an analytical approach to this problem is rather cumbersome. Therefore, extensive Monte Carlo simulations have been carried out to estimate the detector response for various combinations of the variables mentioned above. Furthermore, the influence of possible background sources has been investigated. Section 2.2.1 presents some general considerations concerning the detector geometry and position, while section 2.2.2 describes the setup and the processes considered in the simulation. The results in terms of detector yield and background conditions are summarized in section 2.2.3.

### 2.2.1 General Considerations

From the physics point of view, it would be desirable to have the HERMES Recoil Detector cover as much as possible of the area around the storage cell, i.e. to obtain a solid angle coverage of close to $4\pi$. Nevertheless, manpower and financing suggest to divide the project into two stages. In the so-called *Phase I*, a Silicon telescope will be installed below the storage cell, while in *Phase II*, additional detectors of similar design will cover the side and top region.

For the physics processes to be accessed by the HERMES Recoil Detector, it is sufficient to select a telescope with two Silicon layers. Hereby, the vertex determination is ensured by using a double–sided read–out on each layer, i.e. the strips on each side form an orthogonal grid and give direct information about the impact point. As the telescope will also be used to measure low–momentum spectator nucleons, the thickness of the first layer should be minimized to lower the punch–through energy and enable the determination of a second space point. While counters with a thickness of 60 $\mu$m are commercially available, a thinner detector also results in a lower signal–to–noise ratio in the output. The second layer should in principle be as thick as possible to maximize the fraction of stopped particles. However, restrictions in the realizable dynamic range of the read–out system make it necessary to limit the thickness to about 300 $\mu$m.

The dimensions and the position of the detector are constrained by the limited space in the HERMES target chamber and by the need not to obstruct the acceptance of the HERMES spectrometer. Nevertheless, it is possible to install a device with a total active area of (350×100) mm$^2$ centred along the $z$–axis at a distance of $\Delta y = 60$ mm from the first layer to the electron beam, as it is shown in figure 2.4. To ensure a sufficient angular resolution,
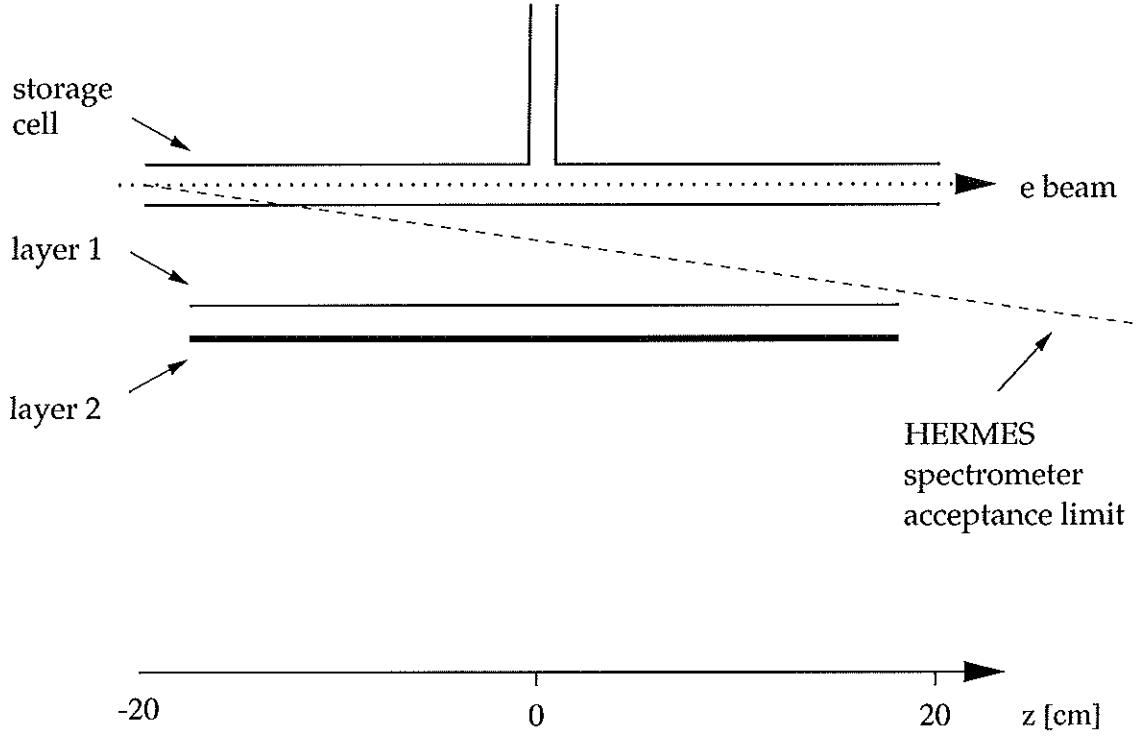
Figure 2.4: Schematic side view of the Phase I HERMES Recoil Detector.

the second layer is positioned at $\Delta y = 75$ mm, i.e. at a distance of 15 mm from the first layer.

The parameters described in this section are used as an input for the Monte Carlo simulations to gain insight into the detector yield and to investigate possible modifications.

## 2.2.2 Setup and Simulated Processes

The Monte Carlo simulations of the HERMES Recoil Detector are based on the GEANT library [B+:94], which is used to describe the geometrical setup and to perform the tracking of the generated particles[1]. The input geometry consists of the aluminum storage cell and the Silicon layers, which are positioned inside the vacuum of the target chamber. To allow for the running conditions of the longitudinally polarized HERMES target, the magnetic target holding field of 0.35 T parallel to the $z$–axis is taken into account[2]. The $z$–vertex

---

[1]While GEANT is mainly used in the field of high energy physics, the intrinsic energy deposition tables are of suitable accuracy in the low energy range to provide reliable results for the tracking of slow spectator particles.

[2]As the exact specifications of a transversally polarized HERMES target and the corresponding Recoil Detector design are not established, yet, the simulations are restricted to the longitudinal and the unpolarized

of an event is generated according to the target density distribution shown in figure 1.2, while the x– and y–vertex are fixed to zero.

The main physics process investigated in the simulations is the generation of a spectator proton in deep–inelastic scattering off a deuterium target. Due to the high energy deposition, a spectator event features a clear signature and is easily distinguishable from potential MIP background sources. On the other hand, current and target fragmentation in the deep–inelastic scattering process result in the generation of charged hadrons which potentially overlap in angle and momentum with protons from the spectator process. As both processes are of physics interest, it is essential to consider their interference in the Monte Carlo studies.

To achieve this, the LEPTO event generator [IER:97] is used to generate the complete final state of the $e(^2H, e')X$ process with the standard kinematical and acceptance cuts used in the HERMES experiment:

$$Q^2 > 1.0\,\mathrm{GeV}^2 \quad , \quad y < 0.85 \, ,$$
$$40\mathrm{mrad} < |\theta_y| < 140\mathrm{mrad} \quad , \quad |\theta_x| < 170\mathrm{mrad} \, .$$

In the case of an neutron scattering event, a spectator proton is added to the final state, and the generated particles are tracked through the geometrical setup.

As discussed in section 1.2.2, the spectator model allows a factorization of the deep–inelastic scattering and the spectator process. Therefore, the spectator proton is generated with an isotropic angular distribution and a momentum distribution $|\psi(|p_s|)|^2 \cdot p_s^2$ calculated from the deuteron $S$ and $D$ wave functions; for the latter, a parameterization based on existing data [Kra:76] is used. Figure 2.5 summarizes the distributions utilized for the simulation of a spectator particle in scattering off deuterium, with $\theta$ and $\phi$ being the polar and azimuthal angle of the generated particle.

If not stated otherwise, the simulations are based on a sample of $10^6$ generated events. For all particles, a common energy threshold of $E_{thr} = 100$ keV is applied.

Besides the generation of spectator protons, several other processes have been investigated using Monte Carlo techniques. These include polarized elastic scattering and possible background sources like Møller scattering and synchrotron radiation. While a summary of the results and the consequences for the HERMES Recoil Detector is presented in the following section, a detailed description can be found in [HERMES:97b].

### 2.2.3  Results

#### Spectator Yield

One of the fundamental parameters to be determined by the Monte Carlo simulations is the yield of spectator proton detection, i.e. the fraction of generated spectator protons
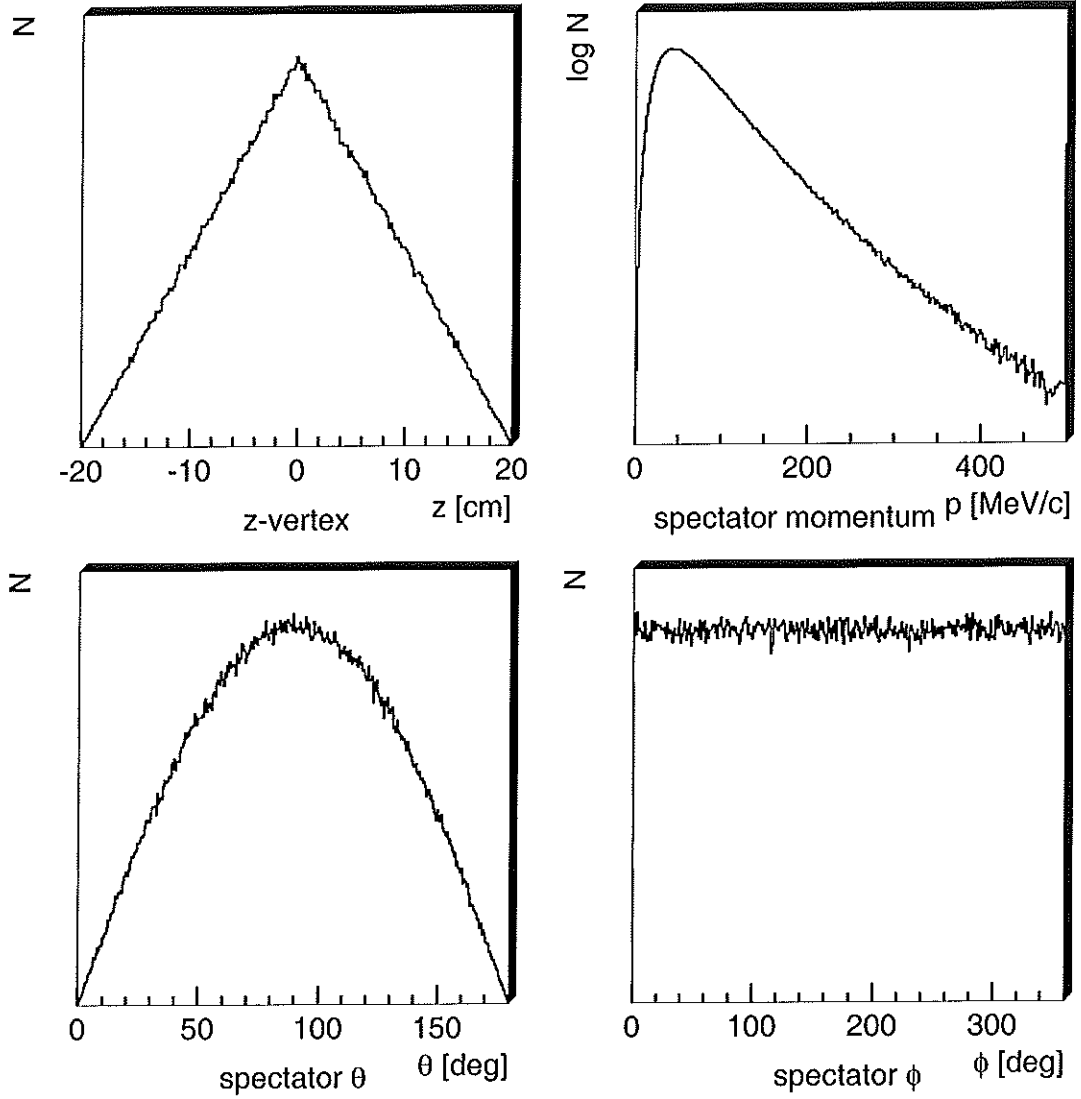
case.

Figure 2.5: Distributions utilized to generate the spectator proton kinematics in the Monte Carlo simulation.

which can be detected and reconstructed with the HERMES Recoil Detector. The main contributing factors to the yield are the storage cell wall thickness and the geometrical acceptance of the telescope. Due to the low momentum and therefore high energy deposition of the spectator particles, it is worthwhile to attempt the reconstruction of events which feature only one detector signal, i.e. in which the particle gets stuck in the first layer and the incident angle is determined by using the HERMES $z$-vertex. In the following, the

inclusion of this case will be identified as a *single hit*. For the additional requirement of the particle traversing the top layer and depositing energy in the second layer (*double hit*), the yield is further determined by the thickness of the first layer.

| Geometry | A | B | C | D |
|---|---|---|---|---|
| thickness first layer [$\mu$m] | 100 | 100 | 60 | 60 |
| thickness second layer [$\mu$m] | 300 | 300 | 300 | 300 |
| thickness storage cell wall [$\mu$m] | 75 | 50 | 75 | 50 |

**Table 2.1:** Geometrical setups used in the Monte Carlo simulations.

As the position and active area of the telescope are largely fixed by the spacial constraints in the target vessel (see section 2.2.1), the remaining free parameters are the thickness of the first layer and the storage cell wall. The simulations focus on four realizable geometrical setups for Phase I, which are described in table 2.1.

Firstly, the Recoil Detector response to pure spectator protons shall be addressed. Figure 2.6 shows the initial spectator momentum for all generated events in comparison to single hits and double hits in the Recoil Detector as simulated for geometry A. It can be seen that the absorption in the storage cell wall with a thickness of 75 $\mu$m introduces a momentum threshold of about[3] 75 MeV/c for particles reaching the first layer of the telescope. The further energy loss in the first layer results in an increased threshold for double hits of about 90 MeV/c.

By integrating the number of single hits over an initial momentum range which is clearly above the single hit threshold, and by normalizing the result to the number of generated events in this range, the geometrical acceptance of the Phase I Recoil Detector can be calculated to 19.5% of $4\pi$. This allows to define the *total yield* as the yield resulting from particle absorption and geometrical acceptance, while the *momentum yield* solely describes the accessible fraction of the momentum distribution. With the knowledge of the momentum yield, the acquirable number of events can easily be scaled with an increase in geometrical acceptance, e.g. for a Phase II Recoil Detector[4].

The yields determined for the different geometrical setups and normalized to the total number of generated spectator protons[5] are summarized in table 2.2. It can be concluded that the single hit yield shows a moderate increase with the use of a 50 $\mu$m storage cell, while the double hit yield profits more from a 60 $\mu$m first layer than from a thinner cell wall.

The $z$–vertex and the angular distribution for single hit spectator events with geometry

---

[3] As the threshold depends on the incidence angle of the particle, an exact value cannot be specified.

[4] While no detailed design for a Phase II Recoil Detector exists as yet, an increase by a factor of 3.4 in geometrical acceptance can be estimated.

[5] In scattering off $^2$H, this corresponds to approximately half the number of DIS events.
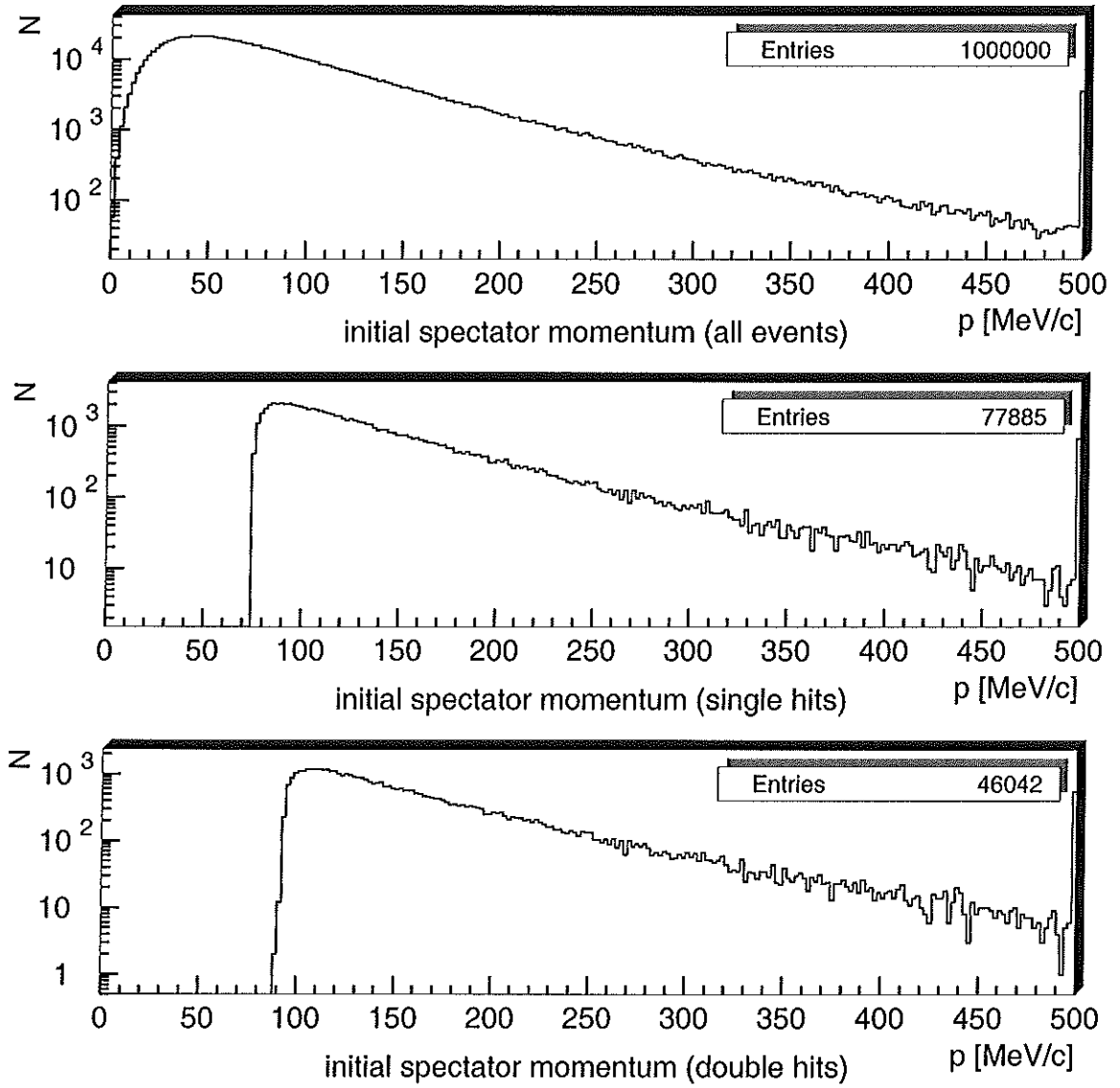
Figure 2.6: Initial momentum for detected pure spectator events (Geometry A).
Top: All generated events.
Middle: Single hits in the Recoil Detector.
Bottom: Double hits in the Recoil Detector.

A is shown in figure 2.7. The deviations from the input distributions (see figure 2.5) can be explained by the limits in $\theta$ and $\phi$ resulting from the detector geometry. If not stated otherwise, all following calculations are based on the geometry A of the HERMES Recoil

| Geometry | A | B | C | D |
|---|---|---|---|---|
| Single hit total yield [%] | 7.8 | 9.1 | 7.8 | 9.1 |
| Double hit total yield [%] | 4.6 | 5.0 | 5.3 | 5.8 |
| Single hit momentum yield [%] | 40.1 | 46.8 | 40.1 | 46.8 |
| Double hit momentum yield [%] | 23.6 | 25.7 | 27.2 | 29.8 |

Table 2.2: Spectator proton yield normalized to the number of generated spectator protons for the investigated geometry setups.

Detector.

Given the angular distribution shown in figure 2.7, the spectrum of the light cone momentum fraction $z_s$ for the detected spectator protons, which is shown in figure 2.8, can easily be derived. As expected, most events occur at $z_s \approx 1$, while the distribution drops steeply in the physically interesting regions of $|z_s - 1| > 0.2$. The kinematical condition corresponding to $\bar{z}_s = 1.2$ is satisfied by 9.3 % of the events, whereas $\bar{z}_s = 1.4$ is only met by 0.9 % of the sample. These values indicate that a significant measurement requires a high integrated luminosity.

## Fragmentation Products

As mentioned in section 2.2.2, the angular and momentum range of the fragmentation products from the deep–inelastic scattering process partly overlaps with that of the spectator protons. Due to the lack of experimental data in the low–energy domain, the available Monte Carlo generators may not deliver an exact prediction, but rather a coarse estimate of the conditions to be expected. As an aside, it is remarked that by sampling data e.g. in scattering off $^1$H, the HERMES Recoil Detector will deliver a new experimental insight into the angular and momentum distribution of low–energy fragmentation products.

In the simulation of the $e(^2\mathrm{H}, e')X$ process, the bulk of the fragmentation particles depositing energy in the first layer of the geometry A Recoil Detector consist of either charged pions (85 %) or protons (15 %). To determine in how far these may dilute the detection of low–momentum spectator protons, a modest energy deposition threshold of $\Delta E_{thr\,t} = 150$ keV is introduced to remove minimum ionization particles[6], resulting in in a ratio of about 50 % charged pions and 50 % protons. Accounting for the different detector thickness, a threshold of $\Delta E_{thr\,b} = 450$ keV is applied to the bottom layer when considering double hits. The proportion of protons is in this case increased to about 70 %.

The momentum distribution of the fragmentation particles detected in the Recoil Detector is displayed in figure 2.9 for the case of single and double hits. As the spectra of

---

[6]The minimum ionization energy deposition in 100 $\mu$m of Silicon is $\Delta E_{MIP} \approx 40$ keV and scales with $1/\cos\alpha$ of the incidence angle.
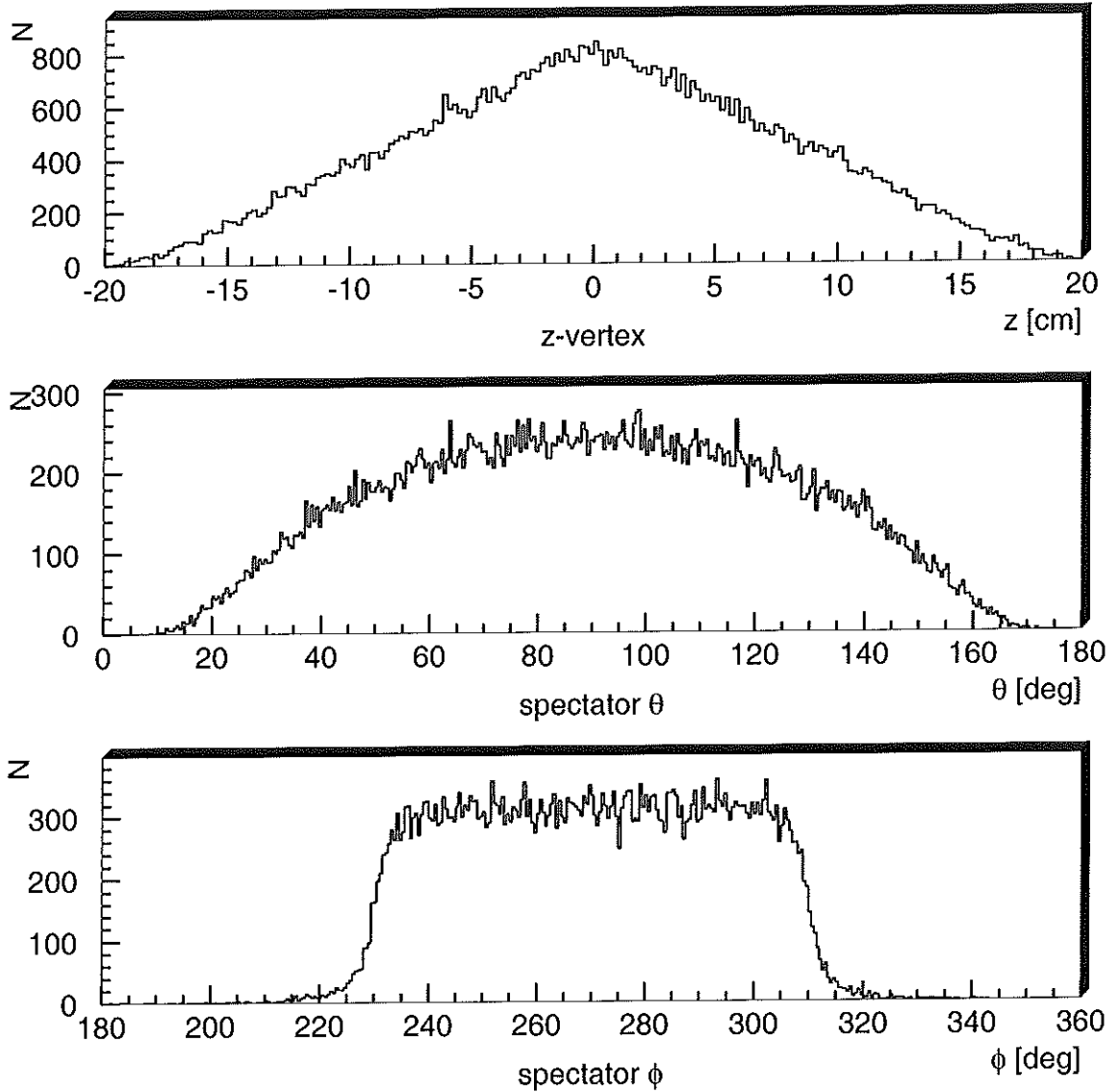
Figure 2.7: $z$–vertex and angular distributions for single hit spectator events (Geometry A).

pions and protons are superimposed, a minimum is observed at $\approx 200$ MeV/c. With the above–mentioned MIP cuts, a single hit event is observed for about 3.4 % of the DIS events, while double hits occur in only 1.1 % of the cases.

The mean multiplicity of the fragmentation products in the full active area is 1.35 for single hits and 1.29 for double hits. Given the fact that each telescope layer will be composed of several small modules (see section 2.4), the particle track reconstruction is there-
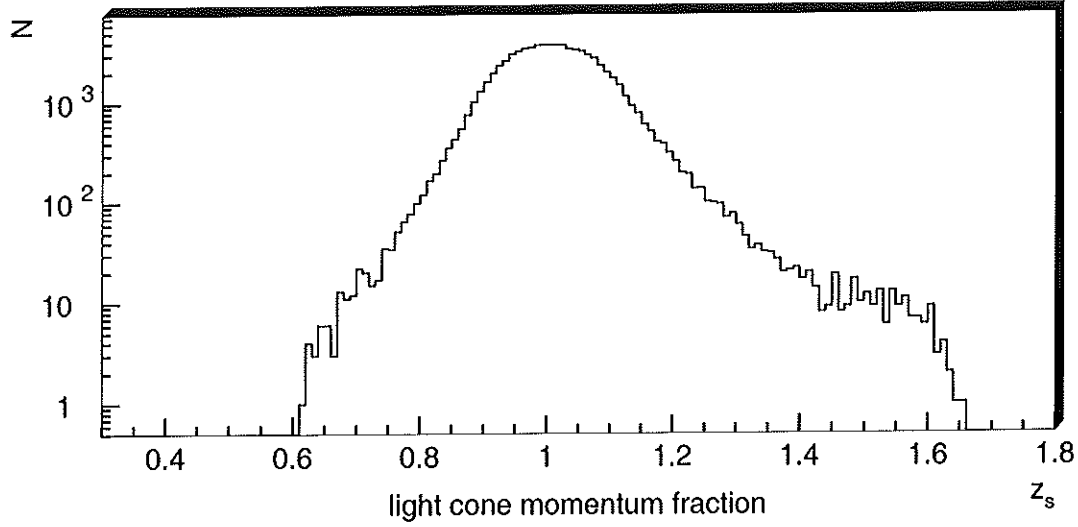
Figure 2.8: Light cone momentum fraction $z_s$ for single hits in the geometry A Recoil Detector. A MIP cut is applied.

fore ensured. The dilution of a single hit spectator proton event, i.e. the case in which a fragmentation particle deposits a higher energy in the telescope than the synchronous spectator proton, occurs in only 0.4 % of the DIS events and is therefore negligible. On the other hand, when considering the total number of $e(^2H, e'p)X$ events which pass the MIP cuts, 46.8 % of the single hits and 32.2 % of the double hits originate from fragmentation products and not from a spectator proton. While a doubling of the thresholds, which has only a minor effect on the number of detected spectator protons, reduces these fractions to 21.3 % and 12.2 %, it will be shown that several other methods exist to ensure a clean spectator proton signature.

Unlike the isotropic distribution of the spectator protons, the angular spectrum of the fragmentation products shows a clear boost to the forward direction, which is also noticeable in the $z$–vertex distribution of the detected particles. As illustrated in figure 2.10, almost all events recorded by the Recoil Detector originate from the $z < 0$ cm region, with polar angles of $\theta < 90°$. In the kinematic range in which energy deposition and PID cuts (see next section) are insufficient to distinguish spectator and fragmentation events, it is therefore possible to apply a further cut on the scattering angle.

### Energy Deposition and Angular Resolution

The path length of a particle traversing a Silicon layer depends on the inverted cosine of the incident angle $\alpha$, which is defined as the angle relative to the normal vector of the
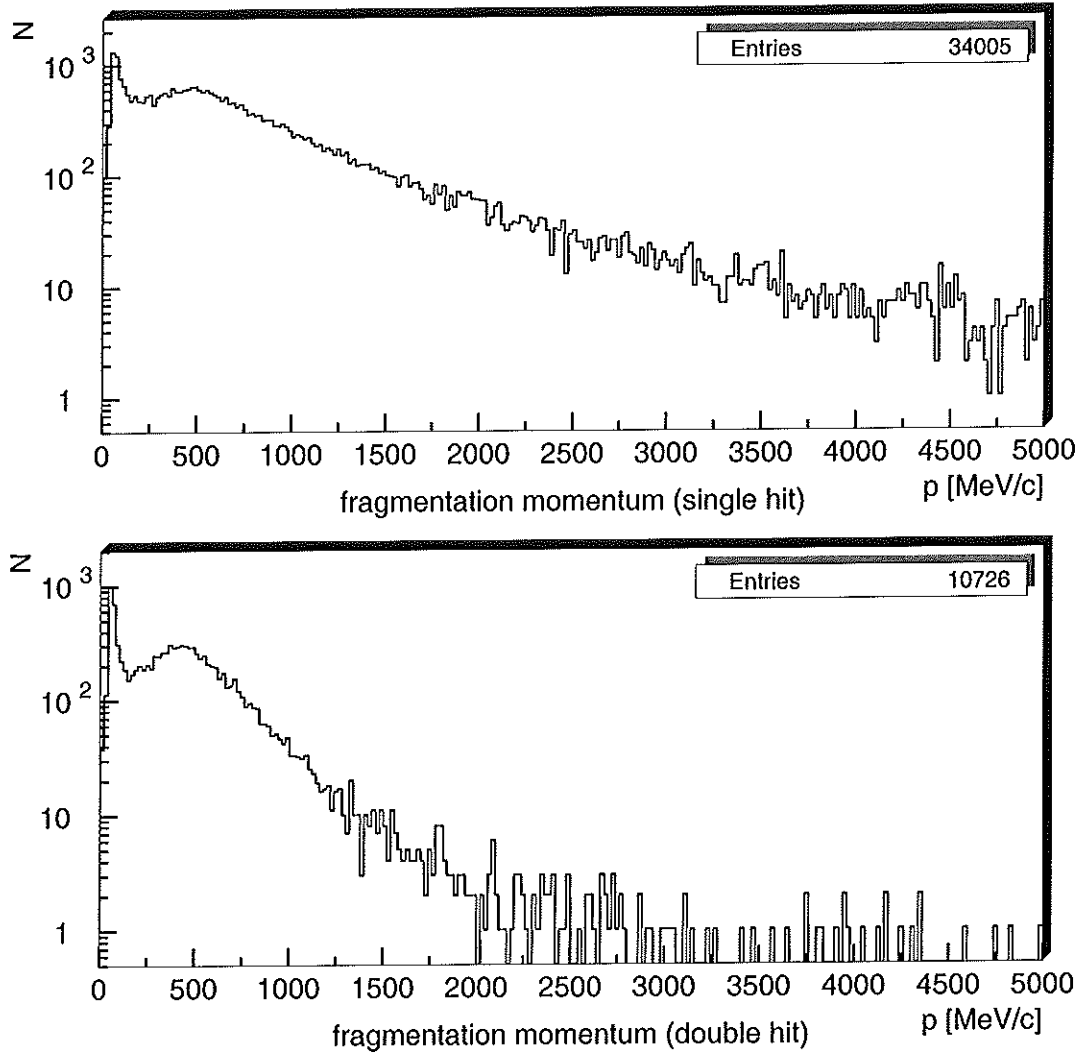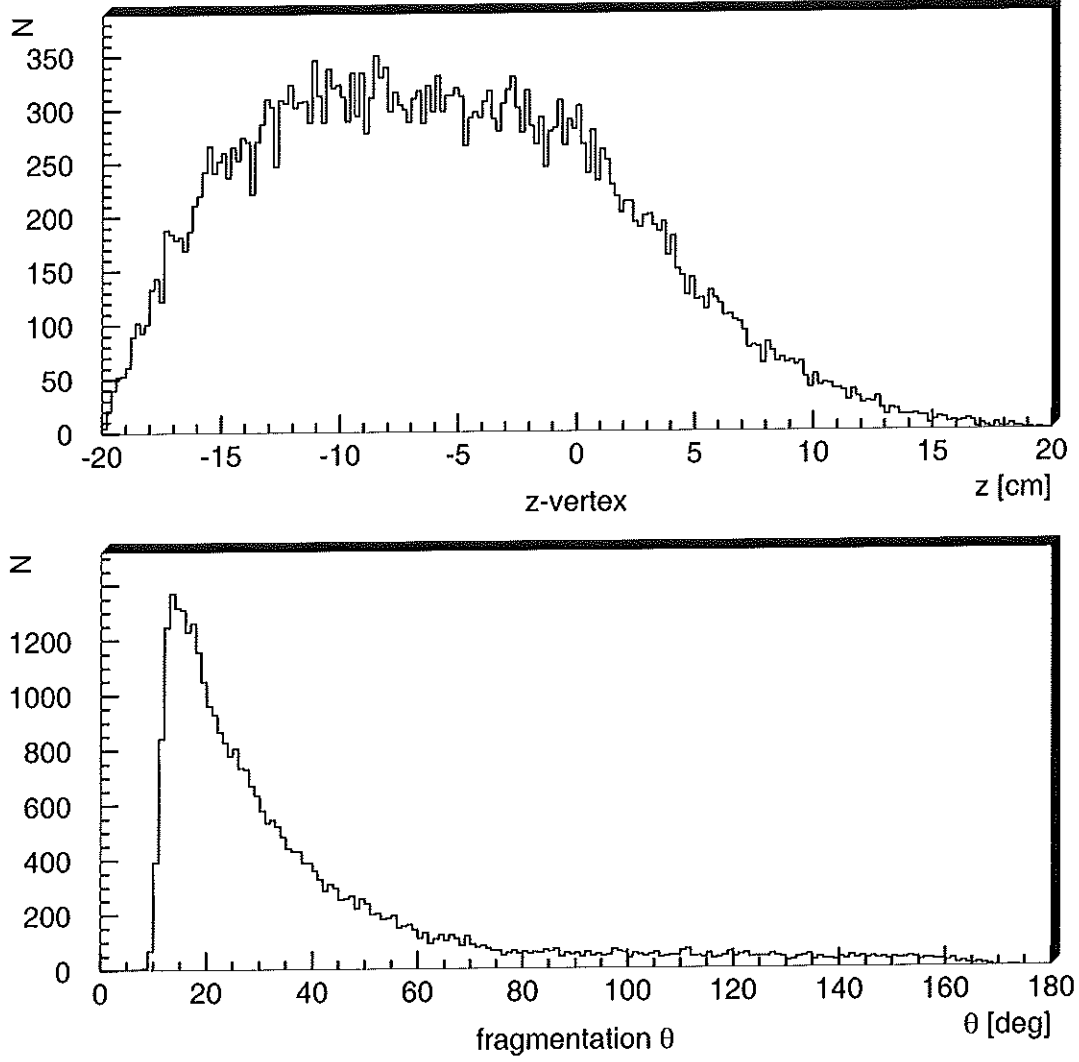
**Figure 2.9:** Momentum distribution for detected fragmentation events (Geometry A). An energy deposition threshold of $\Delta E_{thr\ t} = 150$ keV for the first layer and $\Delta E_{thr\ b} = 450$ keV for the second layer is applied.

detector surface and relates to the common scattering angles $\theta$ and $\phi$ as

$$\cos\alpha = -\sin\theta \cdot \sin\phi\ .$$

To reach a straightforward dependency between the measured impact coordinates and the incident angle, it proves convenient (see section 4.3.3) to use the projected polar angle

**Figure 2.10:** $z$–vertex and angular distribution for detected single hit fragmentation events (Geometry A). An energy deposition threshold of $\Delta E_{thr\,t} = 150$ keV for the first layer is applied.

$\theta_{(yz)} := \arctan(\Delta y/\Delta z)$, resulting in the relation

$$\tan \alpha = \sqrt{\tan^{-2}\theta_{(yz)} + \tan^{-2}\phi}\,.$$ 
(2.1)

As it has been pointed out in section 2.1, a reliable initial energy determination and particle identification highly depends on an exact knowledge of the incident angle $\alpha$.

This can be illustrated by means of figure 2.11, which shows the correlation between
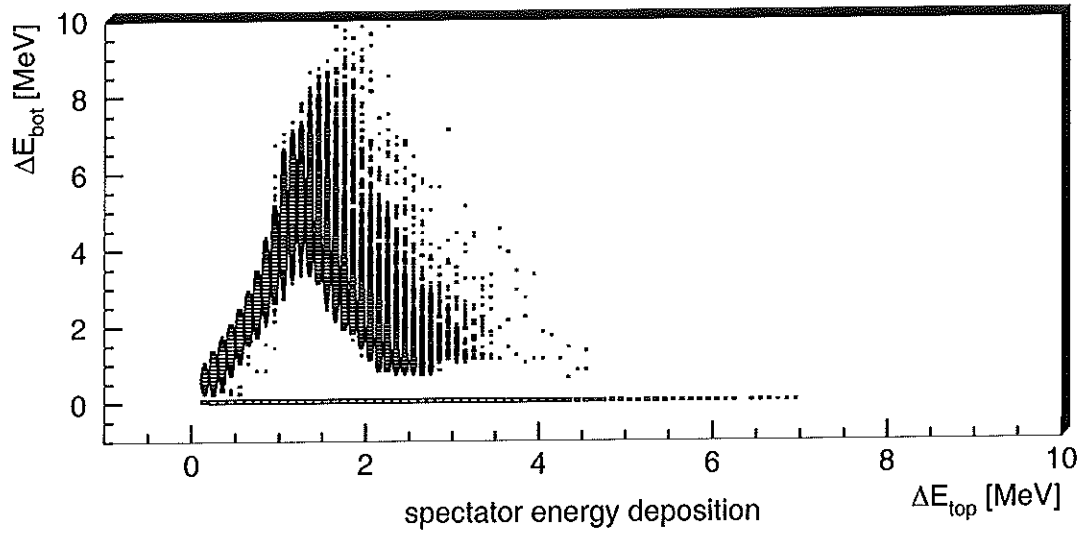
**Figure 2.11:** Correlation of the energy depositions in the top and the bottom layer of the geometry A Recoil Detector for pure spectator proton events. The $z$-axis features a logarithmic scale.
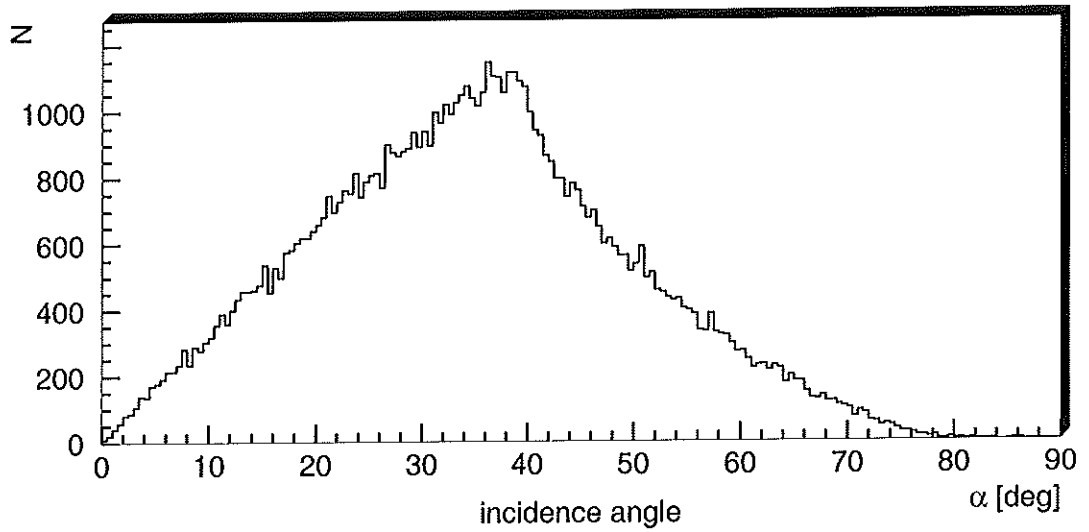


**Figure 2.12:** Incident angle $\alpha$ in the geometry A Recoil Detector for pure spectator proton events with a single hit cut.

the energy depositions in the top and the bottom layer of the geometry A Recoil Detector for pure spectator proton events. While the basic triangular shape can be recognized, the deposition values are smeared due to the wide range of incident angles, as seen from the
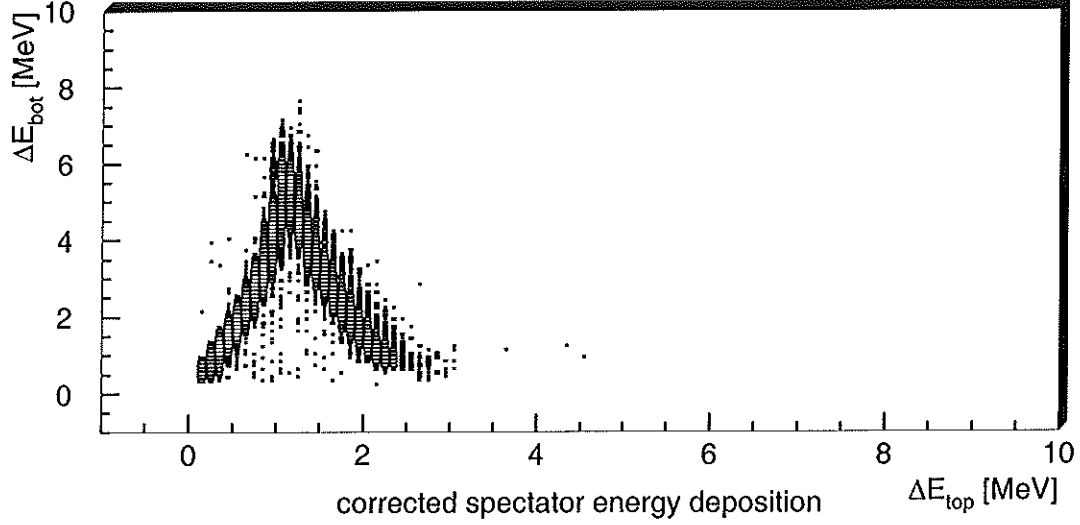
**Figure 2.13:** Correlation of the energy depositions corrected with the factor cos(0.79 · $\alpha$) in the top and the bottom layer of the geometry A Recoil Detector for pure spectator proton events. The $z$-axis features a logarithmic scale, and a double hit cut is applied.

distribution in figure 2.12. To distinguish between the deposition triangles of different particle types, it is essential to correct the energy deposition to a value which is independent of $\alpha$.

However, the energy loss of slow protons does not scale with the path length and an analytical energy reconstruction can only be applied with the knowledge of the particle type. Nevertheless, the desired unsmearing can be achieved by multiplying the energy deposition with an empiric factor [Ste:98a] of cos(0.79 · $\alpha$), which results in the corrected correlation plot shown in figure 2.13. This technique therefore allows a separation of particle types and a direct comparison of the energy deposition with theoretical predictions irrespective of the underlying angular spectrum.

As none of the forseen physics applications of the HERMES Recoil Detector impose any severe restrictions on the angular resolution, the required accuracy and the resulting strip pitch is determined by the particle identification needs. Due to the geometrically limited range in the azimuthal angle $\phi$ (see figure 2.7), the angular resolution is predominantly given by the vertical distance $d$ between the layers and the polar angle resolution d$\theta$, which is related to the $z$-resolution d$z$ by

$$dz = d \left(1 + \tan^{-2}\theta\right) \cdot d\theta \ .$$

To be able to distinguish protons and deuterons in the telescope, the factor cos(0.79 · $\alpha$) has to be known to better than 2 %. This results in a required strip pitch of 0.25 mm for the $z$-direction, while for the $x$-direction 1.00 mm is sufficient.
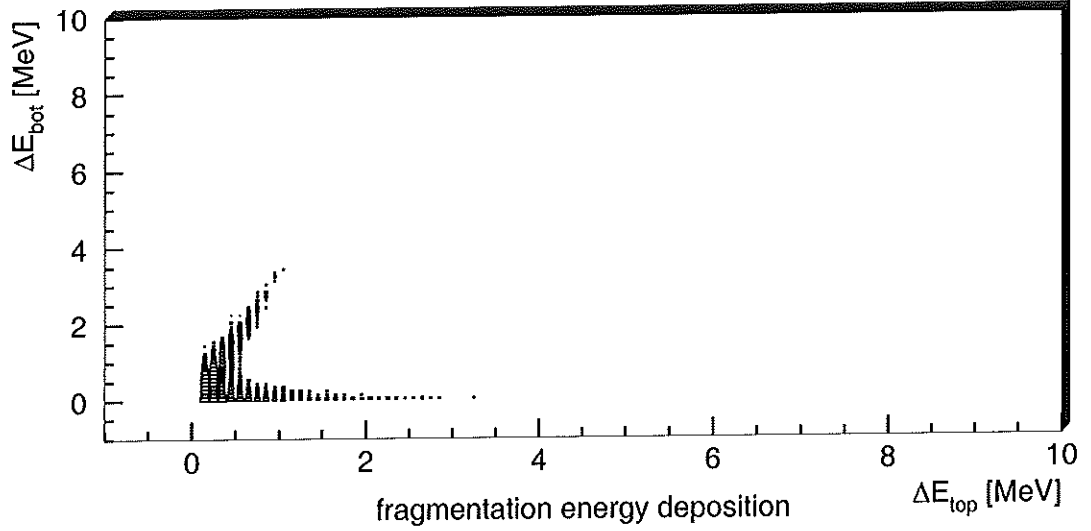
**Figure 2.14:** Correlation of the energy depositions in the top and the bottom layer of the geometry A Recoil Detector for fragmentation particles. The $z$-axis features a logarithmic scale.

The energy deposition distributions derived from the simulations can further be used to investigate possible ways of separating fragmentation products and spectator protons. As shown in figure 2.14, due to the higher initial momenta the energy loss induced by fragmentation particles is considerably lower in comparison to that resulting from spectator protons.

In order to determine in how far energy deposition cuts can effect a clear signature of spectator events, two cases have to be considered. For a double hit complying with the MIP cuts, the energy depositions in each layer resulting from spectator protons and fragmentation products are shown in figure 2.15. It can be seen that the overlap of the two contributions is rather small and that an increase in the energy deposition threshold leads to a satisfactory separation without markedly affecting the detection yield of the spectator process.

In the case of pure single hits, i.e. of particles stopped in the first layer, the energy deposition is depicted in figure 2.16. Here, the separation is even easier to achieve, as the considered spectator particles correspond to the lower part of the momentum spectrum. The energy deposition basically only starts[7] at a value of $\Delta E \approx 800$ keV, while the bulk of the fragmentation energy deposition is clearly below this threshold. It is therefore reasonable to assume that also pure single hits can be included in the Recoil Detector analysis.

For the analysis of the HERMES Recoil Detector data, naturally a combination of the

---

[7]The energy deposition values of less than $\Delta E \approx 800$ keV correspond to particles traversing the first but not hitting the second layer for acceptance reasons. This effect can easily be averted by a $\phi$ cut.
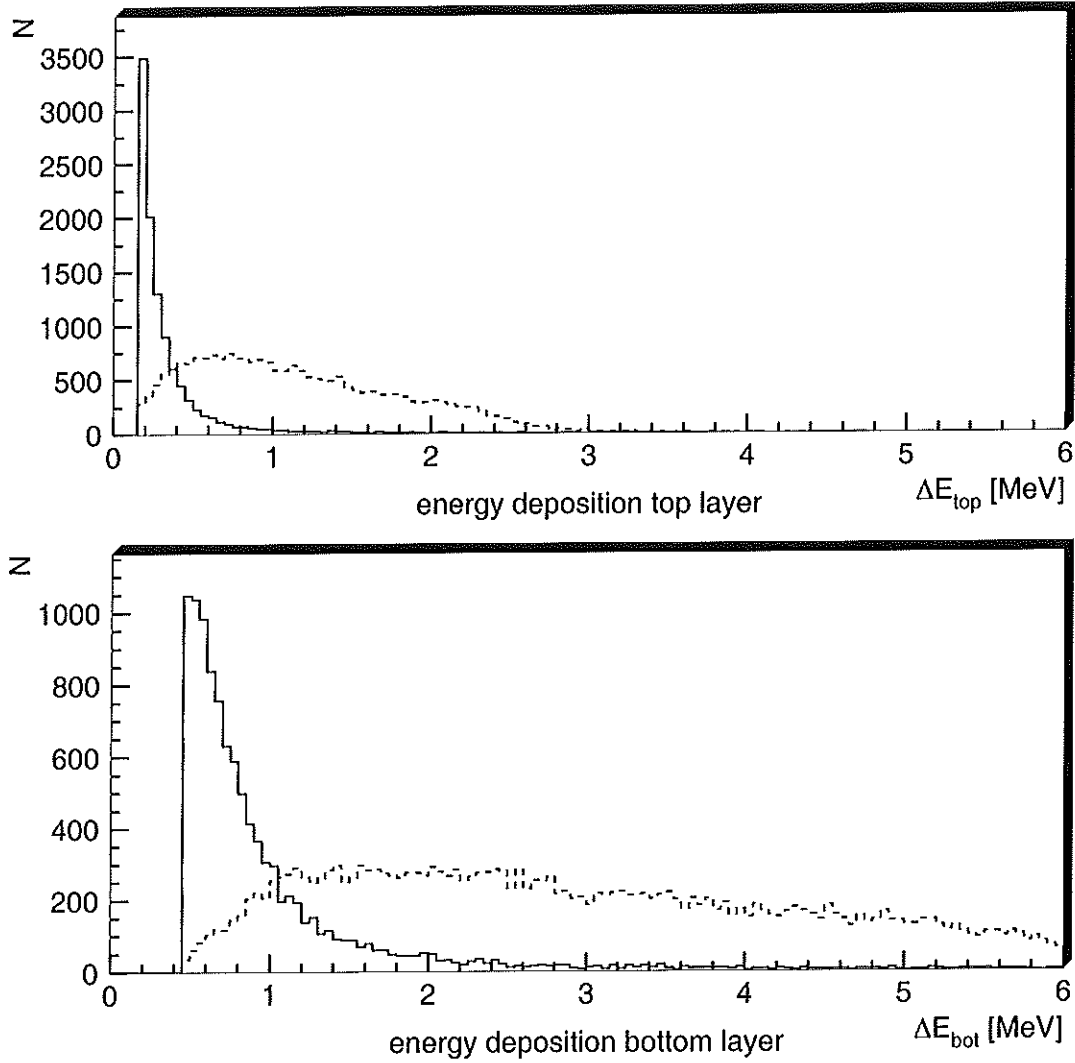
Figure 2.15: Energy depositions in top and bottom layer for double hits resulting from fragmentation products (solid curve) and spectator protons (dashed curve). A MIP cut is applied.

above-mentioned energy deposition, angular and PID cuts will be applied. The simulation of fragmentation products in the relevant energy range may only give an indication of the expected conditions, and the determination of exact values for different combinations of cuts is therefore inappropriate. As measurements with the Recoil Detector will be carried out both with $^1$H and heavier targets, a comparison of the resulting momentum and angular distributions will give direct experimental evidence of both the spectator and the fragmentation process.
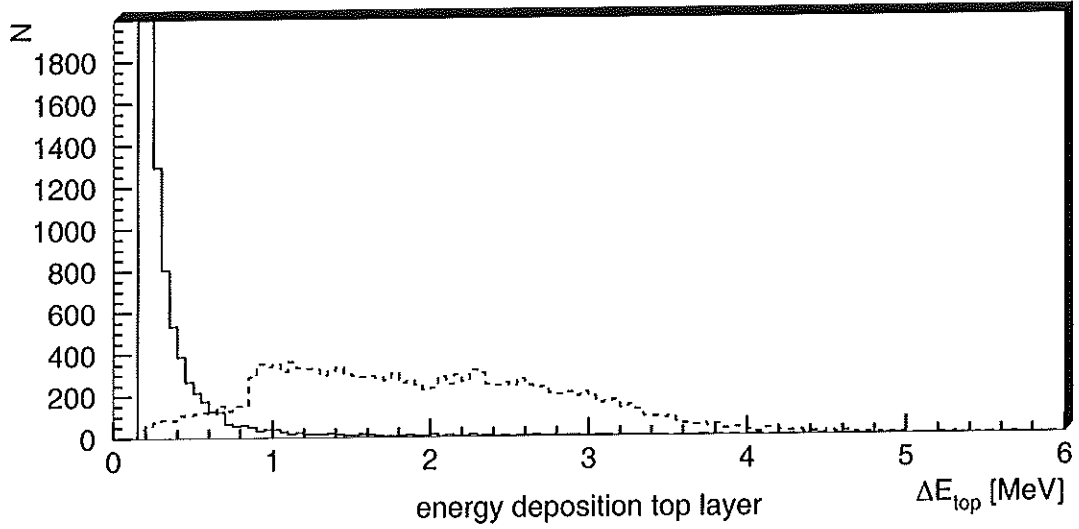
Figure 2.16: Energy depositions in top layer for single hits resulting from fragmentation products (solid curve) and spectator protons (dashed curve). A MIP cut is applied.

## Background

Given the close proximity of the Recoil Detector to the HERA electron beam, the influence of potential background sources on the operation of the detector has been studied [HERMES:97b]. Hereby, Møller scattering off the atomic electrons in the target gas is expected to be the dominant contribution. The results presented in the following are based on a beam current of 40 mA and a target density of $1 \cdot 10^{15}$ cm$^{-2}$.

The total rate of Møller electrons in the acceptance of the geometry A Recoil Detector amounts to $\approx$ 23 MHz and reduces to $\approx$ 9 MHz after the application of a 20 keV threshold. When considering the maximum rate per detector strip, a strong dependence on the employed threshold is observed. While a 20 keV threshold corresponds to a value of $\approx$ 5 kHz per strip, this rate drops to less than 100 Hz once a 100 keV threshold is applied. From this, an average occupancy of $\approx$ 0.1 % for each Silicon plane can be estimated, which is not critical for the Recoil Detector operation. It is noted that the presence of a longitudinal holding field in the target deviates the slow Møeller electrons, thereby reducing the incident rate by more than a factor of 100.

As the Recoil Detector is protected from direct synchrotron radiation by two movable collimators upstream of the HERMES storage cell, only double scattered photons can reach the detector acceptance. The resulting total rate is estimated to $\approx$ 1 MHz and will for the most part be removed by a 100 keV threshold in the first Silicon layer. It is therefore concluded that the expected background causes no operational problems for the HERMES Recoil Detector.

## 2.3   Expected Statistical Uncertainties

As mentioned in section 1.1.2, the typical target density used in the HERMES experiment is about an order of magnitude higher for the case of unpolarized operation as compared to polarized running. While the spectator tagging measurements can of course also be carried out with a polarized target, it is sensible to use the unpolarized target density as a basis for predictions of the achievable statistical uncertainty. To account for factors like detector efficiencies and acceptance effects at HERMES , the calculations are based on previous HERMES data [Vin:96] and scaled to the desired integrated luminosity. In a conservative approach, the single hit spectator yield of 7.8 % for the current target setup with a storage cell wall thickness of 75 $\mu$m is used as an input.

| $x$–bin | $\delta F_2^n$ [%] (400 pb$^{-1}$) |
|---------|------------------------------------|
| 0.125   | 0.37                               |
| 0.175   | 0.45                               |
| 0.235   | 0.47                               |
| 0.310   | 0.59                               |
| 0.400   | 0.81                               |
| 0.525   | 1.29                               |
| 0.645   | 3.74                               |

Table 2.3: Estimated statistical errors on $F_2^n$ for an unpolarized $^2$H target assuming a tagging efficiency of 7.8 %.

Table 2.3 shows the estimated statistical errors on the measurement of the tagged neutron structure function $F_2^n$ for different $x$–bins. The values have been scaled to an integrated luminosity of 400 pb$^{-1}$, which corresponds to approximately four weeks of continuous data taking under the assumption of a $^2$H target density of $1 \cdot 10^{15}$ cm$^{-2}$ and an average beam current of 20 mA[8]. A similar estimate is presented in table 2.4, which gives the predicted statistical errors in $F_2^n$ for the kinematical condition of $\bar{z}_s = 1.2$, as needed for the separation of the different theoretical models of the EMC effect in $^2$H.

For both cases, it can be observed that the statistical uncertainties in the high-$x$ region for an integrated luminosity of 400 pb$^{-1}$ are barely sufficient to significantly distinguish between the different theoretical predictions discussed in section 1.2.2. This problem could either be overcome by a dedicated data taking time with a high–density unpolarized target, by an increase in the tagging efficiency resulting from a thinner storage cell wall or, naturally, by the installation of a Phase II Recoil Detector. As an aside, it is mentioned that the fraction of detected high-$z_s$ events could be increased by putting the detectors active

---

[8] A comparable integrated luminosity has been reached in the 2000 running period by increasing the target density towards the end of a HERA electron fill.

| $x$–bin | $\delta F_2^n$ [%] (400 pb$^{-1}$) |
|---------|------------------------------------|
| 0.310   | 1.93  |
| 0.400   | 2.67  |
| 0.525   | 4.24  |
| 0.645   | 12.27 |

**Table 2.4:** Estimated statistical errors on $F_2^n$ under the kinematical condition of $\bar{z}_s = 1.2$ for an unpolarized $^2$H target, assuming a tagging efficiency of 7.8 %.

area closer to the storage cell in the $z < 0$ cm region.

## 2.4  Conceptual Design of the HERMES Recoil Detector

The following sections present an overview of the design specifications for a Phase I HERMES Recoil Detector. A full write-up on this subject can be found in [HERMES:97b], while a summary has been published in [vB$^+$:98].

### 2.4.1  Geometry

The overall dimensions of the active area of the Phase I HERMES Recoil Detector have been discussed in detail in section 2.2; the relevant parameters are summarized in table 2.5. Each layer consists of 14 individual detector modules with an active area of $(50 \times 50)$ mm$^2$

| | |
|---|---|
| Total length | 350 mm |
| Total width | 100 mm |
| Position in $x$–$z$ plane | centred rel. to $(0, 0)$ |
| Position in $y$ (top layer) | -60 mm |
| Position in $y$ (bottom layer) | -75 mm |
| Thickness (top layer) | 100 $\mu$m |
| Thickness (bottom layer) | 300 $\mu$m |
| Strip pitch in $z$ | 250 $\mu$m |
| Strip pitch in $x$ | 1 mm |

**Table 2.5:** Geometry parameters of the Phase I HERMES Recoil Detector in the HERMES coordinate system.

each. Figure 2.17 shows the Silicon telescope mounted underneath the HERMES storage cell. The perspective faces the target vacuum chamber flange, i.e. the view is against the beam direction.
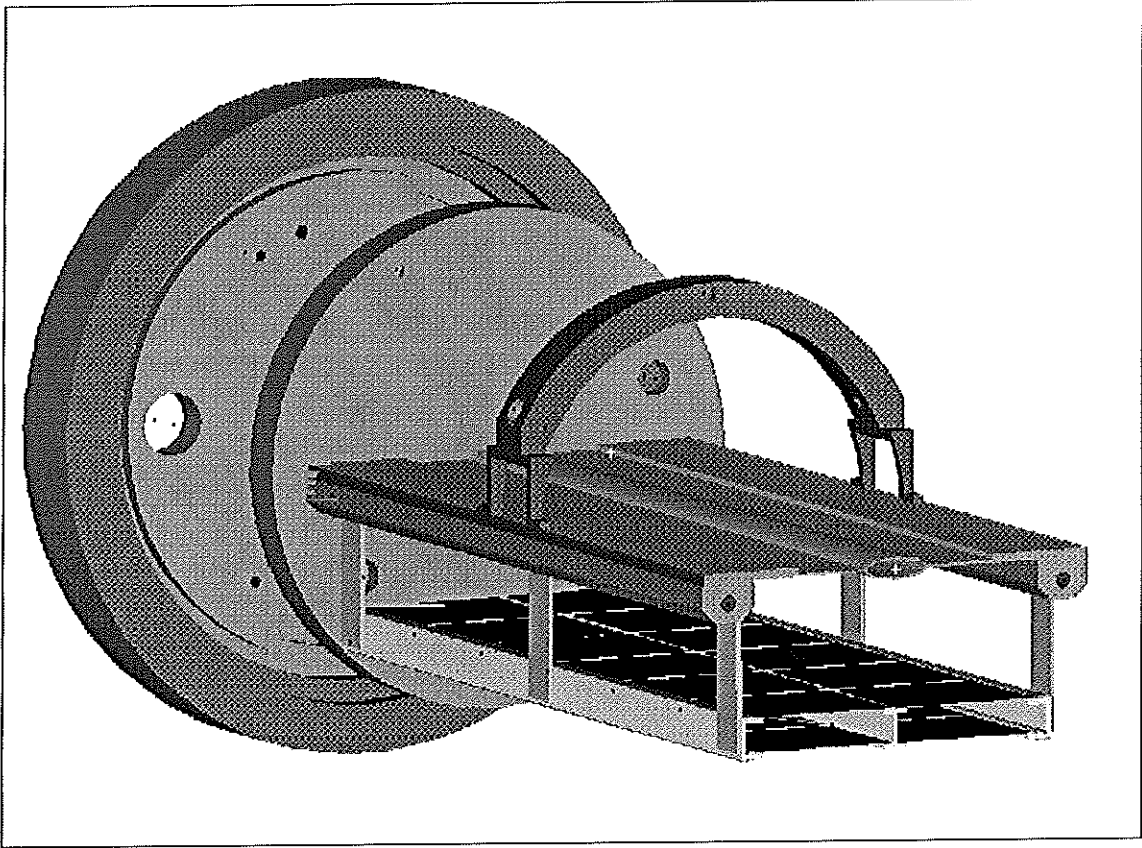
Figure 2.17: Conceptual design of the HERMES Recoil Detector. The two layers of Silicon are shown underneath the HERMES storage cell.

## 2.4.2 Readout

The subdivision of the Recoil Detector into 28 modules and the strip pitch of 250 $\mu$m in the $z-$ and 1 mm in the $x-$direction result in a total of 7000 analogue signals that have to be read out and digitized. In order to reduce noise contributions and to minimize the amount of signal wires to be routed out of the target chamber, it is essential to mount part of the readout electronics close to the strips themselves. Therefore, the readout system will consist of a basic front–end chip and output driver inside the target chamber, while control and signal digitization take place outside of the vacuum environment.

As the Recoil Detector will be used for the detection of both minimum ionizing and slow spectator particles, a wide range of energy depositions is encountered. Thus, the dynamic range required of the readout system must be considerably higher than a factor of 100 to be able to process all kinds of possible signal heights. As readout of an event is

initiated by an external HERMES trigger, the system further has to be capable of handling the typical HERMES trigger rates of $\approx 250$ Hz.

A detailed design of a readout system satisfying these requirements is described in [HERMES:97b]. However, some alterations may be necessary, as the concept is based on the use of the APC–64 front–end chip, of which recent tests (see section 4.1) indicate that it does not provide the necessary radiation hardness.

## 2.4.3 Mechanics

As the HERMES Recoil Detector and part of the readout electronics will be positioned inside the vacuum of the target chamber and in close proximity to the HERA electron beam, the mechanical design has to account for outgassing, beam–induced RF fields, radiation and cooling. In the following, a summary of design options considering these constraints is presented.

The high vacuum environment in the HERMES target area is usually at a level of $10^{-7}$ mbar for polarized gases and $10^{-6}$ mbar for the unpolarized case. As outgassing of the various components of the HERMES Recoil Detector must not degrade these levels, two possible options can be considered: the construction of a separate vacuum housing for the detector, or a direct placement inside the vacuum environment. While the former option would also ensure an effective RF shielding, it has the major drawback of increasing the momentum threshold for the detection of spectator particles. By using low–outgassing materials like ceramic carrier boards and Kapton–coated signal wires, an unshielded mounting can be realized, while a thin wire mesh provides protection against RF effects.

Concerning radiation damage, the integrated total dose for the 1996 running period at a comparable position has been measured to $\approx 5$ krad, while the neutron flux is estimated to the order of $7 \cdot 10^{10}$ cm$^{-2}$. Both values are well below the critical levels for Silicon counters, and no major degradation is expected.

The readout electronics inside the vacuum will produce a considerable amount of heat, which, depending on the employed readout chip, is in the order of 50 W. As it is also advantageous to operate the Silicon counters at low temperatures for reasons of radiation damage, the installation of a cooling system is essential. Again, a detailed design based on the use of Peltier elements is presented in [HERMES:97b]. The principal feasibility of operating a Silicon telescope under the above–mentioned boundary conditions has been proven by the installation of a small test device, which is described in the following chapters.

# 3 The HERMES Silicon Test Counter

As outlined in the previous chapter, the successful operation of a Silicon telescope in the HERMES target region is, while rewarding from the physics point of view, a challenging task. The feasibility of meeting the design stipulations imposed by the vacuum environment and the proximity to the HERA electron beam has to be demonstrated and the proposed measurements require a proof of principle. Therefore, a *Silicon Test Counter* (STC) featuring the full functionality of the HERMES Recoil Detector was installed in early 1998 and has been operated during several months of HERMES data taking. The concept and design of this detector is presented in section 3.1, while section 3.2 summarizes the results of a series of tests carried out using the tandem accelerator at the University of Erlangen. The expected performance of the STC in the HERMES environment, as estimated by means of Monte Carlo simulations, is discussed in section 3.3.

## 3.1 Concept and Design

### 3.1.1 Geometry

The aim of installing the Silicon Test Counter is to prove the feasibility of operating a HERMES Recoil Detector as described in chapter 2. Therefore, a comparable range of incident momenta and angles have to be covered by the STC acceptance, and the telescope parameters have to ensure a similar detector response.

Due to the HERMES target density distribution, the STC will be centred to the $x$– and $z$–axis. In accordance with the Recoil Detector design, the active area of the STC is positioned underneath the HERMES storage cell and arranged in two levels at $y = -60$ mm and $y = -75$ mm, which allows particle identification as well as momentum and vertex reconstruction. While for the upper layer only one Silicon module is used, the lower layer consists of two adjacent wafers with different thicknesses, which are aligned along the $z$ axis symmetrical to $z = 0$ mm. This allows to study the correlation of the energy depositions for two different module combinations and, by arranging the thicker layer at higher $z$, results in a higher energy deposition for the minimum ionizing particles occurring at smaller scattering angles $\theta$.

Partly determined by commercial availability, the three Silicon wafers used for the STC each have an octagonal shape with a kerb distance of 64 mm. Two equal modules with a
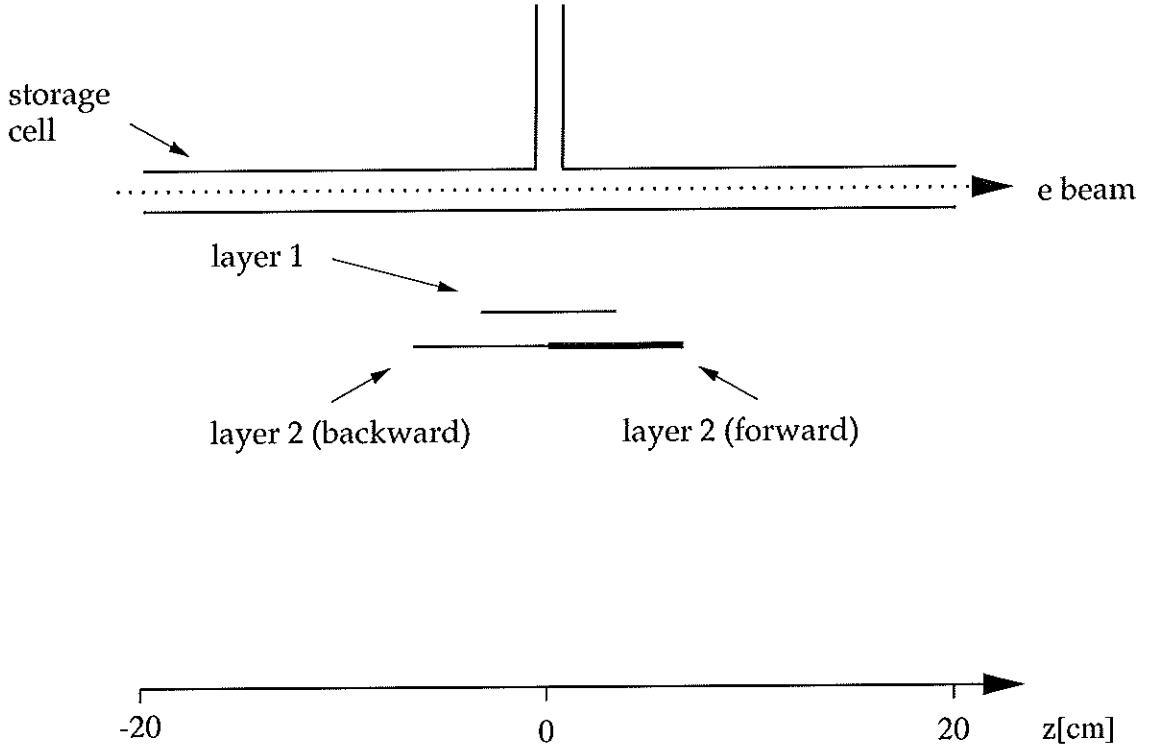
---

Figure 3.1: Schematic side view of the Silicon Test Counter.

thickness of 135 $\mu$m are used as the top layer and the backward–facing half of the bottom layer, while the forward–facing bottom layer has a thickness of 306 $\mu$m. All modules feature double–sided readout with orthogonal strips and a strip pitch of 1 mm. Hereby, the ohmic side determines the $x-$ and the junction side the $z$–coordinate of a traversing particle. Table 3.1 summarizes the geometry parameters of the Silicon Test Counter, while figure 3.1 shows a side view of the active area relative to the HERMES storage cell.

## 3.1.2   Readout

Given by the dimensions and strip pitch of the Silicon Test Counter, a total of 384 analogue signals have to be processed and incorporated into the HERMES data acquisition. To ensure a short construction phase, the readout system is based on the use of the APC–64 front–end chip [HP:93], which is already utilized in the HERMES vertex chambers. While these chips are mounted close to the Silicon layers inside the vacuum environment, it is possible to place the control logic and the digitizing electronics outside of the HERMES target vessel. One STC module features 128 strips, whereby one APC corresponding to each the ohmic and the junction side is needed for the readout of a Silicon layer. Therefore, a

| Total width | 64 mm |
| --- | --- |
| Total length (top layer) | 64 mm |
| Total length (bottom layer) | 128 mm |
| Position in $x$–$z$ plane | centred rel. to $(0,0)$ |
| Position in $y$ (top layer) | -60 mm |
| Position in $y$ (bottom layer) | -75 mm |
| Thickness (top layer) | 135 $\mu$m |
| Thickness (bottom layer backward) | 135 $\mu$m |
| Thickness (bottom layer forward) | 306 $\mu$m |
| Strip pitch in $z$ | 1 mm |
| Strip pitch in $x$ | 1 mm |

Table 3.1: Geometry parameters of the Silicon Test Counter in the HERMES coordinate system.

total of six AP chips are utilized in the STC.

The APC stores 64 analogue signals in a circular pipeline, which can be read out via a serial connection upon reception of an external trigger. The gain of the chip is adjustable over a range of $\approx$ 4.5 by two internal capacitors, which are, among other parameters, set by an external APC controller. Even though the dynamic range of $\approx$ 100 is lower than required, at the lowest gain setting only a small fraction of the slow spectator protons will deposit an energy in the thick counter that corresponds to an overflow, and the reconstructibility of these events is still ensured.

As the readout system features no direct analogue output, the STC has to be triggered by an independent signal indicating a physics event. Depending on the physics process considered, this signal will be provided by one of the available HERMES triggers. In order to test the analogue response of the chip and to ensure a correct timing, the APC features a test pulse input, which is used to synchronize the STC events with the events in the HERMES spectrometer and to adjust the signal shaping parameters.

Once an event is triggered, the analogue pulses in the pipeline are shaped and then sent as a balanced signal from the APC to the HERMES data acquisition. Here, two CAEN V676 analogue–digital converters provide the signal digitization, whereby three 10–bit signals are stored in one 32–bit word. Given the sensitivity of 4 mV/channel for the ADCs, the APC parameters and the capacity of the Silicon wafers, the total theoretical sensitivity of the read–out system, i.e. the energy deposition per ADC channel, can be calculated [Ste:98b]. The results for the minimum and maximum gain settings of the APC are shown in table 3.2[1]. As the minimum ionization energy deposition of $\approx$ 50 keV in the thin counter corresponds to an ADC signal of only two channels for the minimum gain, a measurement

---

[1]Due to the different capacitance of the thin and the thick counters, the corresponding sensitivities differ as well.

of MIPs and spectator protons with the same gain setting will hardly be feasible.

| gain setting | thin counter | thick counter |
|---|---|---|
| minimum | 29.3 keV/ch. | 24.5 keV/ch. |
| maximum | 6.3 keV/ch. | 5.2 keV/ch. |

Table 3.2: Calculated sensitivity of the STC readout system for for the minimum and maximum gain settings of the APC.

## 3.1.3   Mechanics

As discussed in section 3.1.1, the Silicon Test Counter consists of three separate detector modules. Hereby, each module incorporates the octagonal Silicon wafer, which is glued to a carrier board housing the front–end electronics for both sides of the detector. To minimize outgassing, a Kapton–coated copper plane is used for the carrier board. The layout of a complete module is displayed in figure 3.2.
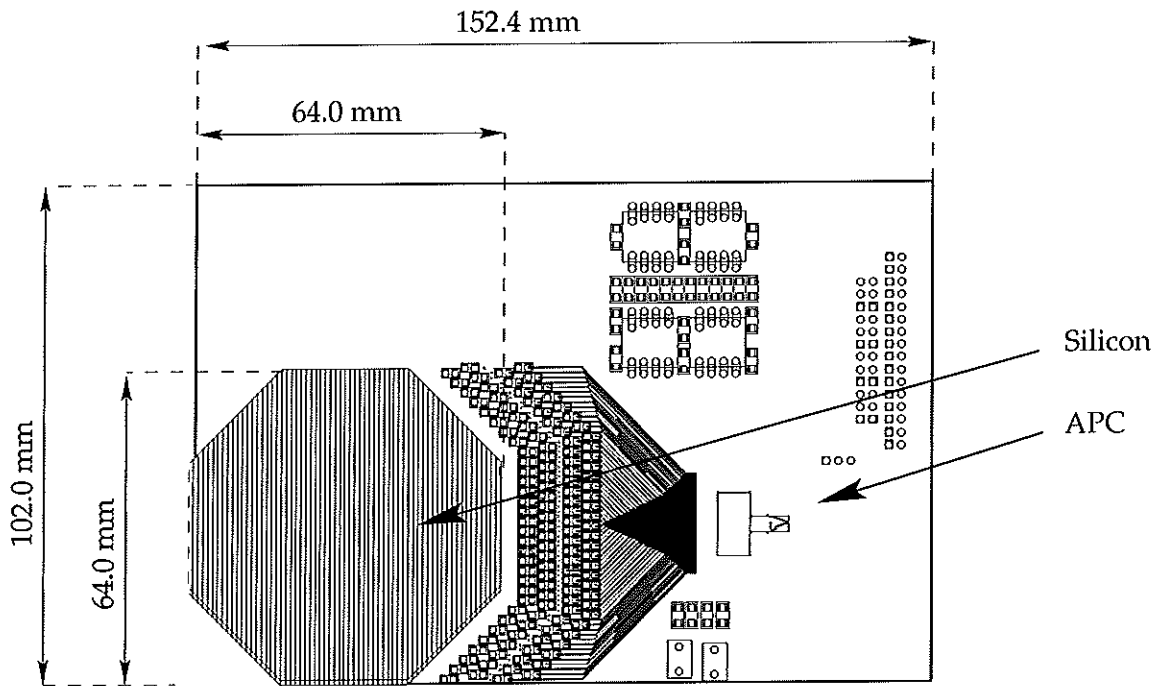


Figure 3.2: Layout of a single STC module, consisting of the carrier board with the front–end electronics and the Silicon wafer.

The readout electronics required for the STC data processing inside the vacuum area produce a total heat power of about 2.5 W. While this amount of heat could easily be dissipated using the storage cell cooling system, it is preferable for safety reasons to have an independent way of controlling the STC temperature. This is achieved by a set of Peltier elements, which are positioned outside of the target area vacuum and are thermally connected to the STC via a copper bar. The temperature at several positions on the carrier boards is monitored using UHV-compatible sensors.

The three modules are mounted inside a metal housing and aligned according to the specifications given in table 3.1. The part of the casing lid corresponding to the geometrical acceptance of the detector features an opening window covered by a thin copper mesh, thereby providing for an effective RF shielding. To avoid an obstruction of the HERMES spectrometer acceptance, the forward–facing part of the lid is slightly tilted. Using Kapton–coated twisted–pair wires, the counters analogue and control signals are lead to a vacuum feed–through. The design of the STC housing and the alignment of the modules inside is illustrated in figure 3.3. The fully assembled system is attached to the bottom of the HERMES target chamber underneath the storage cell.

## 3.2 Detector Tests

In order to demonstrate the functionality of the STC modules and the cooling system, a series of tests was carried out using a proton beam provided by the tandem accelerator at the University of Erlangen. The performed measurements included the calibration of the single modules, the study of incident angle effects and of energy deposition correlations between two modules. In this section, a short summary of the setup and the results is presented, while a detailed description can be found in [Wie:98].

### 3.2.1 Setup

The tandem accelerator at the University of Erlangen provides a proton beam with a high energy resolution in the energy range of about 4 MeV to 11 MeV. Using a series of apertures and quadrupole lenses, the beam current can be reduced to values of a few fA, while the beam diameter is in the order of 0.5 mm. For the STC tests, it was therefore possible to guide the beam directly onto the Silicon layers without the risk of radiation damage. A set of two dipole magnets allowed to vary the beam position in the horizontal and vertical direction, thereby scanning different detector strip combinations without changing the module positions. Figure 3.4 shows a schematic diagram illustrating the test experiment setup.

The Silicon modules were attached to the rotatable lid of a scattering chamber at the end of the proton beam line, which was evacuated to a pressure of about $10^{-6}$ mbar. To the side of the chamber, a Peltier cooling system identical to the one used at HERMES was
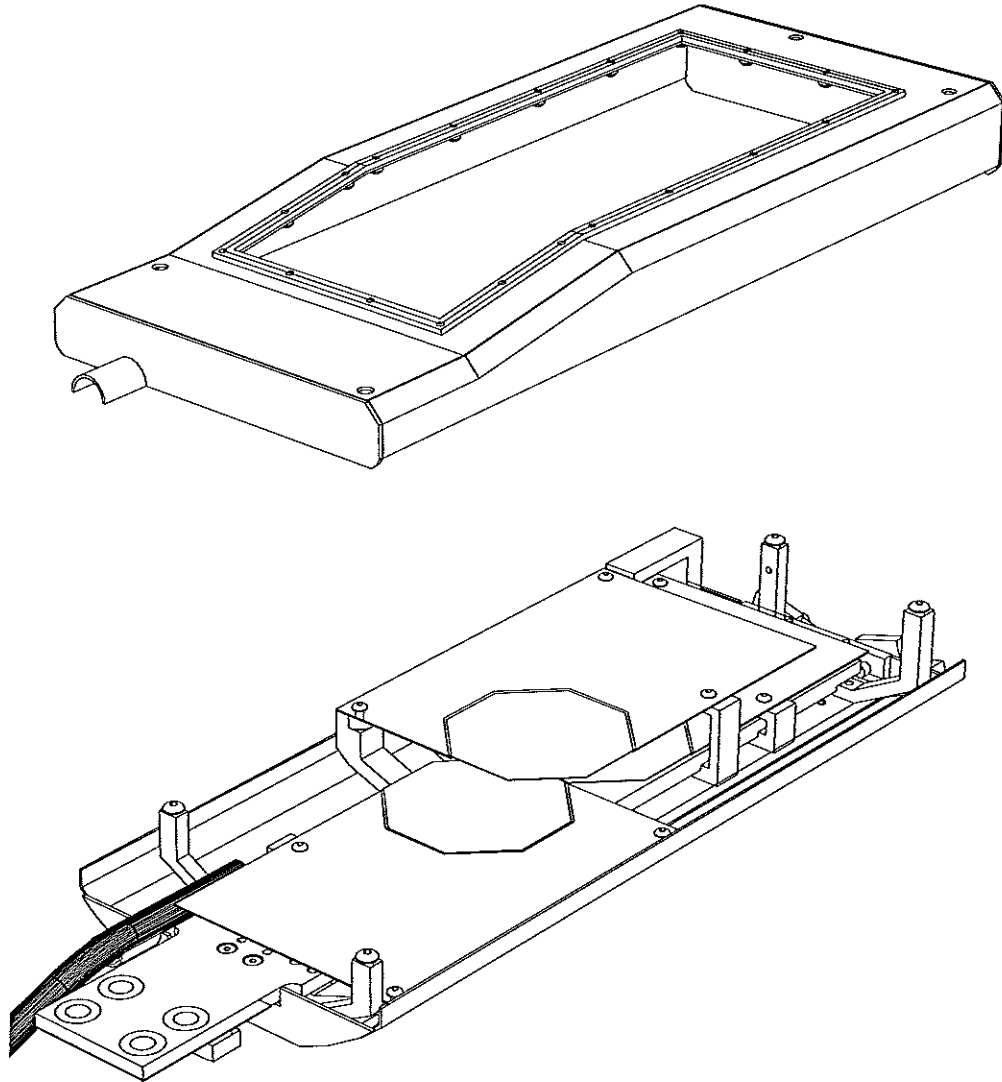
Figure 3.3: Design of the STC housing. The top part of the picture shows the lid with the opening window, while the bottom part displays the position of the modules. The bunched signal wires and the copper bar used for the heat transfer are also depicted.

attached, while the heat transport was realized using copper lace. Furthermore, the signal cables and the vacuum feed-throughs were of the final STC design.

Concerning the readout electronics, a different type of ADC as compared to the intended HERMES design had to be used. Also, as the STC modules have no self–triggering capability, a separate trigger detector had to be installed in the downstream area of the scattering chamber, thereby restricting the measurements to the case of particles travers-
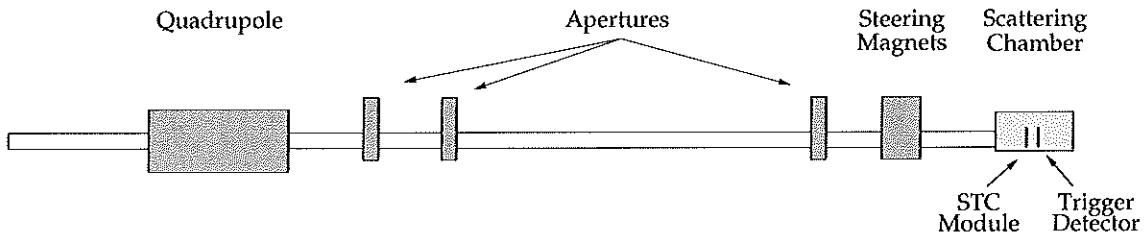
Figure 3.4: Schematic diagram of the test experiment setup (side view).

ing the Silicon layer. For reasons of vacuum compatibility and energy resolution, a further Silicon counter was chosen for this purpose.

The operation parameters of the STC modules were comparable to those encountered in the HERMES environment. The bias voltages corresponded to a full depletion of the detector, and the temperatures were in the range of 5–10 °C. Due to the high energy depositions expected in the available proton energy range, the measurements were carried out at the minimum gain setting of the APC. As the front–end chips of one of the thin modules malfunctioned, the measurements were carried out with one 135 $\mu$m–module and one 306 $\mu$m module.

## 3.2.2 Results

### Calibration and Energy Deposition

With the knowledge of the incident proton energy and angle, the theoretical energy deposition in a Silicon counter can be derived from parametrizations [BT:67], and an energy deposition calibration can be performed. Figure 3.5 shows the correlation between the calculated energy deposition and the detector response in ADC channels as measured for a detector of 135 $\mu$m thickness[2]. The observed linear dependence allows a determination of the average calibration factor to better than 2.5 % for the thin and 1.9 % for the thick module. As a result, it is found that the sensitivity of the ohmic side of a detector layer is only 90 % with respect to that of the junction side. This effect can be explained by the different recombination probabilities of holes and electrons in the Silicon wafer.

The measurement of the energy deposition correlation between a thin and a thick detector module is displayed in figure 3.6 in comparison to the theoretical prediction. As the experimental setup requires an external trigger, only the energy range corresponding to a particle traversing both layers can be investigated. While the data in the left plot are based on the assumption of fully activated detector layers, the right plot is corrected for passivation on the detector surfaces. By incorporating a passivated layer thickness of about 4 $\mu$m, a good agreement between measurement and theory can be achieved.

---

[2]Due to the use of different readout electronics, the calibration constants differ from those given in table 3.2
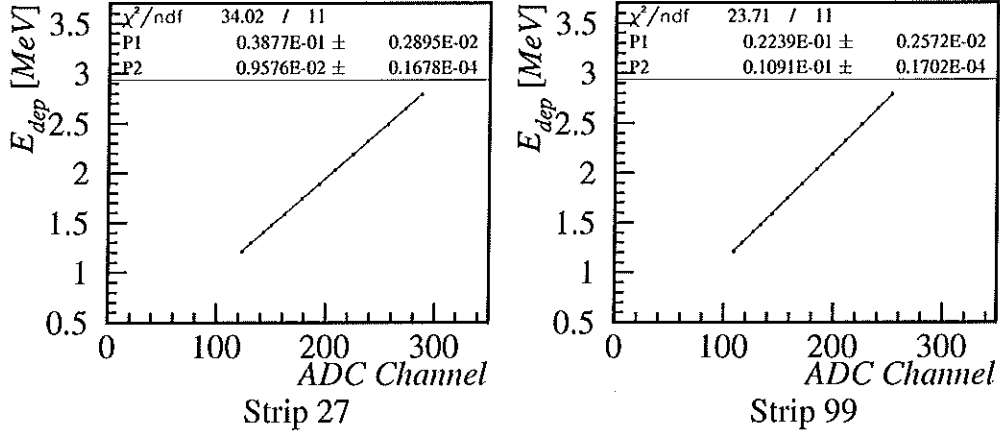
Figure 3.5: Energy deposition calibration as measured for a fixed impact position in a detector of 135 $\mu$m thickness [Wie:98]. The two different strip numbers correspond to the position on the ohmic and the junction side.
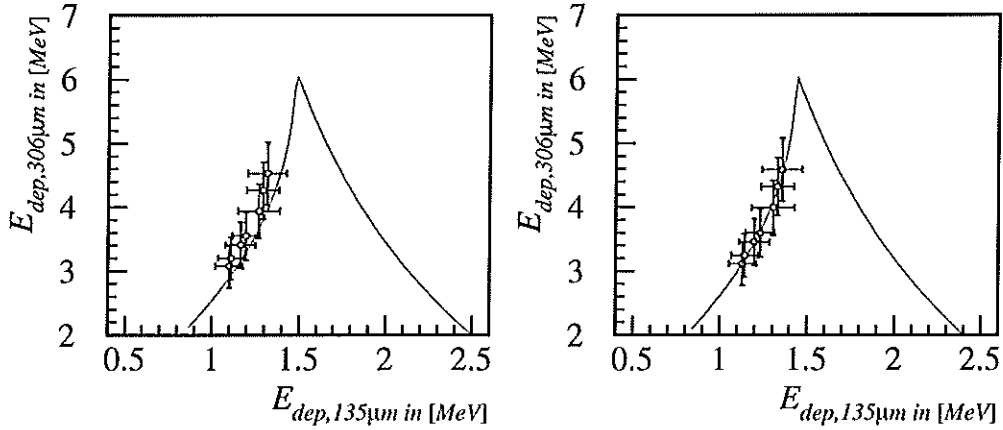


Figure 3.6: Correlation of the energy depositions in a thin and a thick module [Wie:98]. While the left plot assumes a fully activated layer, the right plot is corrected for passivation on the detector surfaces.

## Noise and Resolution

In [Ste:98b], a detailed analysis of the noise conditions encountered at the test experiment in Erlangen is presented. Using the calibration constants derived in [Wie:98], the contribu-

tions to the total noise in keV are shown in table 3.3. In general, the total measured noise is in the order of 20 keV and predominantly uncorrelated.

| thickness [$\mu$m] | side | $\sigma_{tot}$ [keV] | $\sigma_{uncorr}$ [keV] | $\sigma_{corr}$ [keV] |
|---|---|---|---|---|
| 306 | junction | 20.9 | 19.3 | 7.8 |
| 306 | ohmic | 19.6 | 17.7 | 8.4 |
| 135 | junction | 26.2 | 21.0 | 15.5 |
| 135 | ohmic | 24.2 | 22.5 | 8.8 |

Table 3.3: Summary of the noise measurements at the test experiment. $\sigma_{tot}$ denotes the total width of the baseline, while $\sigma_{uncorr}$ and $\sigma_{corr}$ specify the uncorrelated and correlated contributions.

Besides the noise contribution, the uncertainty in the relation between the energy deposition and the resulting ADC signal depends on a multitude of factors, which include energy straggling, detector resolution, angular uncertainty and thickness variations. While a detailed study of these contributions is presented in section 4.3.3, it can be stated that the signal width introduced by energy straggling alone dominates at roughly 80 keV for the thick and 35 keV for the thin counter against the noise levels given in table 3.3.

# 3.3  Monte Carlo Simulations

In analogy to the studies presented in section 2.2, the expected detector response of the Silicon Test Counter in the HERMES environment has been investigated using Monte Carlo techniques. The incorporated input consists of the storage cell with a wall thickness of 75 $\mu$m and the detector geometry discussed in section 3.1.1.

## 3.3.1  Spectator Yield

In the case of the STC, the events observed in the detector can be divided into three categories. Concerning hits in both horizontal layers of the counter (double hits), a signal in the top module can either be combined with a signal in the forward–facing thick module, or with a signal in the backward–facing thin module. While the yield for isotropic spectator particles should for symmetry reasons be the same in both cases, the number of detected fragmentation products and the energy deposition correlations are expected to differ. The third case of single hits is more difficult to approach, as the acceptance in the bottom layer is rather small, i.e. a straightforward distinction between a particle getting stuck in the top layer and a particle passing the top, but missing the bottom layer is not possible. Nevertheless, by using the HERMES $z$–vertex as an additional input information, a reconstruction of single hit events can be attempted.
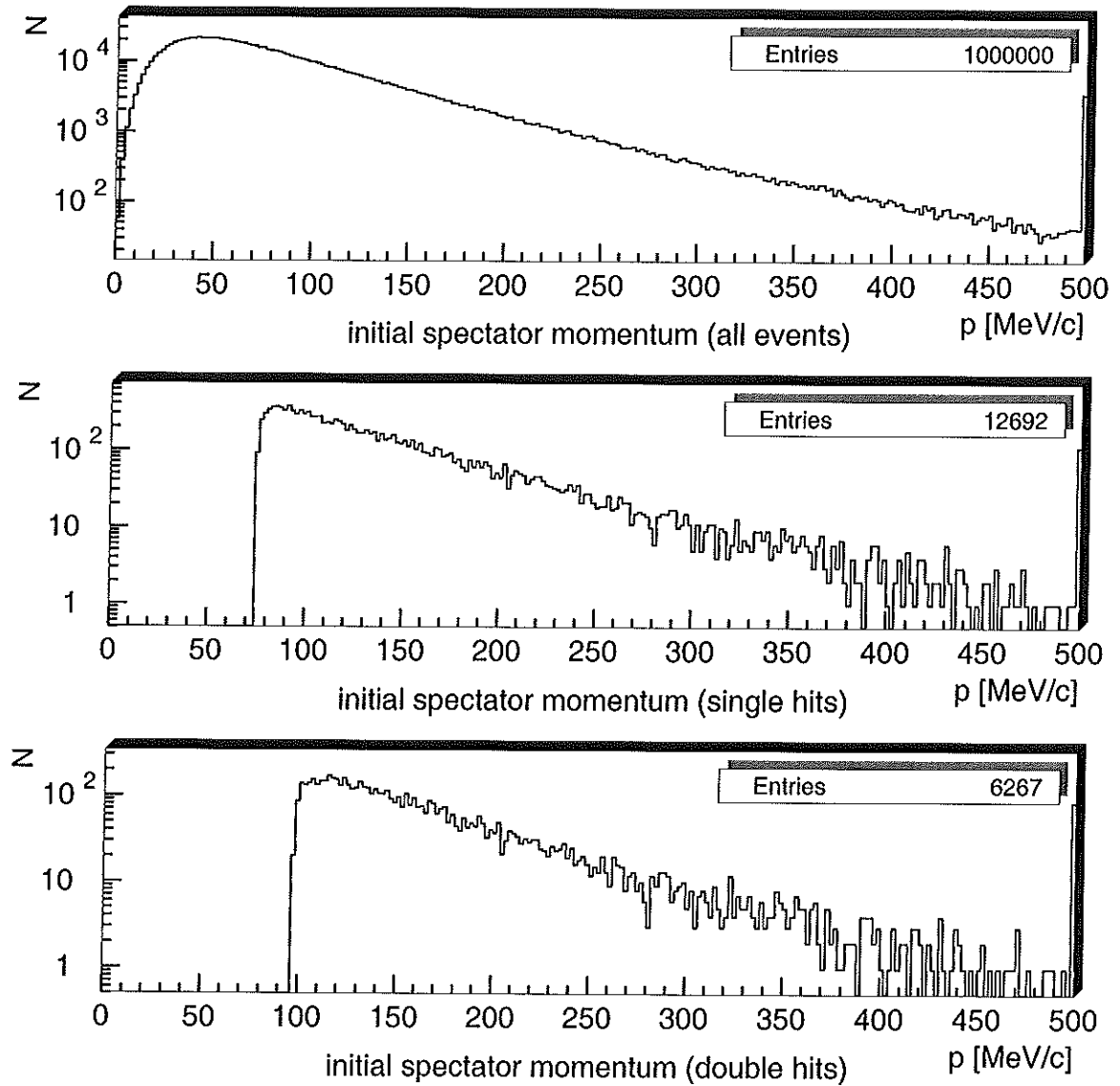
Figure 3.7: Initial momentum for detected pure spectator events in the STC.
Top: All generated events.
Middle: Single hits.
Bottom: Double hits.

For the case of pure spectator protons, the initial momentum spectra of the events reconstructible with the STC is shown in figure 3.7. The momentum threshold for single hits is $\approx 75$ MeV/c and increases to $\approx 100$ MeV/c for double hits. In comparison to the

values obtained for the full Recoil Detector (see table 2.2), the single hit threshold, which only depends on the storage cell wall thickness, is obviously unchanged, while the double hit threshold is increased by $\approx 10$ MeV/c due to the different thickness of the top layer.

The geometrical acceptance of the STC is determined to 3.1 % of $4\pi$ for the single hit case and 2.3 % of $4\pi$ for double hits. However, as mentioned above a reconstruction of the single hit events can only be achieved if the regarded event is also in the double hit acceptance. This has to be taken into account when calculating the spectator yields of the STC, which are summarized in table 3.4.

| Single hit total yield [%] | 1.1 |
|---|---|
| Double hit total yield [%] | 0.6 |
| Single hit momentum yield [%] | 40.1 |
| Double hit momentum yield [%] | 28.6 |

Table 3.4: Spectator proton yield normalized on the number of generated spectator protons for of STC.

The $z$–vertex and the angular distributions for detected spectator double hits in the STC are displayed in figure 3.8. The wide range of incidence angles covered allows to prove the reconstructibility of events under conditions which are similar to those encountered with the full HERMES Recoil Detector.

### 3.3.2 Fragmentation Products

Due to the forward–facing angular distribution of the fragmentation products in the DIS process, the corresponding double hit events in the STC are expected to be largely restricted to the combination of a signal in the top module and the thick bottom module. The resulting angular spectrum for the two possible combinations after the introduction of a MIP cut of $\Delta E_{thr} = 200$ keV for the thin counters and $\Delta E_{thr} = 450$ keV for the thick counter is shown in figure 3.9.

In the forward–facing module combination, 40 % of the events passing the MIP threshold in deep–inelastic scattering off $^2$H originate from fragmentation particles, while in the backward–facing combination, this fraction is reduced to less than 18 %. The STC is therefore a suitable device to study the separation of the spectator and the fragmentation process.

### 3.3.3 Energy Deposition

The two possible double hit combinations further allow the investigation of different energy deposition correlations and their effect on the achievable energy resolution. Figure 3.10 shows the two correlation plots as simulated for pure spectator events, whereby
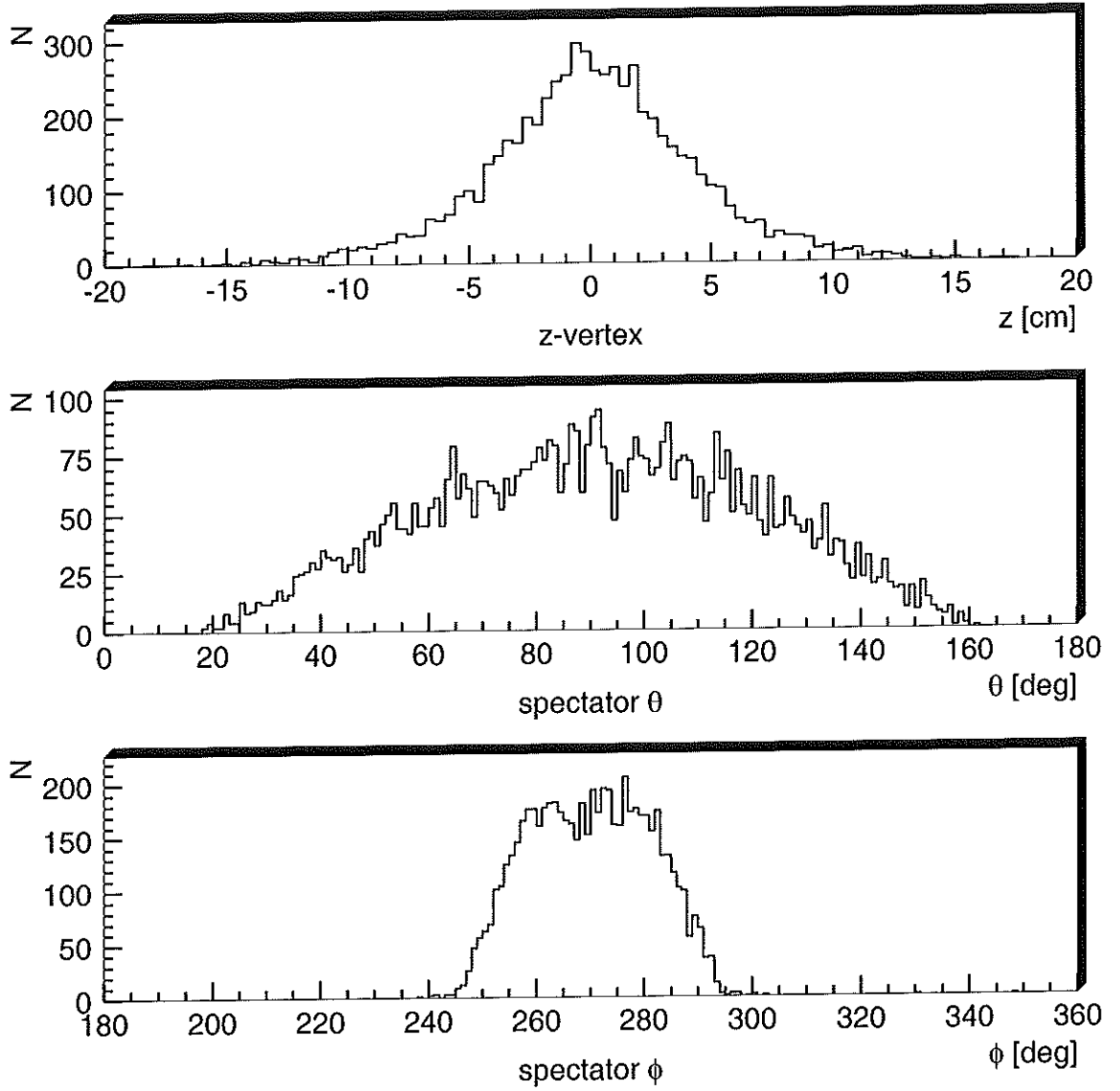
**Figure 3.8:** $z$–vertex and angular distributions for double hit spectator events in the STC.

the incident angle correction factor of $\cos(0.79 \cdot \alpha)$ is already applied. For the thin–thin combination, the energy deposition in the bottom counter is obviously reduced, and a higher fraction of the spectator events traverses both layers. On the other hand, the successful reconstruction of events in this setup would allow to reduce the required dynamic range of the employed front–end chip.
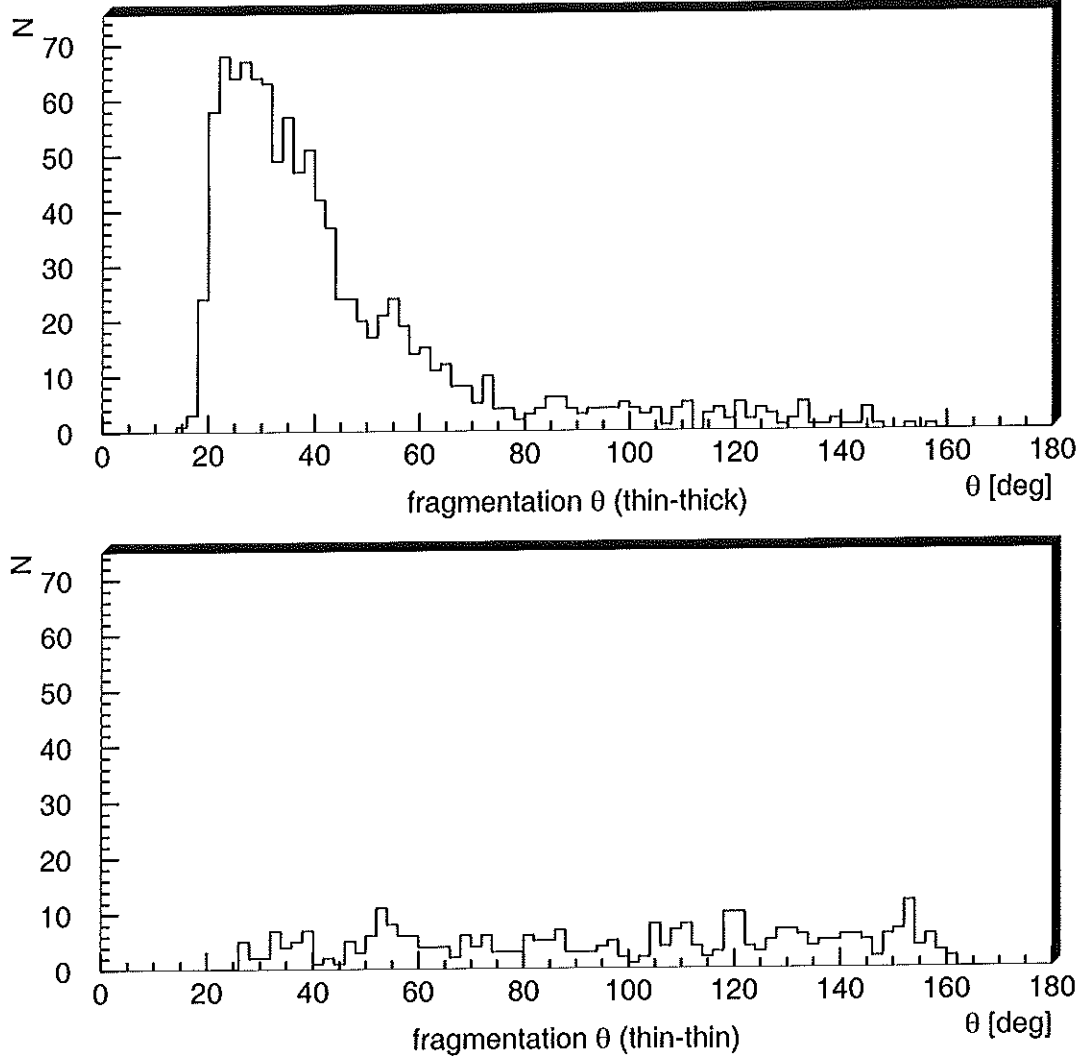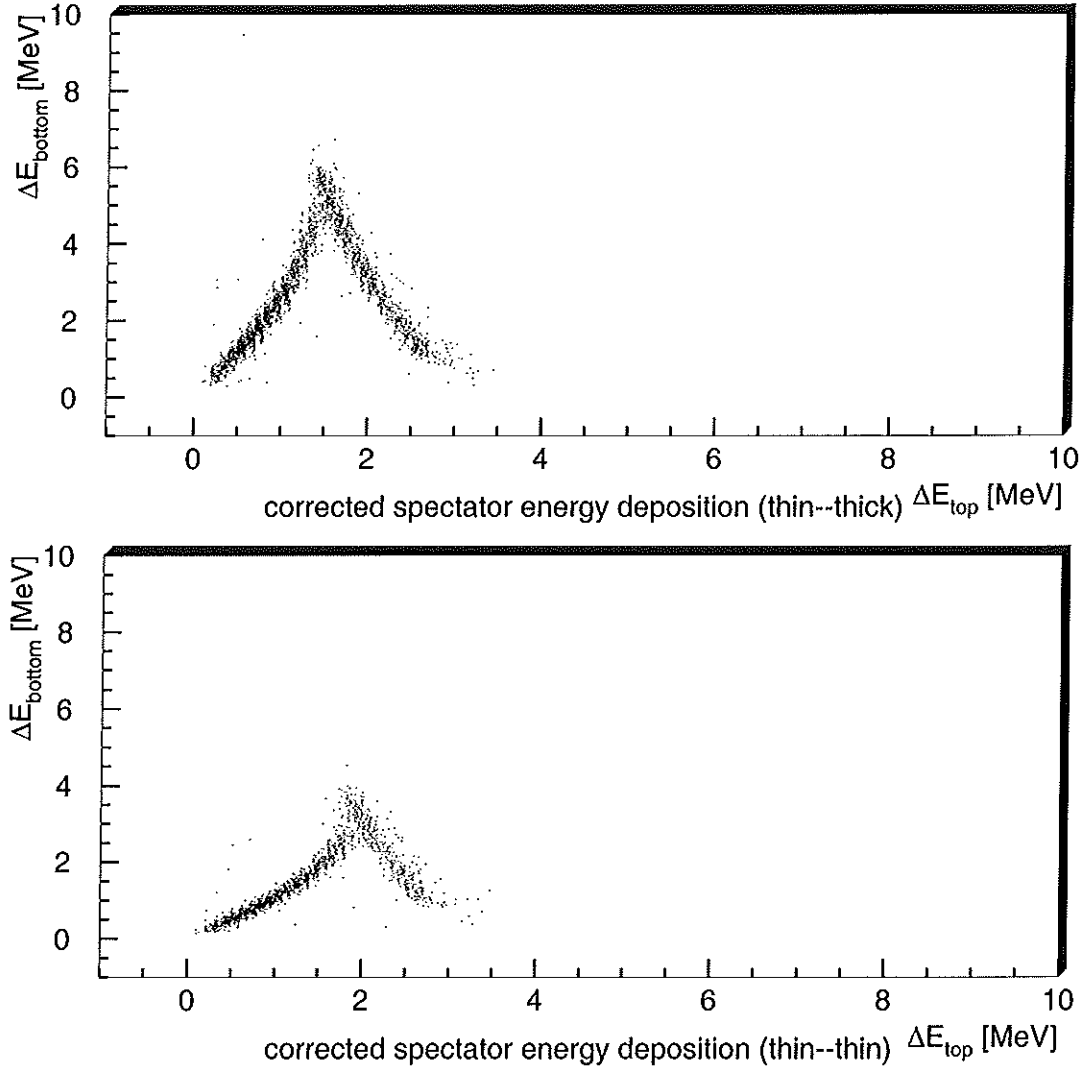
Figure 3.9: Angular distribution of detected double hit fragmentation events in the STC. The upper graph shows the forward–facing combination with a signal in the thick bottom detector, while the lower graph depicts the backward–facing combination with a signal in the thin bottom detector. An energy deposition threshold of $\Delta E_{thr} = 200$ keV for the thin counters and $\Delta E_{thr} = 450$ keV for the thick counter is applied.

Figure 3.10: Correlation of the energy depositions in the top and bottom layer of the STC for pure spectator proton events. The upper graph shows the forward–facing combination with a signal in the thick bottom detector, while the lower graph depicts the backward–facing combination with a signal in the thin bottom detector. The depositions are corrected for the particle incident angle, and an energy deposition threshold of $\Delta E_{thr} = 200$ keV for the thin counters and $\Delta E_{thr} = 450$ keV for the thick counter is applied.

# 4 First Results obtained with the STC

The Silicon Test Counter was installed in the HERMES target chamber in May 1998 and, after extensive tests, has been operated from August 1998 to December 1998. Section 4.1 summarizes the detector preparation and the operation parameters of the STC, while section 4.2 describes the event selection and the STC data production chain. The analysis algorithms and the first results obtained with the STC in scattering off $^1$H and $^2$H are presented in section 4.3.

## 4.1 Preparation and Operation

### 4.1.1 Vacuum Tests

Prior to the installation of the STC in the HERMES target chamber, extensive tests have been carried out to determine the out-gassing properties of the detector. For this reason, the complete counter was placed in the available HERMES transverse scattering chamber, which was connected to a mobile pump stand and evacuated to $\approx 10^{-7}$ mbar. Using an attached quadrupole mass spectrometer, the partial pressures of the residual gas could be monitored.

During the first pump-down, the total pressure in the chamber was dominated for a period of $\approx 100$ h by the partial pressure of $H_2O$, which can be explained by the large amount of Kapton used for the coating of the carrier boards and the signal wires. However, subsequent measurements revealed no noticeable difference in the total pressure and the mass spectra as compared to the data obtained with an empty vacuum vessel. Also, within the accuracy of the mass spectrometer ($\delta p \approx 10^{-10}$ mbar), no hydrocarbon out-gassing from e.g. the glue used in the detector production could be observed. The vacuum compatibility of the STC was further confirmed by independent measurements performed after its installation in the HERMES vacuum environment.

### 4.1.2 Electronics Adjustment

To obtain analysable results from the measurements with the STC, it is of utmost importance to have the readout timing correctly synchronized with the other components of the HERMES data acquisition. As the STC is not a self-triggering device and features no

direct analogue output, this can be achieved by determining the appropriate timing from the signal delay in the cables and in the various electronics modules used to generate a HERMES trigger pulse. However, given the short electron bunch distance of 96 ns in the HERA ring, it is desirable to have an additional real time observable to confirm the correct timing.

Using the coincidence of a pair of scintillators installed in close proximity to the HERMES target vessel, a signal with a well–known ($\delta t \approx 10$ ns) delay and a precise synchronization with the HERA electron bunches was obtained. By triggering the test pulse input of the APC synchronously with this signal, the correct STC timing setup can be determined in dependence on the trigger delay. A straightforward measurement of the difference in time between the scintillator signal and the HERMES physics trigger then pinpoints the correct timing for the implementation of the STC in the HERMES readout.

## 4.1.3  Detector Operation

After the installation of the STC and the first electronics tests, only three of a total of six APC units proved operational. Furthermore, the output of one chip provided only half of the balanced analogue signal, which resulted in a significant increase in electronics noise for the corresponding detector side. The most likely cause of these faults is the direct connection of the signal cables to the APC output, which makes the system susceptible to static charge building up in the dry air of the HERMES environment. In the design of the HERMES Recoil Detector, a safety measure like a decoupling output driver therefore has to be implemented.

The two fully operational APCs belong to the ohmic and the junction side of the top module, which is therefore completely functional and provides information about the $x$– and the $z$–coordinate of a detected particle. Furthermore, the ohmic side of the thick bottom module gives an analysable signal, i.e. a second $x$–coordinate is available. As the determination of the incident angle of a particle track largely depends on the polar angle given by the $z$–coordinates, the analysis of the STC data is clearly limited. Furthermore, the angular acceptance of the operational module combination is biased in the forward direction, which results in a more difficult separation of spectator protons and fragmentation products (see section 3.3.2). However, by using the additional input of the HERMES $z$–vertex, it is nevertheless possible to extract significant results from the collected data.

During the operation of the counter, the cooling system was set to a nominal temperature of $T_{set} = -10$ °C, which due to the influence of the target cooling resulted in an average actual temperature of $T_{avg} \approx -15$ °C under normal running conditions. Both modules were operated at double depletion voltages of 28 V for the top and 54 V for the bottom detector[1], which corresponds to bias currents of $I_{top} \approx 0.4$ $\mu$A and $I_{bot} \approx 1.0$ $\mu$A.

---

[1] As only the signals of two STC modules are analysable, the unequivocal terms of top and bottom module will be used in the following text.

The currents did not significantly increase over the data taking period, i.e. no deterioration of the Silicon resistance due to radiation damage could be observed.

### 4.1.4  Slow Control

In order to allow a direct monitoring of the STC operation parameters, a basic slow control system was implemented into the existing HERMES control setup. The observed quantities included the bias voltage and the detector temperature, which were charted on two real-time displays. Furthermore, an online representation of the ADC output for the different Silicon strips was made available.

If one of the observed parameters showed a significant deviation from the nominal value, an alarm was triggered to ensure a swift intervention. The following conditions were considered as critical:

- low bias voltage during HERMES operation,

- $I_{top} > 1\,\mu$A or $I_{bot} > 2\,\mu$A,

- $T_{avg} > 30\,°$C or $T_{avg} < -30\,°$C,

- HERMES target vacuum pressure $> 1 \cdot 10^{-4}$ mbar.

While a deviation from the nominal bias voltages and currents resulted in a notification of the shift crew and an automatic repetition of the turn–on sequence, the temperature and vacuum alarms led to an immediate shutdown of the STC operation. Apart from occasional current spikes induced by an accidental loss of the HERA electron beam, all above–mentioned parameters remained within the scheduled range during the STC operation period.

### 4.1.5  Collected Data

During the operation period of the STC, the HERMES experiment took data with both polarized and unpolarized targets. While in the polarized mode only Deuterium was used as a target gas, the unpolarized measurements were carried out with both Hydrogen and Deuterium. As the detection of spectator protons does not require a polarized target, the bulk of the data used in the following analysis is based on the scattering off unpolarized $^1$H and $^2$H.

The front–end chip used in the STC can be set to different amplification levels (see section 3.1.2), which are suitable for either resolving the low energy depositions induced by minimum ionizing particles or for providing the large energy deposition range required to detect slow particles. As the detection of spectator nucleons gives the opportunity to test the momentum reconstruction as well as the tracking capabilities of the STC, most of the data taking time was used for measurements in the minimum amplification setting.

| target | min. amplification | | max. amplification | |
|--------|--------------------|--------------------|--------------------|--------------------|
| type | # of runs | # of DIS | # of runs | # of DIS |
| unpol. $^1$H | 281 | 241729 | 188 | 228605 |
| unpol. $^2$H | 430 | 556520 | 220 | 344484 |
| pol. $^2$H | 1611 | 179427 | 0 | 0 |

Table 4.1: Number of runs and reconstructed DIS events collected with the STC for different target types and APC amplification settings.

A summary of the number of HERMES runs and reconstructed DIS events collected during the STC operation for the different target types is shown in table 4.1. It is noted that the data taking with the maximum APC amplification took place at the beginning of the 1998 HERMES running period and therefore coincided with tuning efforts on the HERMES spectrometer as well as the STC. The minimum amplification data used in the following analysis however were collected under stable detector conditions.

## 4.2  STC Data Production Chain

The STC is designed to prove the feasibility of operating a Silicon telescope in the HERMES vacuum environment. Therefore, the main focus is not on a stable data production under fixed conditions, but on the testing of the detector functionality. As the STC is furthermore positioned outside of the HERMES spectrometer acceptance, it is sensible to develop algorithms for the data production which are for the most part independent of the existing HERMES software.

In order to illustrate the individual parts of the STC production chain, section 4.2.1 firstly describes the software packages used for the processing of the HERMES spectrometer data. The decoding of the STC events is presented in section 4.2.2, while section 4.2.3 illustrates the event selection and the merging of the STC and HERMES data. Finally, section 4.2.4 focuses on the calibration of the energy depositions in the STC and the reconstruction of the particle tracks.

### 4.2.1  HERMES Data Production

Upon reception of a trigger signal, the output of the different components of the HERMES spectrometer is present in the form of channel numbers and digitized signals. This raw data is processed by the HERMES DAQ and stored in EPIO (Experimental Physics Input Output package) format on a hard disk, from where it is transferred to a tape robot system. Even though most HERMES detectors operate in zero–suppression mode, i.e. only signals which comply to a threshold condition are read out, the huge amount of resulting data ($\approx$

10 TB/a) has to be processed by a chain of analysis programs to reach a suitable format for the extraction of physics information. The following description is only intended to give a simplified overview of this process; for a more detailed presentation, see e.g. [Gut:99].

In a first step, the *Hermes Decoder* (HDC) converts the raw bit–stream signals into concrete information like positions and energy depositions. The resulting output is stored in ADAMO [PTG:94] format and passed via the client–server program *Distributed ADAMO* (DAD) to the *Hermes Reconstruction* program (HRC), which reconstructs the particle tracks using a tree search algorithm and determines momenta, scattering angles, particle types and other variables relevant for the physics analysis. The results are in turn passed to the *Alignment–Calibration–Efficiency* program (ACE), which computes the efficiencies of the individual detectors and stores the event information in *Data Summary Tables* (DSTs) on a hard disk.

During the operation of the HERMES spectrometer, the slow control data containing the parameters of the individual detectors is recorded by several DAD servers. To synchronize this information with the generated DSTs, a separate slow control production is performed. As a final step, it is now possible to merge the crucial data of both productions in so–called $\mu$DSTs, which contain only the essential information and therefore allow an efficient physics analysis.

## 4.2.2 Decoding and Storage Format

As discussed in section 3.1.2, the raw data output of the STC with the three working front–end chips consists of 192 ADC channels, which have to be converted to positions and energy depositions. The HERMES decoder HDC is designed for exactly this task, and it is therefore used as far as possible. However, the test detector characteristics of the STC make it necessary to deviate from the standard HERMES implementation.

The HDC output for an energy deposition detector usually consists of an ADAMO table containing the raw ADC channels and signals as well as the calculated positions and energy depositions. This output format is not suitable for the STC, as many parameters like the baseline offset and the calibration factors can only be determined once the detector response is tested and well understood. Furthermore, it is not advisable to apply a fixed threshold at this stage, as detailed studies of the baseline width are of high importance for the STC analysis. However, without zero–suppression the standard data format would result in a data volume of $\approx$ 400 MB per run and therefore $\approx$ 4 TB per year. Obviously, it is impossible to keep this amount of data for a single detector stored on hard disks, and an alternative solution has to be developed.

Especially with the lack of an independent $z$–vertex reconstruction, the physics analysis of an STC event is only possible using the additional information obtained from the HERMES spectrometer data. Given the fact that only a fraction of the triggered HERMES events corresponds to a reconstructible DIS event, it is sufficient to consider the STC data for this subsample. Furthermore, the determination of positions and energy depositions

can be performed at a later stage of the production, and the output has to contain only the raw ADC signals. An additional reduction in event size can be realized by a real–time compression of the decoded STC data.
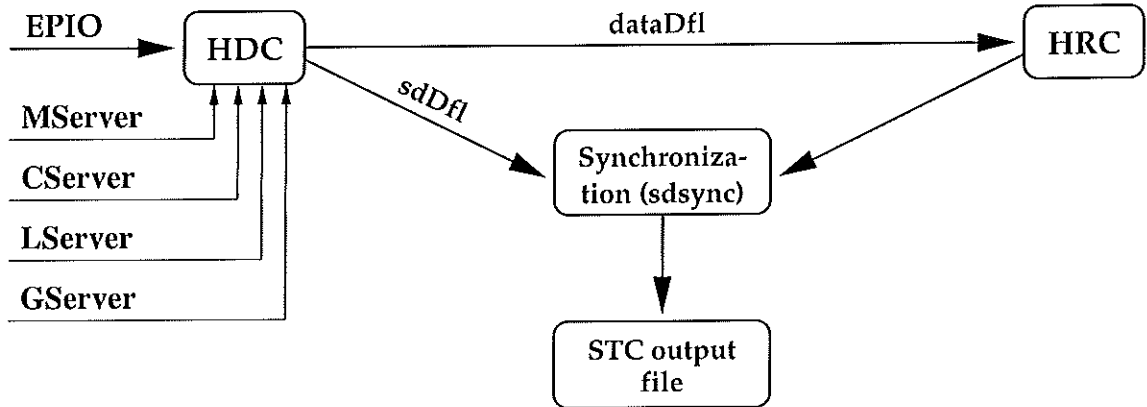


Figure 4.1: Decoding and synchronization of the raw STC data.

The chart in figure 4.1 illustrates the structure of the decoding stage of the STC production chain. The raw HERMES EPIO data is fed into HDC, while several DAD servers provide the relevant information concerning the electronics mapping (MServer), the calibration (CServer), the log file (LServer) and the geometry (GServer). For the case of the STC, the calibration and geometry information is ignored, and only the decoding and output formatting is performed. After the EPIO data is processed, the HDC output is separated into the STC data flow (sdDfl) and the HERMES spectrometer information (dataDfl). The latter is then piped directly into the reconstruction program HRC, which in a first pass determines the analysable events. This event sample is then synchronized with the STC data flow using the program sdsync and written to hard disk as a per–run file in compressed DAD format. Using this technique, the STC data volume is reduced by about a factor of 100 to $\approx$ 4 MB per run. As the complete raw EPIO data is stored on a tape robot system, it is ensured that no irreversible loss of physics information can occur in the synchronization process.

### 4.2.3 Event Selection and Merging

Except for a preselection of potential HERMES DIS events, the STC data files produced in the decoding stage still contain the complete raw ADC output, which is inconvenient for a physics analysis. Therefore, in the next production step a baseline subtraction, a threshold application and an event–by–event merging with the HERMES $\mu$DSTs is performed. For

this purpose, the Silicon Data Extraction program (sdx) was developed, which in turn uses the output of several small software routines suited for the individual tasks.

## Baseline and Threshold

In order to enable the measurement of positive as well as negative analogue signals, the baseline of the employed ADCs is shifted to roughly the middle of the total range of 1024 channels. To correct for this offset, the baseline position is determined individually for each STC strip by applying a Gaussian fit to the ADC spectrum taken with a non–physics pulser trigger[2]. Allowing for potential shifts in the baseline, this procedure is performed for each HERMES run, and the output is stored for subsequent use by the sdx program. The corrected ADC signals obtained by subtracting the baseline values from the raw ADC signals are directly proportional to the energy deposition in the detector module.

The threshold applied to the corrected ADC values is derived from the $1\sigma$ standard deviation of the Gaussian baseline fit. In the case of the analysis of slow spectator and fragmentation products, the total noise corresponding to the baseline width is small in comparison to the expected energy depositions. Therefore, the individual threshold assigned to each detector strip is set to $5\sigma$.

## HERMES $\mu$DST Analysis

For the physics analysis of the STC data, only those events are of interest which correspond to a reconstructed HERMES event. Furthermore, the STC track reconstruction has to rely on the $z$–vertex determined by the HERMES spectrometer. Thus, an analysis of the HERMES $\mu$DSTs is performed, which selects a physics process and stores the event identification parameters as well as the event information relevant for the STC analysis. At a later stage, sdx synchronizes the STC events with the output of the $\mu$DST analysis and merges the information of both sources.

For the analysis of spectator nucleon events presented in the following, the $\mu$DSTs are used to extract DIS events by applying the standard HERMES DIS cuts:

$$Q^2 > 1.0\,\text{GeV}^2, \quad W^2 > 4.0\,\text{GeV}^2, \quad y < 0.85, \quad |z_{vertex}| < 18.0\,\text{cm}, \quad |t_{vertex}| < 0.75\,\text{cm}.$$

Hereby, $t_{vertex}$ describes the transverse distance of the vertex from the axis of the storage cell. Besides the event identification parameters, only the electron vertex information is implemented in the production output. However, is it easily possible to merge the analysed STC data with the complete HERMES $\mu$DSTs, thereby getting access to the complete physics parameters of the DIS process.

---

[2]Due to the small ratio of particle hits to baseline events in an individual strip, the difference between the baseline values based on a pulser trigger and a physics trigger is negligible.

## sdx Processing and Output

The general purpose of sdx is to process the decoded STC data in a way that allows a direct detector response analysis of the resulting output. To achieve this, the following features are provided:

- Selection of various input formats,

- Selection of the HERMES trigger,

- Application of thresholds,

- Subtraction of baselines,

- Synchronization and merging with HERMES data,

- Selection of various output formats.

sdx is written in the C programming language and, by the use of command line options, can easily be implemented in UNIX shell scripts. This allows to process the complete STC production chain without the need of further intervention. The sdx processing sequence depends on the selected options. In the following, the standard running of the STC production is described.

After the basic initializations and I/O calls, sdx reads the decoded STC data as well as the $\mu$DST analysis file of a single HERMES run. As the $\mu$DST event numbers are a subsample of the STC event numbers, a loop over the STC event numbers is initialized. Once a corresponding $\mu$DST event number is found, the baseline values are subtracted from the raw ADC signals and the result is compared with the threshold for each detector strip. In the case of an above–threshold signal, the corrected ADC values for all 64 strips of the corresponding detector side are written to the output. As a detector side is read out by one APC, the relaying of the complete information allows to correct for correlated noise at a later stage of the production chain.

Once the complete run is processed, all events complying with the synchronization and threshold conditions are stored together with the HERMES vertex information in an output file. Unless otherwise specified, instead of ADAMO the HBOOK Ntuple format is used for this purpose, which allows to use the widespread PAW analysis tool in the following stages. At this point, the STC data volume has been reduced to an easily handleable $\approx$ 500 kB per run. For the further analysis, the per–run files are sorted according to the HERMES target gas and the APC settings used in the measurement.

### 4.2.4  Tracking and Calibration

After the sdx stage of the STC production chain, the STC data are present in a compact form, which allows the extraction of the interesting event parameters like hit positions,

energy depositions and incident angles. Using this information, it is finally possible to perform an energy calibration and to reconstruct particle tracks, types and initial momenta. Due to the small data volume involved, these calculations can be carried out using the FORTRAN interpreter provided by PAW.

## Hit Positions and Tracking

The next step in the STC data production involves the selection of particle hits and the conversion of the uncalibrated ADC values into positions and energy depositions. Furthermore, the signals are corrected for correlated noise, and the incident angle $\alpha$ is determined from the particle track. This process is executed by the PAW macro mksum and uses the per-run sdx files as an input. The output is then summarized in one Ntuple corresponding to the complete data production for the considered target gas and APC settings.

As described in section 4.2.3, in the case of a potential hit in the STC the complete raw ADC data for the corresponding detector side is present in the sdx output file. By looping over the 64 ADC channels in a detector side, mksum selects the detector strip with the highest energy deposition and marks it as the hit position. A comparison of this so-called *maximum algorithm* with other hit selection procedures shows that the average multiplicity in a single STC module is $\approx 1$. Furthermore, the Monte Carlo studies discussed in section 3.3 evidence that a spectator proton induces a higher energy deposition than other sources, which justifies this simple approach. As an aside, it is mentioned that the availability of a $z$–vertex reconstruction in the STC would naturally allow a more sophisticated hit selection using the correlation with the HERMES $z$–vertex.

In figure 4.2, the ADC signals for a typical hit are displayed versus the ADC channel number for one detector side. As the charge induced by a particle traversing the Silicon layer is not fully collected in a single strip, the hit signal is determined by integrating the ADC signals over a range of $\pm 2$ strips from the hit position. Furthermore, the correlated baseline noise is calculated as the average signal of the remaining strips not used for the hit signal integration. With $s_i$ being the baseline–corrected ADC signal of strip $i$ and $h$ the strip number of the hit as determined by the maximum algorithm, the actual signal $s'_h$ used in the analysis is thus calculated by[3]

$$s'_h = \sum_{i=h-2}^{h+2} s_i - 5 \cdot \frac{\sum_{i=1}^{h-3} s_i + \sum_{i=h+3}^{64} s_i}{64 - 5} .$$

In the case of a hit occurring closer than two strips from the edge of a detector side, the signal integration range and the correlated noise correction are adjusted accordingly.

---

[3]As only half of the balanced analogue signal is present for the bottom ohmic side (see section 4.1), the baseline–corrected ADC value is in this case multiplied by two.
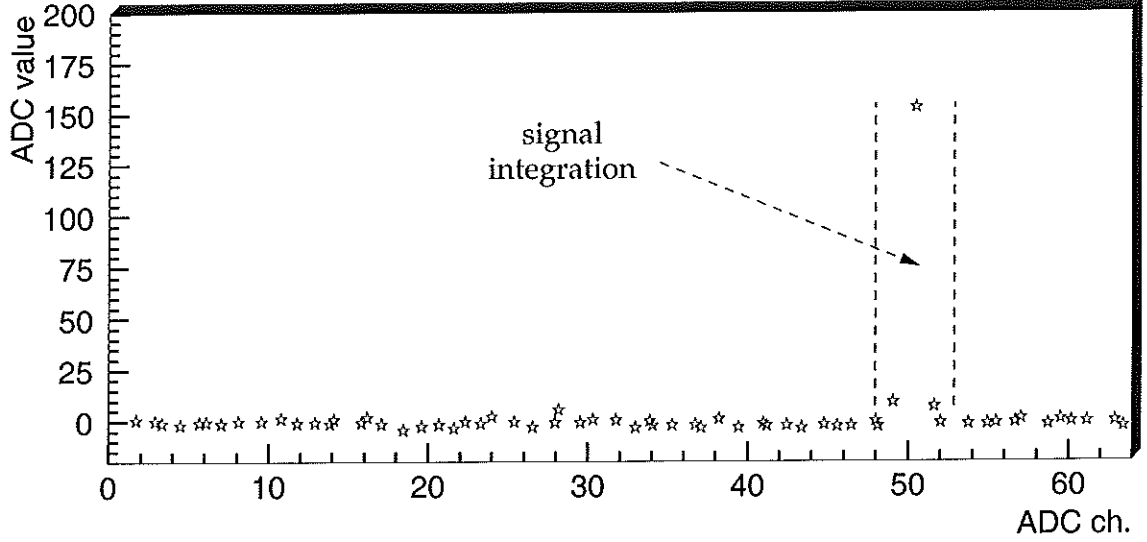
Figure 4.2: Determination of the ADC signal for a hit in a STC detector side.

After the determination of the strip numbers corresponding to a hit in the three detector sides, the geometric hit positions $x_{top}$, $z_{top}$ and $x_{bot}$ can be derived straightforwardly from the known position and orientation of the detector modules. In the case of a double hit, i.e. signals found in both the bottom and the top module, it is possible to reconstruct the $x$–vertex $x_v$ of the particle to

$$x_v = x_{bot} - \frac{\Delta y_t}{\Delta y_d} \cdot (x_{bot} - x_{top}) \,,$$

with $\Delta y_t = 6$ cm being the vertical distance between the top detector module and the centre of the storage cell, and $\Delta y_d = 1.5$ cm the distance between the bottom and the top detector module.

Due to the missing $z$–position in the bottom STC module, the more crucial determination of the $z$–vertex $z_v$ is alas impossible. However, by using the $z$–vertex information from the analysis of the HERMES $\mu$DSTs, a complete particle tracking can be achieved. This allows to reconstruct the impact angle $\alpha$ to

$$\alpha = \cos^{-1}\left(\frac{\Delta y_t}{\sqrt{(x_{top} - x_v)^2 + \Delta y_t^2 + (z_{top} - z_v)^2}}\right) . \tag{4.1}$$

In the case of single hits, only the information of the top detector is present and the angle reconstruction has to rely completely on the HERMES vertex information. Under the

assumption of $x_v = y_v = 0$ cm, the impact angle $\alpha$ is then given by

$$\alpha = \cos^{-1}\left(\frac{\Delta y_t}{\sqrt{x_{top}^2 + \Delta y_t^2 + (z_{top} - z_v)^2}}\right) . \tag{4.2}$$
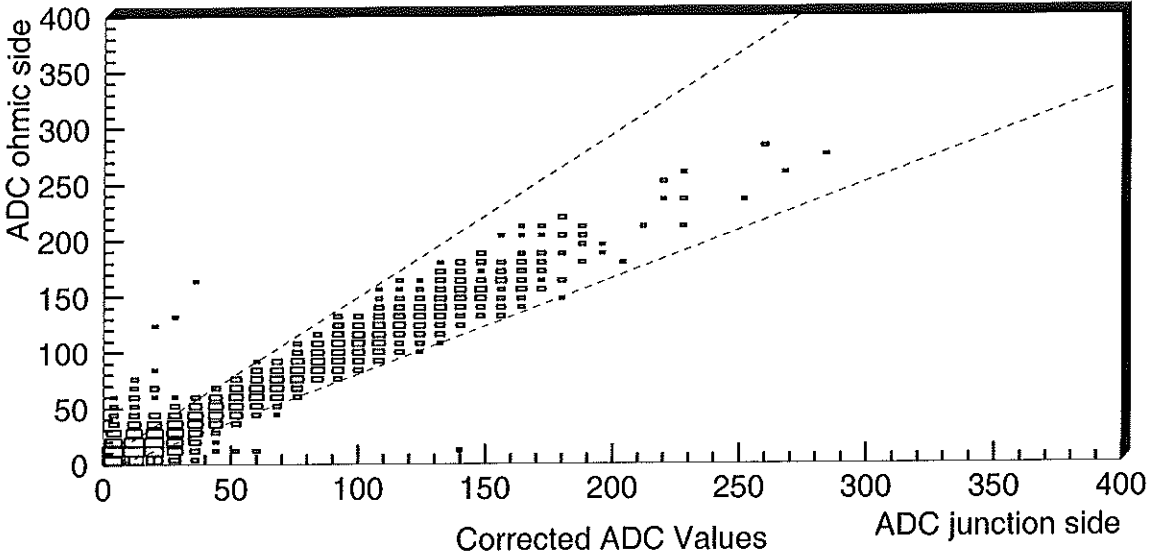


Figure 4.3: Correlation of the corrected ADC signals in the ohmic and the junction side of the top STC module in a logarithmic $z$-scale. The dashed lines indicate the correlation cut.

With the hitherto reconstructed STC detector information, it is possible to impose data cuts to remove event classes which are of background origin or otherwise unanalysable. As the ohmic and the junction side of the top STC module correspond to one Silicon wafer, the energy depositions and therefore the corrected ADC values of both sides have to show a linear correlation as displayed in figure 4.3. In the case of strong deviations from the expected dependence (see section 3.2), it therefore be assumed that the event cannot be analysed. This results in an empiric condition of

$$| s'_h(ohmic)/0.9 - s'_h(junction) | < (s'_h(ohmic)/0.9) \cdot 0.3 + 5 ,$$

as indicated by the dashed lines in the correlation plot. Furthermore, an event in the mksum production stage is only processed if a signal is present in either the top module or in the top and bottom module, i.e. single hits in the bottom module are removed.

**Energy Calibration**

To determine the calibration factor linking the energy deposition with the corrected ADC values, it is necessary to analyse the detector response to particles of known energy. While these measurements were carried out during the detector tests at the Erlangen tandem accelerator (see section 3.2), the different readout electronics used at HERMES may lead to deviations from the values quoted in table 3.2. Therefore, a new calibration is performed by means of the correlation between the proton–induced energy deposition in the top and the bottom module.

For a charged hadron of energy $E$ passing a Silicon layer of thickness $t$, the residual energy $E'$ can be parameterized [BT:67] to an accuracy of better than 0.1 % by

$$E' = \left( E^b - \frac{t \cdot \rho_{Si}}{a} \right)^{1/b} ,$$

whereby $\rho_{Si}$ is the density of Silicon and $a, b$ are constants for describing different particle types and energy ranges. The energy loss $\Delta E$ is then given by

$$\Delta E = E - \left( E^b - \frac{t \cdot \rho_{Si}}{a} \right)^{1/b} . \tag{4.3}$$

However, in order to compare the energy deposition correlation in the STC with the theoretical prediction, the relation $\Delta E_{bot}(\Delta E_{top})$ is needed. As equation 4.3 is a closed function, the inversion $E(\Delta E)$ is performed using an iteration process. From this, $E'(\Delta E_{top})$ and therefore $\Delta E_{bot}(\Delta E_{top})$ can be derived.

| detector side | calibration factor |
|---|---|
| top ohmic | 22.4 keV/ch. |
| top junction | 24.9 keV/ch. |
| bottom ohmic | 22.0 keV/ch. |

Table 4.2: Calibration factors for the STC energy deposition with a minimum APC gain setting as derived from a fit to the correlation of the measured proton energy deposition.

Prior to fitting the theoretical curve, the energy deposition correlation has to be extracted from the experimental data and corrected for the impact angle. A detailed description of this process can be found in section 4.3.2, while table 4.2 summarizes the resulting calibration factors. Using these values, the energy deposition in the top counter is given by the arithmetic mean of the ohmic and junction side signals.
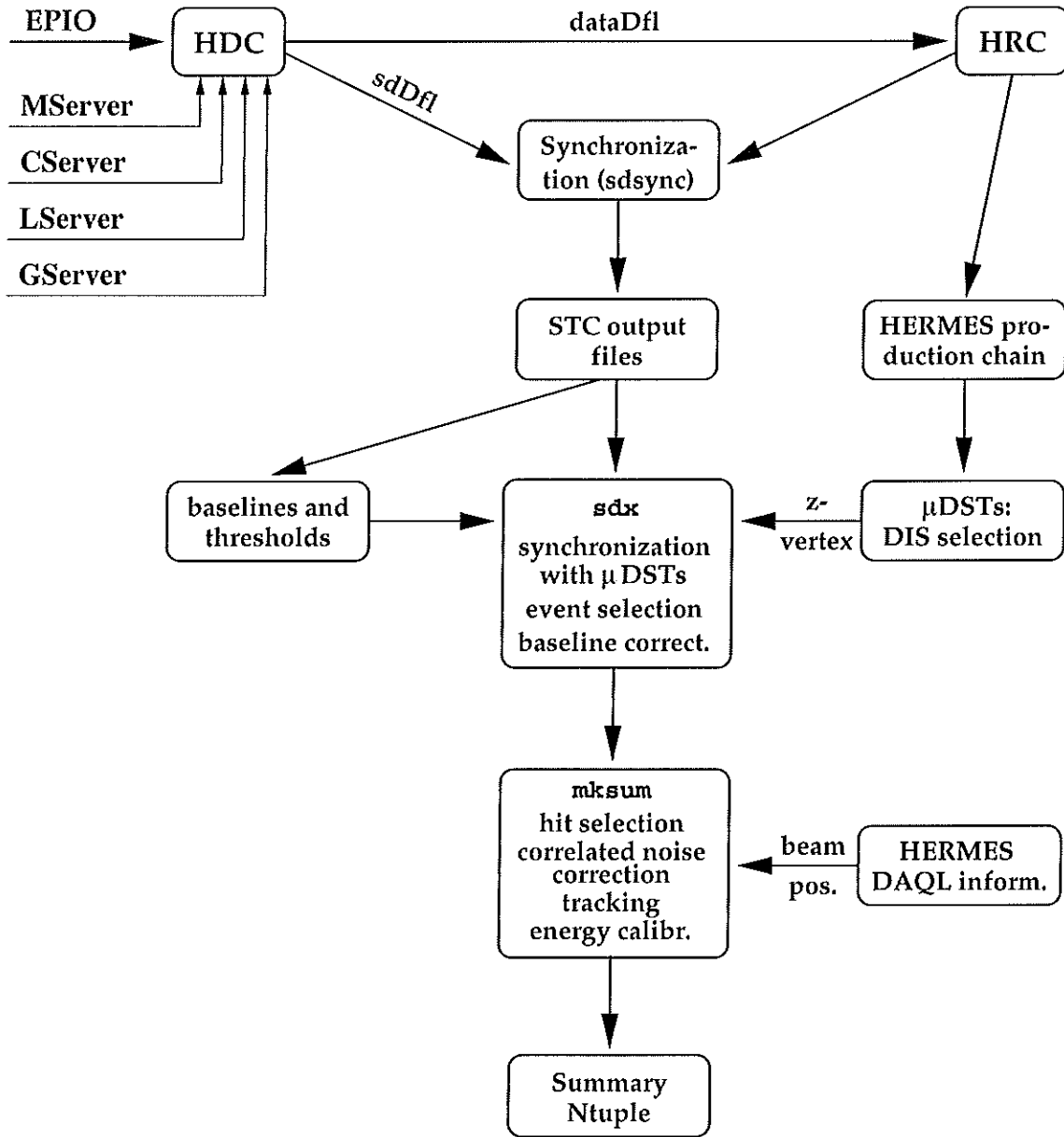
Figure 4.4: Schematic sequence of the STC data production chain.

After the hit positions and the energy depositions are determined, mksum stores these values together with the incident angle $\alpha$ in a compact summary Ntuple, from which the physics results can be extracted. Furthermore, part of the HERMES data quality (DAQL) information concerning e.g. the HERA beam position is added to allow subsequent sys-

tematic studies. A summarizing schematic chart of the complete STC data production chain is shown in figure 4.4.

## 4.3   Results from $^1$H and $^2$H scattering

In the following, an analysis of the 1998 STC data taken during the HERMES measurements with $^1$H and $^2$H targets is presented. To prove the tracking as well as the momentum reconstruction capabilities of the STC, the data sample corresponding to the minimum APC gain and therefore the maximum energy deposition range is chosen. This allows to verify the observation of spectator protons in scattering off $^2$H, while the $^1$H data give an insight into the low–energy domain of the fragmentation products in deep–inelastic scattering.

The general detector response and the resulting data cuts used in the analysis are described in section 4.3.1, while section 4.3.2 focuses on the energy deposition correlation between the top and the bottom module and section 4.3.3 gives an analysis of the noise and the energy resolution. Section 4.3.4 compares the measured distributions with the corresponding Monte Carlo predictions. In conclusion, section 4.3.5 illustrates the employed momentum reconstruction algorithm and shows the observed spectator proton momentum spectra.

### 4.3.1   Detector Response and Data Cuts

While the data files created by the STC production chain contain a calibrated summary of the STC events, only a few general requirements have been employed for the event selection at this stage. Therefore, it is necessary to develop a set of data cuts to ensure the separation of physics events and unanalysable background hits. As the spectator protons observed in deep–inelastic scattering off $^2$H are expected to induce a clean energy deposition signal in the STC, the results presented in this section are based on the unpolarized $^2$H STC data sample.

#### Thresholds

The events registered in the STC can be classified into single hits in only the top module and double hits in both detector layers. For the former case, the available information is limited to the coordinates of the hit, the corresponding energy deposition and the HERMES vertex position. A first indication of the detector response can be obtained from the correlation of the $x$– and $z$–coordinates in the top module, which is displayed in figure 4.5. The lefthand plot is based on the uncut production data and clearly shows the octagonal shape of the Silicon wafer[4]. However, a fraction of the events corresponding to the corners of the

---

[4]The empty channels at $x_{top} = 1.8$ cm are caused by a dead Silicon strip.
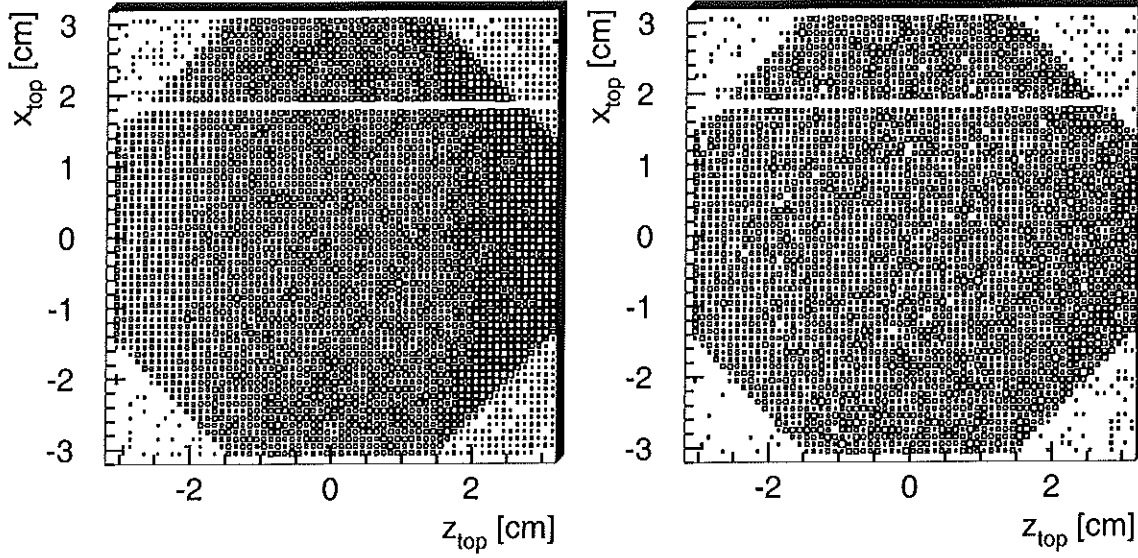
Figure 4.5: Correlation of the $x-$ and $z-$coordinates for a hit in the top detector module. The left-hand plot is based on the uncut production data, while in the righthand plot an energy deposition threshold of $\Delta E_{thr} = 300$ keV is introduced.

correlation graph represents geometrically impossible hit positions. To suppress this part of the single hit data sample induced by noise or a faulty reconstruction, an energy deposition threshold of $\Delta E_{thr} = 300$ keV is introduced for the top module. This results in the hit position pattern depicted in the righthand plot of figure 4.5. Together with the double hit cuts explained later in the text, a sufficient removal of the non–physical hits is achieved to allow an event reconstruction. However, as expected from the studies in section 2.2.3, in the case of pure single hits a more severe energy deposition cut of $\Delta E_{thr} = 800$ keV has to be applied.

Due to the missing $z$–coordinate, an equivalent correlation plot cannot be produced for the bottom STC module. However, it will be shown in the following that detector information accessible for the double hit condition provides for several other methods of cleaning up the data sample. Therefore, the energy deposition threshold for the bottom module is empirically set to $\Delta E_{thr} = 500$ keV. Unless stated otherwise, all subsequent results are based on this *threshold condition* T.

## Vertices

In the case of a double hit, i.e. if the *double hit condition* D of

$$\Delta E_{top} > 300 \text{ keV and } \Delta E_{bot} > 500 \text{ keV .}$$
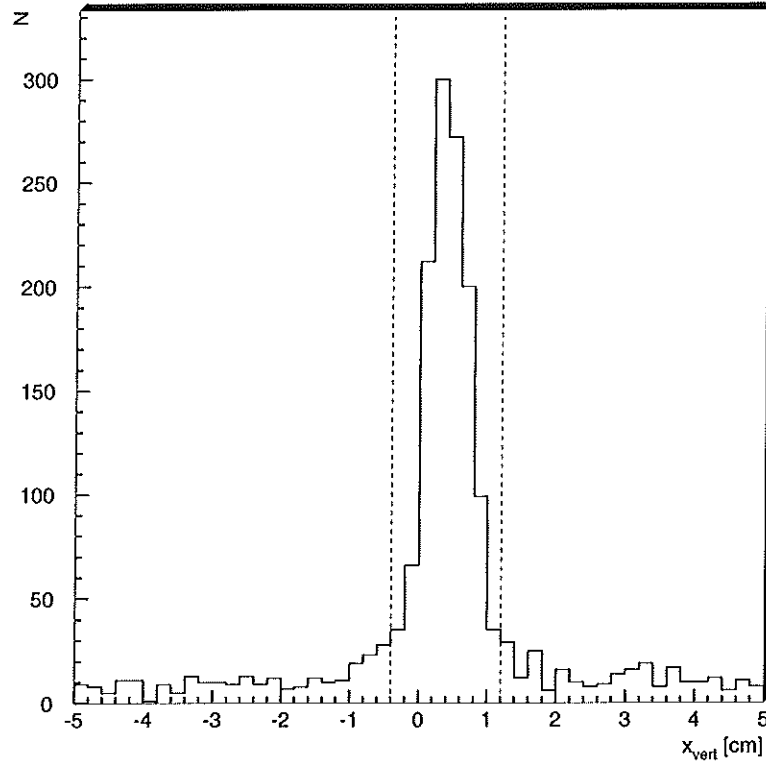
Figure 4.6: Reconstructed $x$–vertex $x_v$ for a double hit in the STC. The plot is based on the double hit condition D, while the dashed lines indicate the additional vertex condition V.

is fulfilled, the $x$–coordinates of the two STC modules allow the reconstruction of the $x$–vertex $x_v$ for the detected event. The resulting distribution is shown in figure 4.6. The plot, which is based solely on the double hit condition, shows a distinct peak at $\bar{x}_v = 0.4$ cm corresponding to the position of the HERMES storage cell[5] and a small, equally distributed baseline. To suppress the events in the latter part of the spectrum, a *vertex condition* V of

$$-0.4 \text{ cm} < x_v < 1.2 \text{ cm}$$

can be applied, which is indicated by the dashed lines in figure 4.6.

## Acceptance

In the case of two working $z$–layers in the STC, the correlation of the reconstructed $z$–vertex with the HERMES $z$–vertex would represent a powerful tool for selecting correctly reconstructed particle tracks. However, under the given conditions the STC analysis has

---

[5]The deviation from $\bar{x}_v = 0$ cm can be explained by the imprecise alignment of the STC.

to rely on the HERMES $z$-vertex information to allow a determination of the impact angle. As the possible vertex resolution from an STC reconstruction is significantly better than the HERMES vertex resolution, this results in a clear deterioration of the STC angular and momentum resolution.
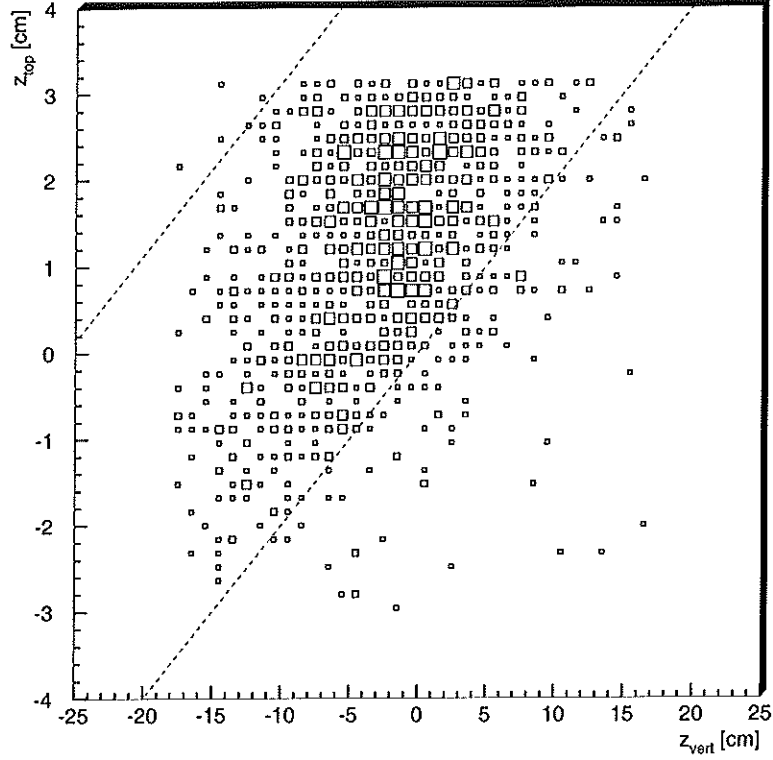


Figure 4.7: Correlation of the top module $z$-coordinate and the HERMES $z$-vertex for a double hit in the STC. The dashed lines in the plot, which is based on the D and V cuts, indicate the limits imposed by the geometrical acceptance.

In spite of this limitation, the geometrical acceptance of the STC for double hits allows to determine a theoretical range for the dependence of the top module $z$-coordinate on the HERMES $z$-vertex. The corresponding correlation, which also constitutes a verification of the crucial STC event synchronization with the HERMES data, is displayed in figure 4.7. While the basic shape of the plot is in accordance with the geometrical limits, a distinct shift along the $z$-axis can be observed. In section 4.3.2, a determination of this $z$-shift by means of the energy deposition correlation will be presented.

As indicated by the dashed lines in figure 4.7, an *acceptance condition* A can be applied to remove those events corresponding to a track outside of the STC geometrical acceptance. While this A cut has only a limited effect in the case of double hit events, it is proves as an important tool for selecting analysable single hits. In general, an exclusive

signal in the top module can correspond either to a particle traversing the first and missing the second layer, or to the desired case of a particle getting stuck in the first while being in the second layer acceptance. With the top detector hit coordinates and the HERMES vertex as an input, the latter sample can be selected by means of the acceptance cut.

### Standard Cuts

With the above considerations, a combination of four different data cuts can be employed to select the analysable STC events:

- Threshold Cut **T**

- Double Hit Cut **D**

- Vertex Cut **V**

- Acceptance Cut **A**

Table 4.3 summarizes the standard data cuts for the single and the double hit STC events as applied in the STC analysis.

| Hit Condition | Applied Cut |
|---|---|
| Single Hits | T and A |
| Double Hits | T and D and V |

Table 4.3: Standard data cuts for the single and the double hit events as applied in the STC analysis.

## 4.3.2  Energy Deposition Correlation

### Incident Angle Correction

Using the data cuts described in the previous section, the energy deposition correlation between the top and the bottom STC module can be extracted. The result for the unpolarized $^2$H data sample is illustrated in figure 4.8, which compares the correlation based on only a threshold cut (lefthand side) to the correlation after applying a further D and V cut (righthand side). While the basic triangular shape can already be anticipated, the energy depositions are smeared due to the lack of an incident angle correction.

However, in the correlation graph after multiplication with the empiric factor $\cos(0.79 \cdot \alpha)$, as displayed in figure 4.9, only a minor improvement in the smearing can be observed
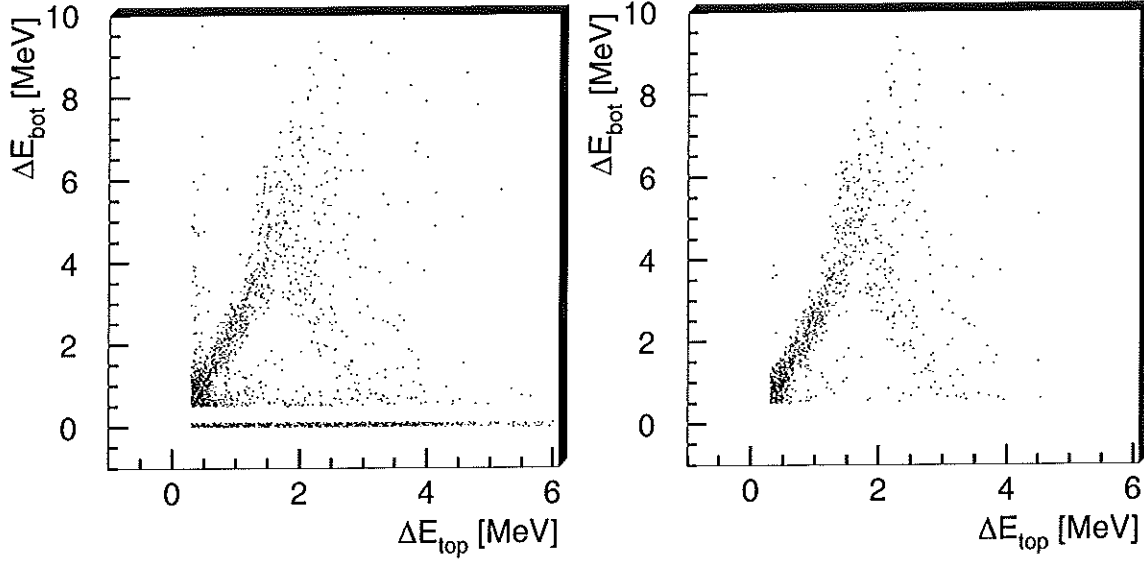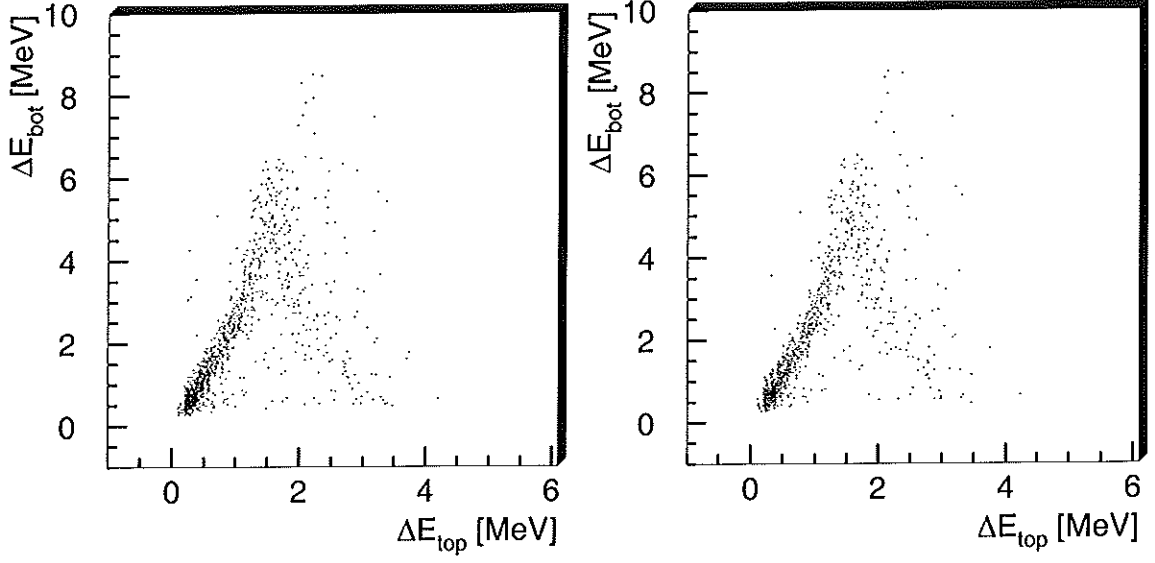
Figure 4.8: Correlation of the measured energy depositions in the STC top and bottom module for the unpolarized $^2H$ data sample. The lefthand plot is based on a T cut, while the righthand plot results from applying the standard (T and D and V) cuts.

for both the lefthand plot based on the (T and D and V) cuts and the righthand plots, for which an additional A cut is applied. This can be explained by the low angular resolution resulting from the missing $z$-vertex reconstruction and the consequential dependence on the HERMES $z$-vertex. Nevertheless, as the main part of the STC events consists of detected protons, the accuracy is sufficient to allow a particle identification.

## Particle Identification

The identification of the type of a particle traversing a Silicon telescope can be achieved by comparing the correlation of the energy depositions in the different layers to the theoretical predictions derived from parametrizations as in equation 4.3. This procedure can be illustrated by means of figure 4.10, which displays the angle–corrected correlation plot as measured with the STC to the theoretical curves for protons (dashed line) and deuterons (dotted line). Obviously, the clearest distinction can be achieved for the events corresponding to a particle traversing the top layer while being absorbed in the bottom layer. Even with the limited statistics gathered with the STC in this range, a consistence of the major fraction of the data sample with the proton curve can be observed, while a few isolated events are in accordance with the energy deposition of deuterons resulting from elastic scattering off $^2H$.

Figure 4.9: Incident angle–corrected correlation of the measured energy depositions in the STC top and bottom module for the unpolarized $^2$H data sample. The lefthand plot is based on the standard (T and D and V) cut, while for the righthand plot an additional A cut is applied.

After the removal of the deuteron events by means of a graphical cut[6], the event sample shown in figure 4.10 was used to determine the energy calibration given in table 4.2 by applying an unweighted two-dimensional fit of the proton parameterization to the correlation data.

In [B+:97], an analytical approach for the determination of the energy and mass resolution and therefore the particle identification properties of a Silicon telescope is presented. Based on the energy deposition parameterization given in equation 4.3, for the case of heavy ions a charge resolution parameter

$$\mu \equiv \left[ \left( \frac{A}{2} \right)^{b-1} Z^2 \right]^{1/(b+1)}$$

is introduced, which relates to the residual energy $E'$, the energy loss $\Delta E$ and the total layer thickness $t_{tot}$ as

$$\mu \propto \left[ \frac{(E' + \Delta E)^b - E'^b}{t_{tot}} \right]^{1/(b+1)} . \tag{4.4}$$

While the limited number of different nuclei detected in the STC does not necessitate

---

[6]In a graphical cut, a defined area of a two-dimensional histogram is selected or excluded.
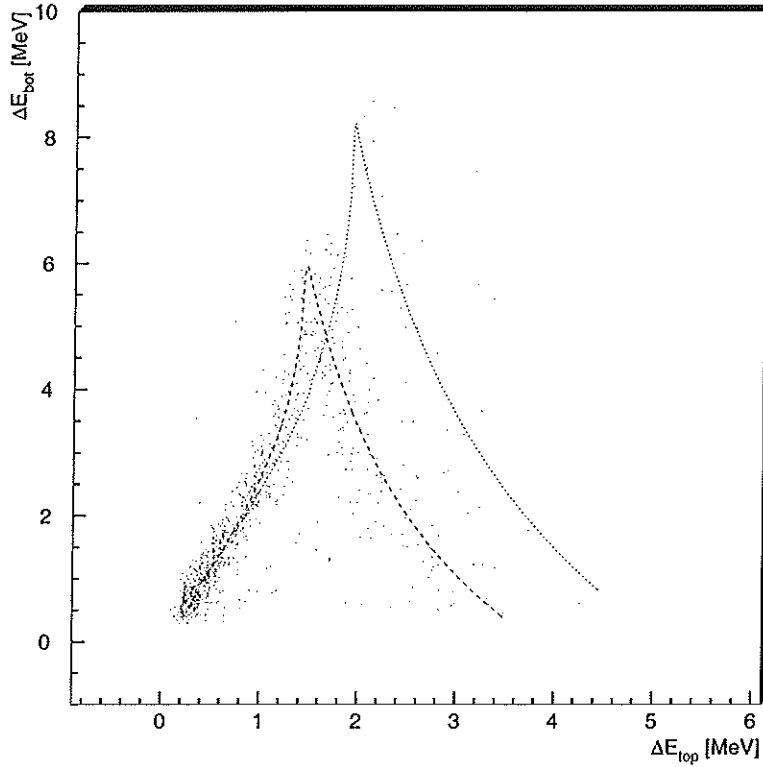
Figure 4.10: Comparison of the incident angle–corrected correlation of the measured energy depositions in the STC top and bottom module with theoretical predictions. The measured data shown in the plot is based on the (T and D and V and A) cuts, while the lines indicate the proton (dashed) and deuteron (dotted) energy deposition relations.

an analytical particle identification approach, the charge resolution $\mu$ can be utilized to determine the possible shift of the HERMES $z$–vertex relative to the STC [Ste:98a].

As the parameter $\mu$ only depends on the particle type traversing the Silicon Telescope, the standard deviation $\sigma_\mu$ reaches a minimum for the best possible angular correction of the energy deposition, which in turn depends on the correct HERMES $z$–vertex. By selecting those STC events corresponding to a proton stuck in the bottom layer and by using equation 4.4, the width of the resulting $\mu$–peak can now be determined in dependence on a theoretical shift $\Delta z_{vert}$ in the HERMES $z$–vertex. The results displayed in figure 4.11 clearly indicate that the best resolution of the STC data is achieved for $\Delta z_{vert} = +1.27$ cm and, as an aside, also prove the correct synchronization of the STC events with the HERMES data. Due to the lack of a fixed reference point, however, it cannot be concluded if this shift is due to a misalignment of the STC or a misreconstruction of the HERMES $z$–vertex. An accordant correction to the employed vertex information is used for the complete STC analysis and has already been implemented in the production of the energy deposition
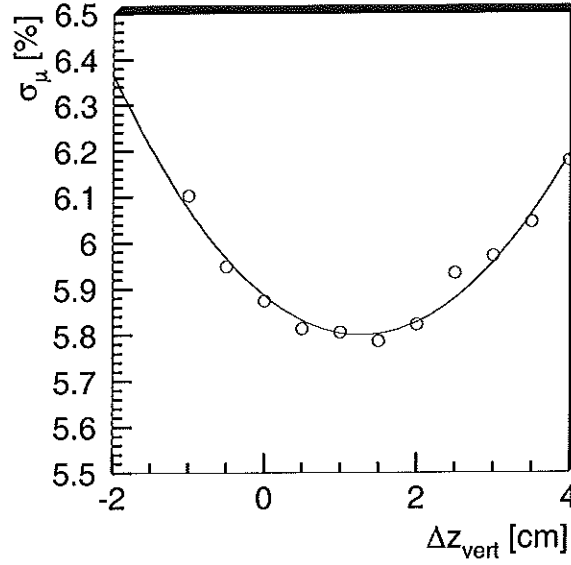
Figure 4.11: Dependence of the width of the $\mu$-peak for the STC proton data on the HERMES $z$-vertex shift $\Delta z_{vert}$. The width $\sigma_\mu$ reaches a minimum at $\Delta z_{vert} = 1.27$ cm [Ste:98a].

plots in this section.

### 4.3.3 Noise and Energy Resolution

The energy resolution of a Silicon detector is determined by a multitude of contributions, with the main broadening factors being the energy loss straggling, detector thickness variations and uncertainties in the incidence angle $\alpha$. Furthermore, the noise resulting from the electronics, signal pick–up and the Silicon has to be taken into account, whereas other effects like channelling or charge collection fluctuations are of minor importance. In the following, the influence of these contributions to the STC resolution will be quantified for the case of the minimum gain setting in the readout chip.

### Noise

As explained in section 4.2.3, the baseline width and therefore the total noise $\sigma_{tot}$ is determined during the STC data production on a per–run base. This allows to correct for time–dependent fluctuations of $\sigma_{tot}$ and furthermore gives access to an important data quality selection criterion. While the baseline width is analysed separately for each detector strip, the variation between the individual channels belonging to one readout chip is small. Therefore, the average $\sigma_{tot}$ corresponding to one detector side is used in the following calculations.
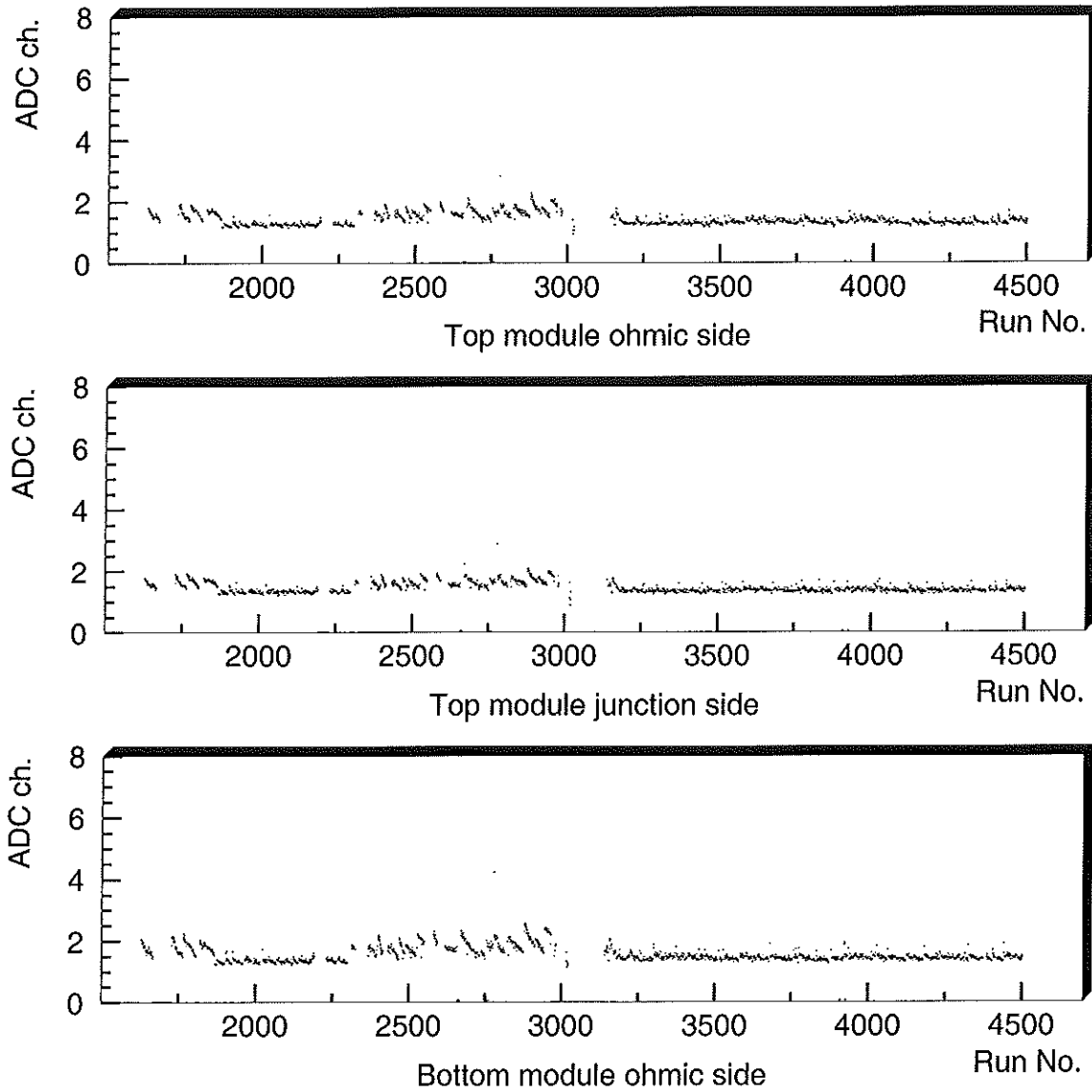
Figure 4.12: Average STC baseline width versus the HERMES run number for the three STC detector sides. The run number ranges of $\approx$(1850–2300) and $\approx$(3200–4500) correspond to the polarized operation of the HERMES target.

Figure 4.12 shows the average standard deviation of the baseline versus the HERMES run number for the three operational STC detector sides. While the general fluctuation of the baseline width is small, it is interesting to note that the variations are less pronounced in the run number ranges of $\approx$(1850–2300) and $\approx$(3200–4500), which correspond to the

polarized operation of the HERMES target. As the STC baseline width for the unpolarized target mode is furthermore correlated to the HERA electron beam current, this effect could be explained by the increased rate of Møller electrons in the STC resulting from the lack of a magnetic target holding field.

By projecting the noise values depicted in figure 4.12 to the $y$–axis, the average baseline width for each of the three detector sides can be determined in units of ADC channels. However, this quantity is not decisive for the energy resolution, as it consists of the quadratic sum of a correlated and an uncorrelated contribution:

$$\sigma_{tot}^2 = \sigma_{corr}^2 + \sigma_{uncorr}^2 .$$

To determine the relevant uncorrelated part, the standard deviation of the correlated noise correction as calculated in the mksum step of the STC data production chain has to be extracted. This can be illustrated by means of figure 4.13, which is based on the polarized HERMES runs and depicts the correlated noise correction values extracted for each STC event versus the HERMES run number for the three STC detector sides. Again, a Gaussian fit to the $y$–axis projection allows the determination of the average correlated noise contribution in units of ADC channels[7].

| detector side | $\sigma_{tot}$ [keV] | $\sigma_{uncorr}$ [keV] | $\sigma_{corr}$ [keV] |
|---|---|---|---|
| top ohmic | 29.7 | 28.6 | 7.9 |
| top junction | 37.8 | 35.8 | 12.2 |
| bottom ohmic | 62.5 | 61.5 | 11.1 |

Table 4.4: Summary of the STC noise analysis. The uncorrelated noise $\sigma_{uncorr}$ is calculated from the measured total noise $\sigma_{tot}$ and the correlated contribution $\sigma_{corr}$.

Using the calibration factors given in table 4.2, the total noise and the contributing factors can be converted to energy units, as summarized in table 4.4. A comparison with the noise measurements from the detector tests at Erlangen shows a general increase in the uncorrelated noise for the operation in the HERMES environment, while the readout of the bottom ohmic side is distorted by the lack of an operational balanced output for the analogue APC signal. Nevertheless, the present noise levels do not restrict the analysis of the STC data.

### Energy Straggling

As the energy loss of a charged hadron in matter is a statistical process, the corresponding energy deposition is subject to smearing. Therefore, a monoenergetic particle induces a

---

[7]The correlated noise is extracted at a different stage of the STC data production chain and therefore already includes the necessary multiplication of the ADC values for the bottom module by a factor of two.
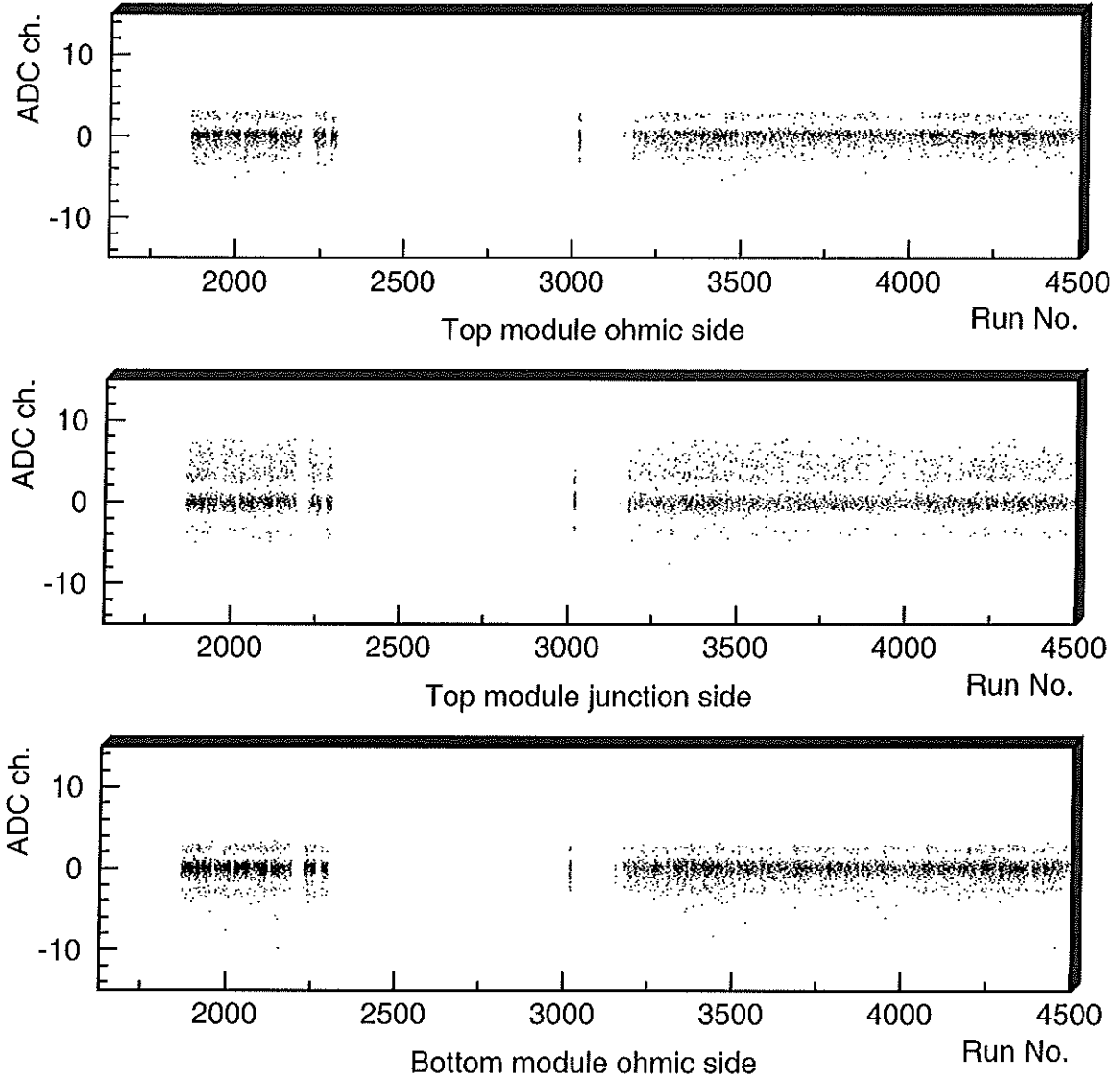
Figure 4.13: Correlated noise correction extracted for each STC event versus the HERMES run number for the three STC detector sides. The plots are based on HERMES runs corresponding to the polarized operation of the HERMES target.

distributed energy deposition with a straggling width of $\sigma_S$.

A theoretical approach to the determination of $\sigma_S$ is given by the Bohr variance [Boh:15]

$$\sigma_S^2 = \sigma_B^2 = 4\pi e^4 z^2 nZt \,, \tag{4.5}$$

where $z$ denotes the ion charge, $n$ the medium atomic density, $Z$ the atomic number and

*t* the traversed thickness. However, one of the conditions restricting the validity of equation 4.5 demands a constant particle velocity during the energy loss process. For common applications of Silicon telescopes, this condition is not fulfilled, which necessitates the solution of a more complicated integral equation by means of numerical methods.

A more convenient approach to the calculation of $\sigma_S$ is presented in [B+:97], where the deviation of $\sigma_S$ from the Bohr variance $\sigma_B$ is parameterized in the simple form of

$$\sigma_S = \sigma_B \cdot k \left( \frac{E'}{E} \right)^{-r} ,$$

with the fitting parameters $k$ and $r$ depending on the ion charge $z$ and the initial energy $E$.
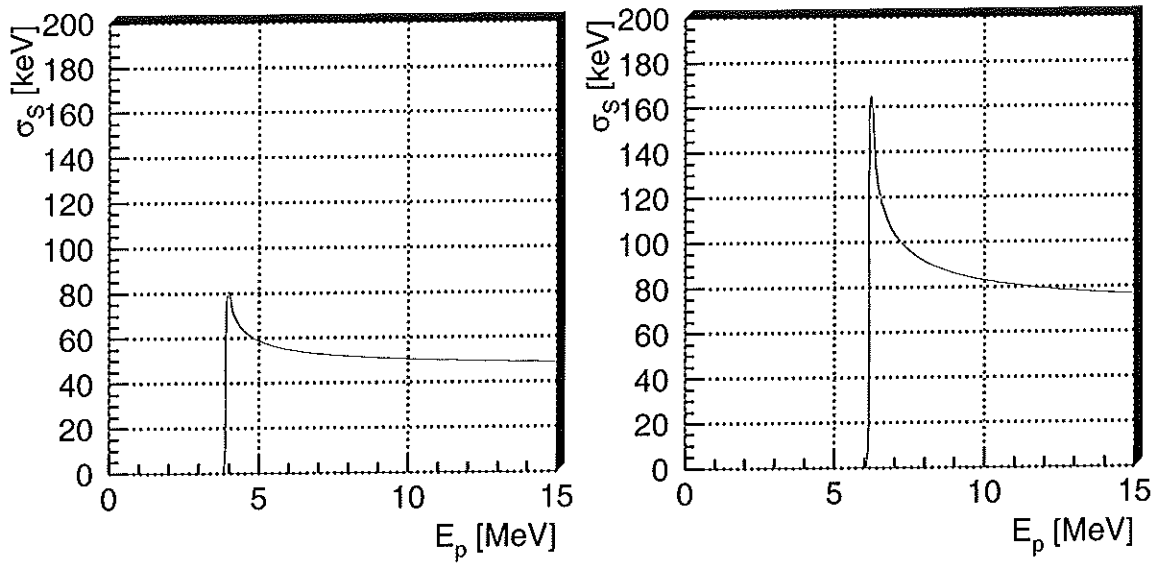


Figure 4.14: Energy straggling for protons in the STC for the thin (left) and the thick (right) detector module calculated from the parameterization given in [B+:97].

The resulting straggling width as calculated for protons in Silicon is shown in figure 4.14 for both the thin and the thick STC module. Typical spectator protons with an initial energy of $E_p = 9$ MeV deposit an average energy of $\Delta E = 1.3$ MeV in 135 μm of Silicon with a straggling width of $\sigma_S = 55$ keV, while for 306 μm of Silicon, the energy loss is $\Delta E = 3.2$ MeV with $\sigma_S = 83$ keV. These values indicate that energy straggling constitutes a major contribution to the total energy resolution of the STC.

## Angle Uncertainties

The dependence of the incidence angle $\alpha$ on the detector observables is given in equations 4.1 and 4.2 for the case of double and single hits in the STC. The total uncertainty $\delta\alpha$

consists of the contributions $(\delta\alpha)_\theta$ and $(\delta\alpha)_\phi$ arising from the scattering angle uncertainties $\delta\theta$ and $\delta\phi$. However, while $\delta\phi$ depends only on the uncertainty $\delta x$ in the measured $x$-coordinates, $\delta\theta$ is dependent on $\delta z$ as well as $\delta x$. It is therefore convenient to use the projected polar angle $\theta_{(yz)}$ and the corresponding contributions $(\delta\alpha)_{\theta_{(yz)}}$ and $(\delta\alpha)_\phi$, which are derived from equation 2.1 to

$$(\delta\alpha)_{\theta_{(yz)}} = -\frac{1 + \tan^2\theta_{(yz)}}{\tan^3\theta_{(yz)}\sqrt{\tan^{-2}\theta_{(yz)} + \tan^{-2}\phi}\left(1 + \tan^{-2}\theta_{(yz)} + \tan^{-2}\phi\right)} \cdot \delta\theta_{(yz)}$$

$$(\delta\alpha)_\phi = -\frac{1 + \tan^2\phi}{\tan^3\phi\sqrt{\tan^{-2}\theta_{(yz)} + \tan^{-2}\phi}\left(1 + \tan^{-2}\theta_{(yz)} + \tan^{-2}\phi\right)} \cdot \delta\phi .$$

With the given uncertainties $\delta x_{top,bot}$, $\delta z_{top}$ and $\delta z_{vert}$, the contributions $\delta\theta_{(yz)}$ and $\delta\phi$ can be determined to[8]

$$\delta\theta_{(yz)} = \frac{1}{\Delta y_t\left(1 + \tan^{-2}\theta_{(yz)}\right)} \cdot (\delta z_{top} + \delta z_{vert})$$

$$\delta\phi = \frac{1}{\Delta y_d\left(1 + \tan^{-2}\phi\right)} \cdot (\delta x_{top} + \delta x_{bot})$$

where $\Delta y_t = 6$ cm is the vertical distance between the top STC module and the target, and $\Delta y_d = 1.5$ cm is the vertical distance between the two modules. The total incidence angle uncertainty is then given by

$$\delta\alpha = \sqrt{(\delta\alpha)^2_{\theta_{(yz)}} + (\delta\alpha)^2_\phi} .$$

The above calculations are based on the detector observables available for a double hit in the STC, while for single hits the HERMES $x$-vertex $x_{vert}$ has to be used to determine $\phi$. As the influence of $\delta\phi$ on $\delta\alpha$ is small, the uncertainty $\delta x_{vert}$ is neglected in this case.

The uncertainties $\delta x_{top,bot}$ and $\delta z_{top}$ are given by the strip pitch in the STC modules to 0.5 mm, while $\delta z_{vert}$ can be determined to $\approx 2$ cm [Sto:99] for the 1998 HERMES running[9]. Based on these values, the angular resolutions $\delta\theta_{(yz)}$ and $\delta\phi$ for the angular range accessible with the STC are shown in figure 4.15. While the resolution in $\phi$, which is based on the two operational $x$-layers, is below 70 mrad, the resolution $\delta\theta_{(yz)}$ reaches values of almost 350 mrad. As the angular uncertainty directly influences the energy resolution, it becomes obvious that the lack of an independent $z$-vertex reconstruction severely restricts the accuracy of the STC analysis.

---

[8]While mathematically straightforward, the conversion of $\tan\theta_{(yz)}$ and $\tan\phi$ to the detector observables $x_{top,bot}$, $z_{top}$ and $z_{vert}$ restricts the legibility of the equation.

[9]The reconstruction of the 1998 HERMES data lacks the input of the HERMES Vertex Chamber information.
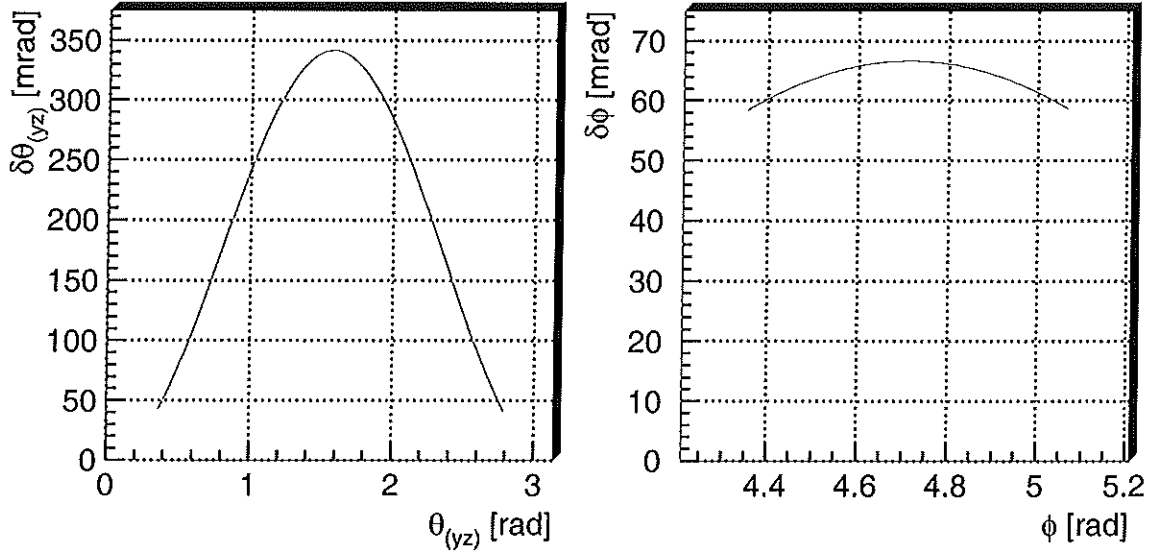
Figure 4.15: Angular resolutions $\delta\theta_{(yz)}$ (left) and $\delta\phi$ (right) of the STC based on the detector observables for a double hit.

By using the effective thickness $t' = t/\cos\alpha$, the propagation of the incident angle uncertainty $\delta\alpha$ to the energy loss uncertainty $\delta\Delta E$ can be derived from equation 4.3 to

$$(\delta\Delta E)_{angle} = \frac{t \cdot \rho_{Si}}{a \cdot b} \left( E^b - \frac{t \cdot \rho_{Si}}{a \cdot \cos\alpha} \right)^{\frac{1-b}{b}} \frac{\sin\alpha}{\cos^2\alpha} \cdot \delta\alpha .$$

The significance of this contribution can be illustrated by regarding a 9 MeV spectator proton traversing the thin STC module with an incidence angle of $\alpha = 45°$, depositing an energy of $\Delta E = 1.86$ MeV. The angular uncertainty in this case leads to an energy loss uncertainty of $(\delta\Delta E)_{angle} \approx 380$ keV, making this contribution clearly dominant in comparison to noise and energy straggling.

## Systematic Errors

The systematic errors having to be taken into account in the STC analysis include uncertainties in the energy calibration, the detector thickness and the total alignment.

As described in section 3.2, the accuracy of the energy calibration for the STC modules has been determined from the results of the dedicated measurements carried out at the Erlangen tandem accelerator. However, the different readout electronics employed at HERMES necessitate an adjustment of the calibration factors by means of the energy deposition correlation in the two detector layers. The error introduced by this process cannot be directly extracted from the fitting routine, as the inhomogeneous distribution of the

STC events on the deposition triangle distorts the result. Therefore, a conservative approximation of $\sigma_{calib} \approx 3$ % is used, which is added in quadrature to the measured factors given in table 4.4.

Another relevant systematic contribution to the energy resolution is the variation $\delta t$ in the detector thickness, which for the wafers used in the STC is specified [MIC:97] to $\delta t < 5$ $\mu$m. Using equation 4.3, the propagation to the energy loss uncertainty $\delta \Delta E$ can be calculated to

$$(\delta \Delta E)_t = \frac{\rho_{Si}}{a \cdot b} \left( E^b - \frac{t \cdot \rho_{Si}}{a \cdot \cos \alpha} \right)^{\frac{1-b}{b}} \cdot \delta t \ .$$

For the perpendicular impact of a 9 MeV spectator proton in the thin module ($\Delta E = 1.86$ MeV), the contribution to the energy deposition width resulting from thickness variations is $(\delta \Delta E)_t = 50$ keV.

The absolute alignment of the STC plays a subordinate role in the STC analysis, as only relative positions enter the particle reconstruction algorithms. The major impact on the systematic error results from the uncertainty in the average shift between the STC $z$-position and the reconstructed HERMES $z$-vertex, which can be determined by means of detector observables (see section 4.3.2). The remaining contributions from e.g. a shift in the $x$-position or a possible detector tilt are small in comparison to the experimental errors discussed above and are therefore omitted.

Finally, the parameterization given in equation 4.3 reflects the energy deposition only to a certain accuracy. While the subdivision of the initial energy into several small ranges allows to reduce the maximum deviation to less than 0.1 % [BT:67], the domination of other sources of uncertainty in the STC justifies to select a parameterization corresponding to $(\delta \Delta E)_{fit}/\Delta E < 1$ %.

### Total Energy Resolution

The total energy resolution in a STC module is given by the quadratic sum of the individual contributions discussed above, and the systematic error $\sigma_{calib}$ introduced by the energy calibration. However, a differentiation is necessary to allow for the different signal combinations found in the STC.

In the case of a single hit, i.e. of a particle being absorbed in the top STC module, the contributions from energy straggling, thickness variations and angular uncertainties do not add to the width of the energy deposition signal. Therefore, the total energy loss uncertainty $\delta(\Delta E)_{tot}$ is simply determined by

$$\delta(\Delta E)_{tot} = \sqrt{\sigma^2_{uncorr,top} + \sigma^2_{calib,top}} \ .$$

A similar approach is valid for the part of the double hit sample which corresponds to a particle traversing the top layer and being stopped in the bottom layer. As no correlation is

present between the top and the bottom module signal width, the energy loss uncertainty for the sum of the two depositions can be expressed as

$$\delta(\Delta E)_{tot} = \sqrt{\sigma^2_{uncorr,top} + \sigma^2_{calib_top} + \sigma^2_{uncorr,bot} + \sigma^2_{calib_bot}} \; .$$
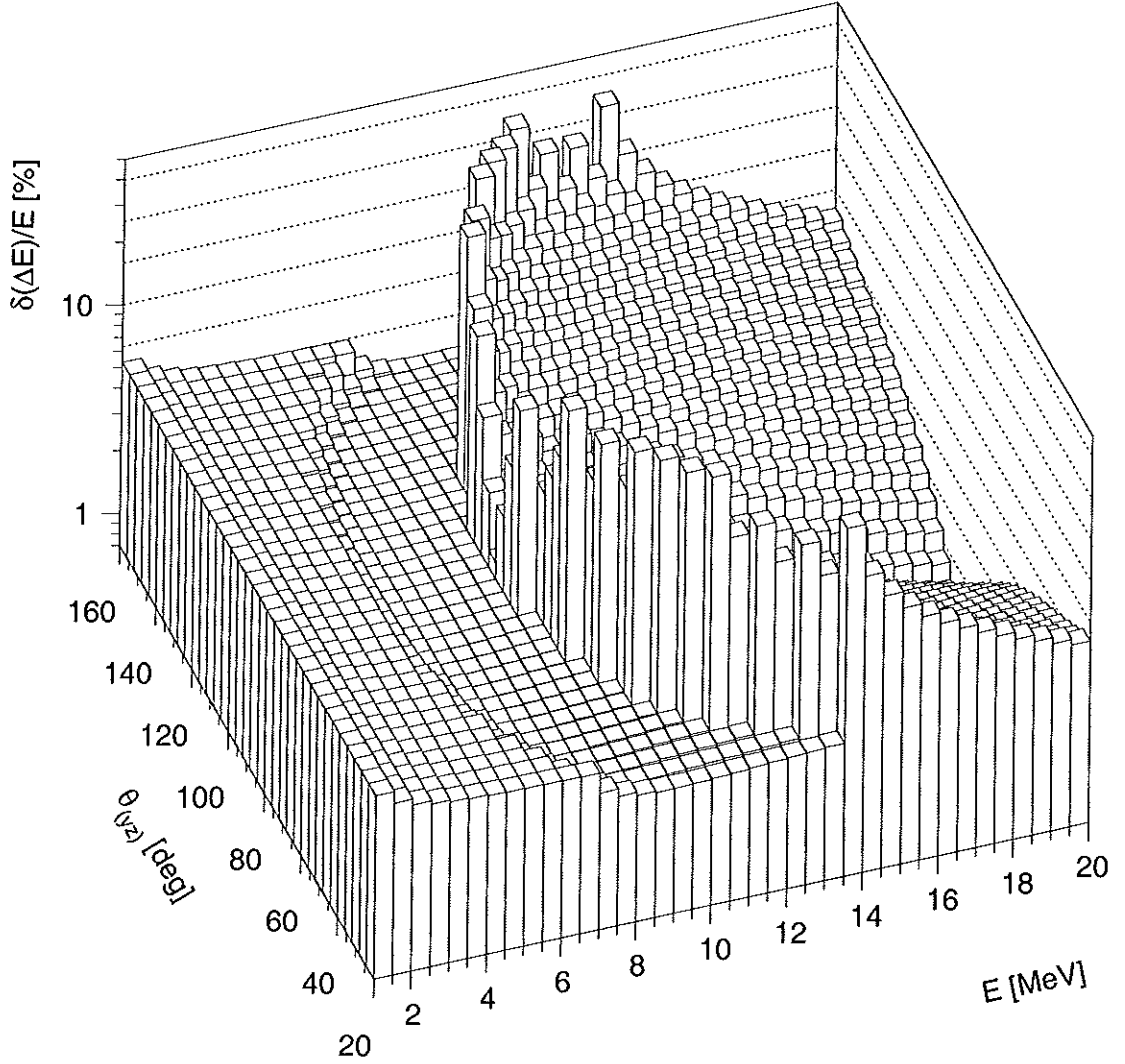


**Figure 4.16:** Total STC energy loss resolution $\delta(\Delta E)_{tot}/E$ in dependence on $E$ and $\theta_{(yz)}$. For reasons of graphical representation, the azimuthal angle is fixed to $\phi = 270°$.

For the third possibility of a particle traversing both the top and the bottom layer, all factors mentioned above have to be taken into account, and the total width of the energy

deposition sum is given by

$$\delta(\Delta E)_{tot} = (\sigma^2_{uncorr,top} + \sigma^2_{calib_{top}} + \sigma^2_{uncorr,bot} + \sigma^2_{calib_{bot}} + \delta(\Delta E)^2_{fit}$$
$$+ \sigma^2_{S,top+bot} + (\delta\Delta E)^2_{t,top+bot} + (\delta\Delta E)^2_{angle,top+bot})^{\frac{1}{2}} .$$

Hereby, the index *top,bot* indicates that the two layers are treated as one Silicon layer with an effective thickness of $t_{eff} = t_{top} + t_{bot}$. This compound approach is justified by the neglectable influence of angular straggling and energy loss of a particle in the area between the two STC modules.

The total STC energy resolution $\delta(\Delta E)_{tot}/E$ derived from the above equations is displayed in figure 4.16 in dependence on the initial energy $E$ and the polar angle $\theta$. It can be concluded that the combination of the angular resolution and the energy straggling results in a total resolution which is best for the case of double hits with an absorption in the bottom layer. Also, the effect of the increased energy loss and straggling close to the punch–through points is clearly visible.

It is noted that the above uncertainties refer to the energy resolution of the STC for a particle of given initial energy and angle. To achieve the uncertainty on the reconstructed energy (see section 4.3.5), the smearing induced by the HERMES storage cell has to be taken into account for all signal combinations. Furthermore, the uncertainty in the angle reconstruction for particles being stopped in the bottom module clearly complicates the particle identification. For the HERMES Recoil Detector with a fully operational vertex reconstruction, the achievable resolution will of course be decisively better.

## 4.3.4  Comparison to Monte Carlo Simulations

The STC Monte Carlo simulations presented in section 3.3 are based on a fully operational detector and furthermore do not include all relevant experimental uncertainties. Therefore, the following extensions are added to the Monte Carlo data:

- The detector output is restricted to the operational APCs, i.e. only the information corresponding to $x_{top,bot}$ and $z_{top}$ is used,

- A Gaussian smearing corresponding to the noise and the calibration uncertainty is applied to the energy deposition,

- The employed HERMES $z$–vertex is smeared with the reconstruction uncertainty.

To allow for possible errors introduced by the STC analysis algorithms, the Monte Carlo data are processed by the same routines used for the STC detector observables. A comparison of the results obtained for deep–inelastic scattering off $^1H$ and $^2H$ is presented in this section.

## Efficiency

Due to the lack of additional experimental observables in the acceptance of the STC, a direct determination of the detector efficiency is not possible. However, using a comparison of the number of reconstructed events for the Monte Carlo and the experimental data, some basic conclusions regarding the detector performance can be drawn.

| target | $^2$H (unpol.) | $^1$H (unpol.) | $^2$H (pol.) |
|---|---|---|---|
| DIS events | 556520 | 241729 | 179427 |
| double hits (data) | 1219 | 265 | 319 |
| double hits (MC) | 922 | 137 | 292 |
| single hits (data) | 315 | 32 | 136 |
| single hits (MC) | 459 | 14 | 134 |

Table 4.5: Comparison of the STC event statistics to the Monte Carlo predictions. The single hit statistics are given for the standard top module threshold of $\Delta E_{thr} = 0.8$ MeV. The uncertainty of the quoted absolute numbers is given by $\pm\sqrt{N}$.

The measurements with the STC were performed using $^1$H and $^2$H targets. However, the noise analysis in section 4.3.3 indicates a difference in the baseline width for polarized and unpolarized $^2$H running and therefore suggests a separate treatment of the two corresponding data samples.

The event statistics shown in table 4.5 give the number of single and double hits for each of the target types as extracted from the experimental and the Monte Carlo data. The latter sample is normalized to the number of DIS events given in table 4.1 and includes the DIS fragmentation process for $^1$H as well as the spectator process for $^2$H. Unless stated otherwise, all results are based on the standard energy deposition thresholds and additional (D and V) cuts for the double hits and an A cut for the single hits.

Regarding the double hit event statistics corresponding to the $^1$H target, it can be observed that the Monte Carlo generator clearly underestimates the number of fragmentation particles detected in the STC, as the experimental result is about a factor of two higher than the Monte Carlo prediction. This deviation is not surprising, as the fragmentation functions employed in the Monte Carlo generator show a high uncertainty for the low energy range corresponding to above–threshold energy depositions in the STC.

In the kinematic range determined by the employed cuts (see section 4.2.3), a spectator proton occurs in about 44 % of the events in scattering off $^2$H. The assumption of comparable fragmentation functions for scattering off protons and neutrons allows to extract the number of detected spectator protons by a normalized subtraction of the $^1$H and the $^2$H data. The result shows an excellent agreement on the $1\sigma$ level of $\sqrt{N}$ between the experimentally observed number and the Monte Carlo prediction, as illustrated by the unpolarized $^2$H double hit ratio of $N_{exp} = 609$ to $N_{MC} = 607$ spectator protons.

When regarding the single hit event statistics, it is observed that the experimental values are significantly lower than expected from the Monte Carlo calculations. Since the deviation is much more pronounced for the data taken with unpolarized targets, the effect could be associated with an increase in Møller electron background, which causes additional signals in the bottom STC module and therefore leads to the misinterpretation of a single hit as a double hit. While these events are removed by the correlation cuts applied to double hits, they no longer contribute to the single hit event sample.

Another source of uncertainty to be taken into account for single hits is the low resolution of the reconstructed HERMES $z$–vertex, which complicates the selection of particles in the double hit acceptance being stopped in the top layer. Thus, unless stated otherwise, the following results will be based on the STC double hit event sample. As an aside, it is remarked that both the low vertex resolution and the restricted bottom layer acceptance are specific to the STC and will not be present in the full HERMES Recoil Detector.

## Energy Deposition Correlation

As outlined in section 4.3.2, the energy deposition correlation between the top and the bottom STC module allows to identify the detected particle type, which for the considered physics processes corresponds to mainly protons. Due to the absence of spectator protons in scattering off $^1H$, a comparison of the STC response for the 1H and $^2H$ data samples is therefore expected to reveal a considerable decrease in the number of detected protons for the former target type.

In figure 4.17, the energy deposition correlation plots are shown for scattering off both $^1H$ and $^2H$. The two top graphs are based on measured STC response with unpolarized targets, while the two bottom graphs result from a Monte Carlo simulation normalized to the number of detected DIS events. Firstly, it can be observed that the proton–induced triangular shape of the correlation is only present in the plots based on $^2H$, while for $^1H$, only part of the punch–through branch corresponding to higher proton energies is visible. Furthermore, a good agreement of the experimental data with the Monte Carlo simulations is present. These results clearly indicate the existence and the dominance of the spectator process in scattering off $^2H$, while the particles observed in the $^1H$ data sample are based on fragmentation. To allow a further confirmation, the angular and momentum spectra of the two processes will be investigated in the following[10].

## Angular Distribution

As outlined in section 4.3.2, the knowledge of the incidence angle $\alpha$ is crucial for the particle identification as well as the momentum reconstruction. Using equation 2.1, it can be derived that, due to the limited STC $\phi$–acceptance, the incidence angle is mainly

---

[10]As the major part of the STC data corresponds to measurements with unpolarized targets, the following results can be restricted to this subset without compromising the significance.
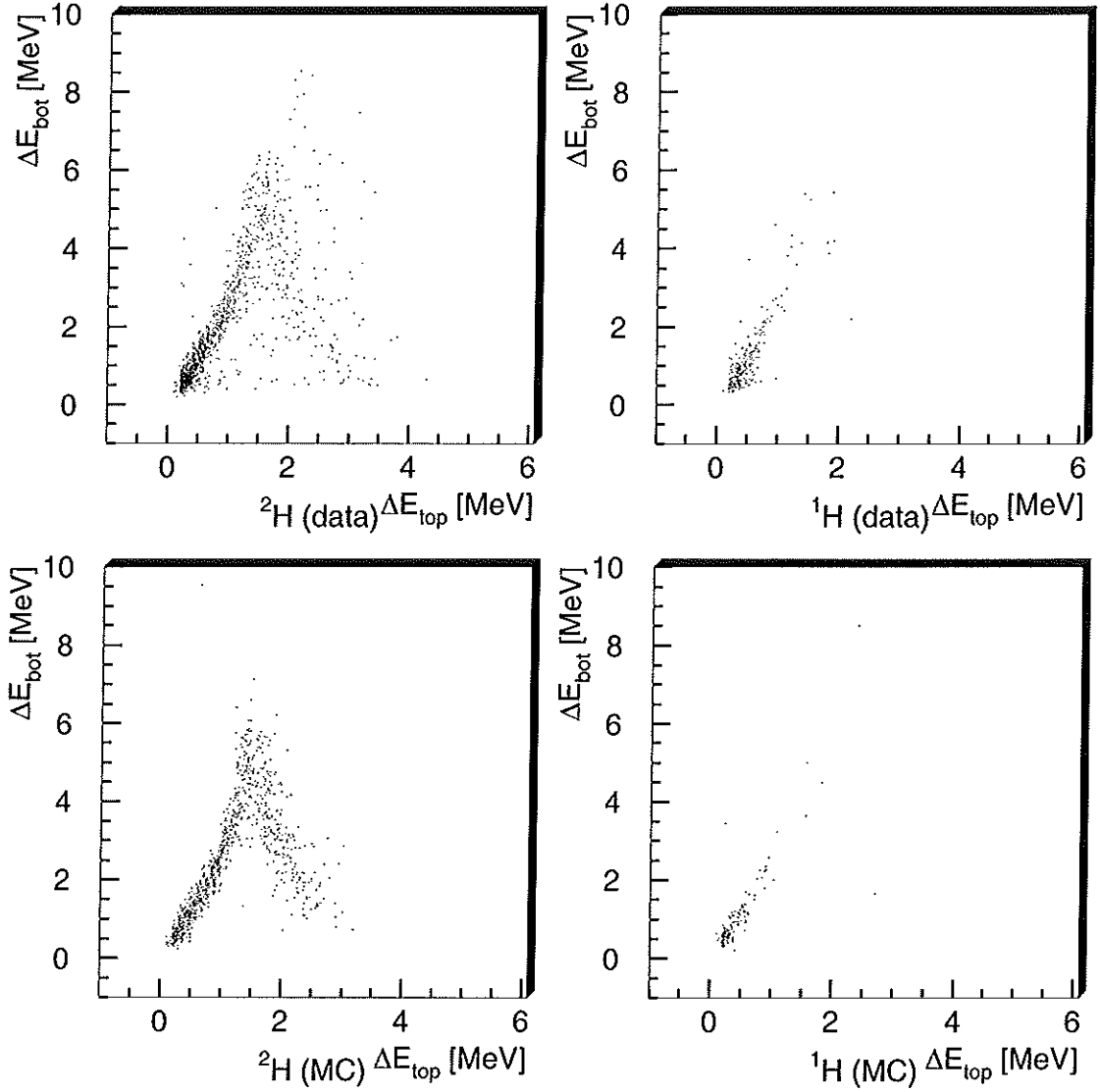
Figure 4.17: Comparison of the measured STC energy deposition correlation (data) for the unpolarized $^1H$ and $^2H$ data samples with the results of Monte Carlo simulations (MC). The number of generated Monte Carlo events is equal to the number of DIS events in the STC data samples.

determined by the polar angle $\theta$. With all relevant experimental uncertainties included in the Monte Carlo simulations, it is possible to compare the angular spectra measured with the STC to the theoretical predictions based on the generation of spectator protons and fragmentation products.
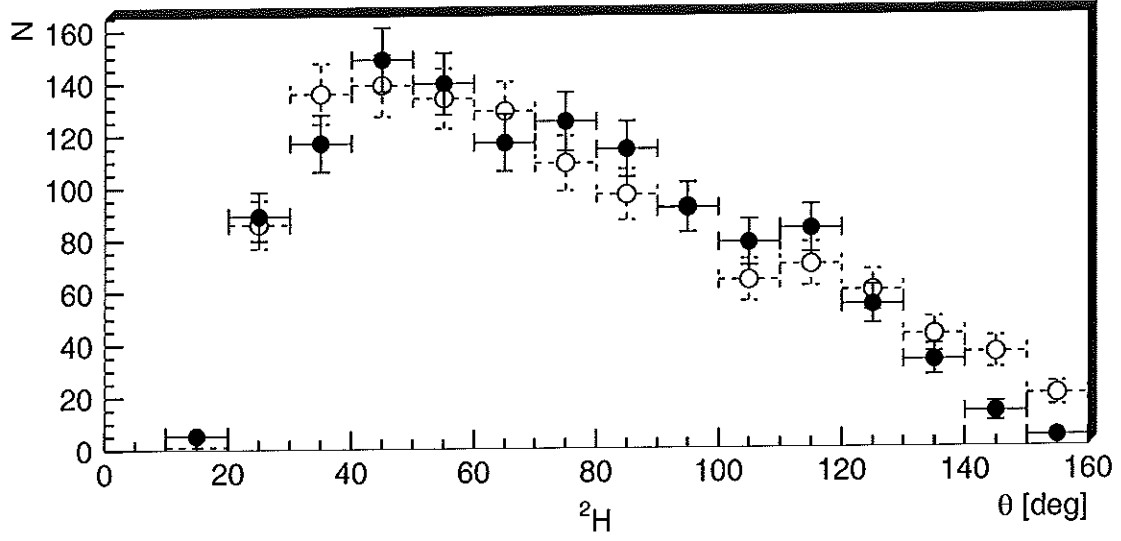
Figure 4.18: Comparison of the measured STC $\theta$-distribution for a $^2H$ target (full circles) with the result of a Monte Carlo simulation (empty circles). The vertical error bars show the statistical uncertainty.
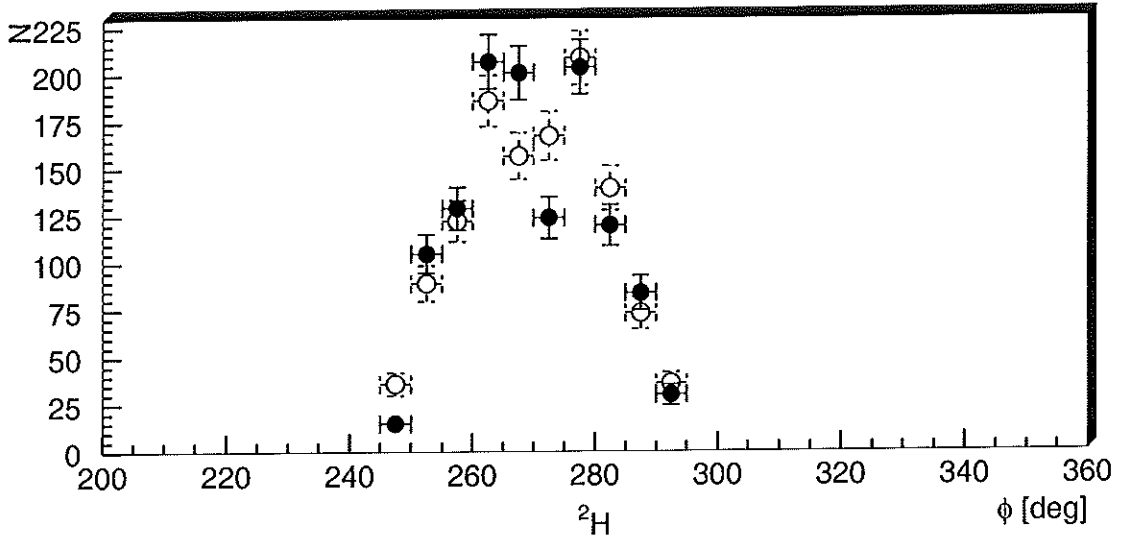


Figure 4.19: Comparison of the measured STC $\phi$-distribution for a $^2H$ target (full circles) with the result of a Monte Carlo simulation (empty circles). The vertical error bars show the statistical uncertainty.

The $\theta$-distribution measured with the STC for a $^2H$ target is shown in figure 4.18, together with the equivalent spectrum extracted from a Monte Carlo simulation. Both

spectra are in reasonable agreement over the full STC acceptance range, even though the above discussion on the event statistics indicates that the impact of the fragmentation products on the STC response is underestimated in the employed Monte Carlo generator. The shift to small polar angles in the measured distribution as compared to the generated $\theta$-spectrum (see figure 2.5) is a result of the forward–facing acceptance of the operational STC modules.

As neither the spectator protons nor the fragmentation products show a dependence on the azimuthal angle $\phi$, the corresponding distribution in the STC is expected only to mirror the detector acceptance. This behaviour is confirmed by the spectra given in figure 4.19, which show no significant difference between the measured angular distributions and the Monte Carlo prediction.
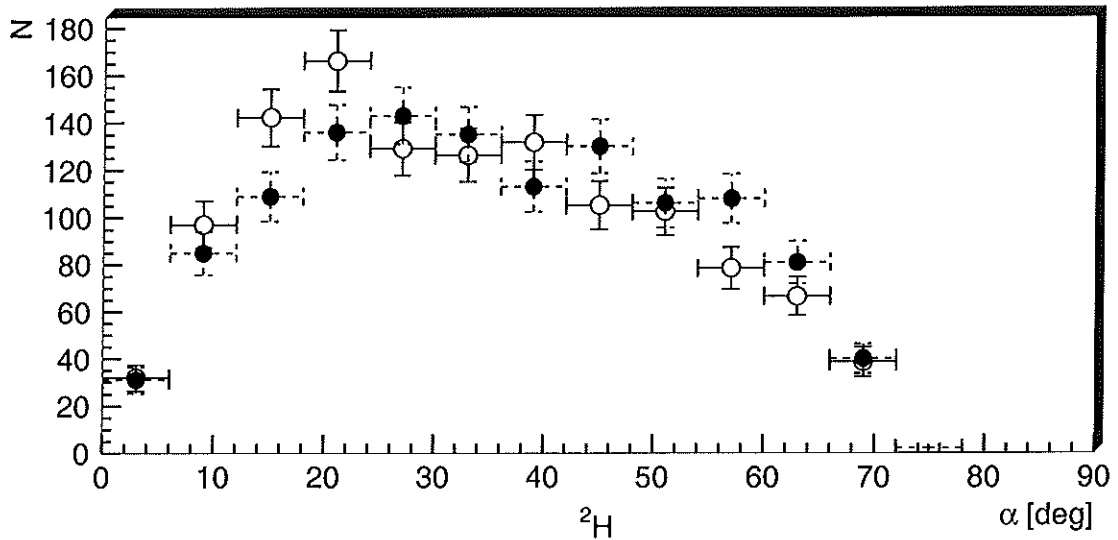


Figure 4.20: Comparison of the measured STC $\alpha$–distribution for a $^2$H target (full circles) with the result of a Monte Carlo simulation (empty circles). The vertical error bars show the statistical uncertainty.

With the knowledge of $\theta$ and $\phi$ for an event in the STC, the incidence angle $\alpha$ needed for the energy deposition correction can be determined. Figure 4.20 again displays the comparison of the measured spectrum with the distribution derived from Monte Carlo results. Again, a satisfactory agreement can be observed in the angular range of the STC acceptance. It is noted that the folding of the $\theta$- and $\phi$-spectra does not lead to a maximum in the range of $\alpha = 0°$, as it could be naively expected.

The distributions presented so far include a mixture of events resulting from spectator protons as well as fragmentation products. As the forward–facing acceptance of the operational STC modules does not allow to impose a cut in $\theta$ without severely restricting the statistical accuracy, an alternative method of separating the two contributions has to

be applied.
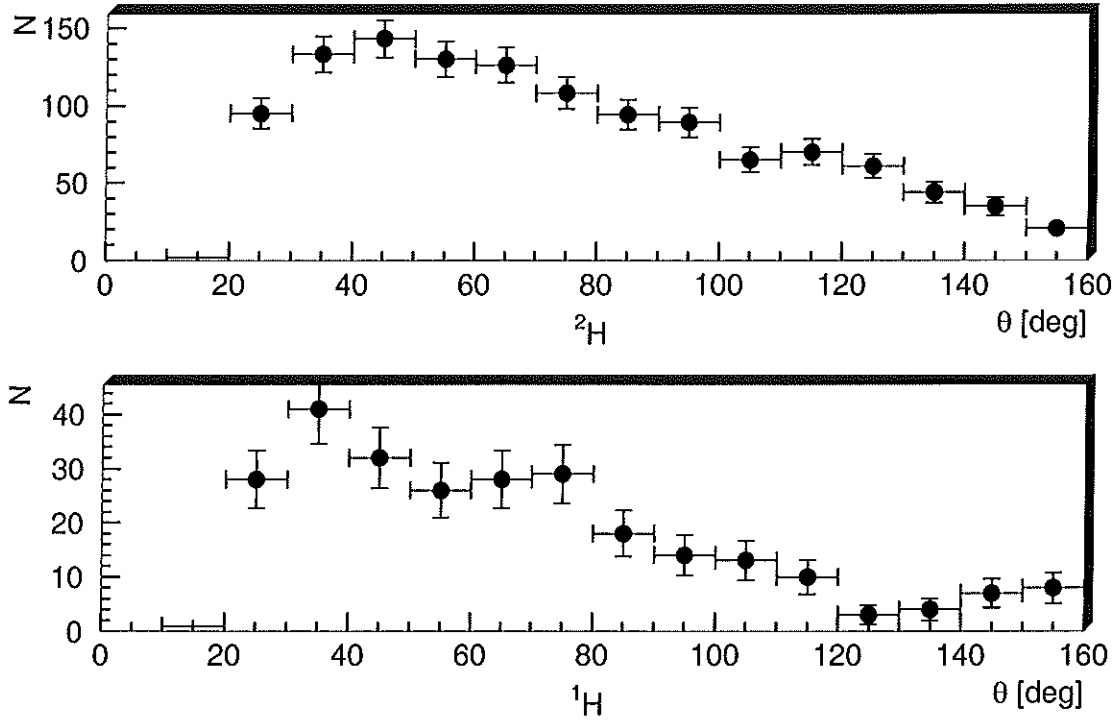


Figure 4.21: Comparison of the unnormalized measured STC $\theta$–distributions for a $^2H$ and a $^1H$ target. The vertical error bars show the statistical uncertainty.

Under the assumption of comparable DIS fragmentation products for a proton and a neutron, the events detected in the STC for scattering off $^1H$ correspond to the pure fragmentation contribution to the $^2H$ measurements. After a normalization to the number of DIS events in the $^2H$ sample, a subtraction of the $^1H$ data from the $^2H$ data should therefore give access to the pure spectator proton distributions. An exact normalization, however, further has to take into account the different quark content and the resulting fragmentation products in the proton and the neutron. Based on Monte Carlo data, this fragmentation correction factor was determined to $f = 1.17$.

This method is illustrated by means of figure 4.21, which compares the $\theta$–distributions measured in the STC for scattering off $^1H$ and $^2H$. In spite of the low number of events in the $^1H$ sample, it can be observed that the fragmentation particles mainly occur under small polar angles. Using the correct normalization factor of $n = 2.69$ derived from the event statistics given in table 4.5 and the fragmentation correction factor, $n$ times the $^1H$ spectrum can now be subtracted from the $^2H$ spectrum. The resulting distribution is shown in figure 4.22 in comparison to the simulated STC response to pure spectator protons.
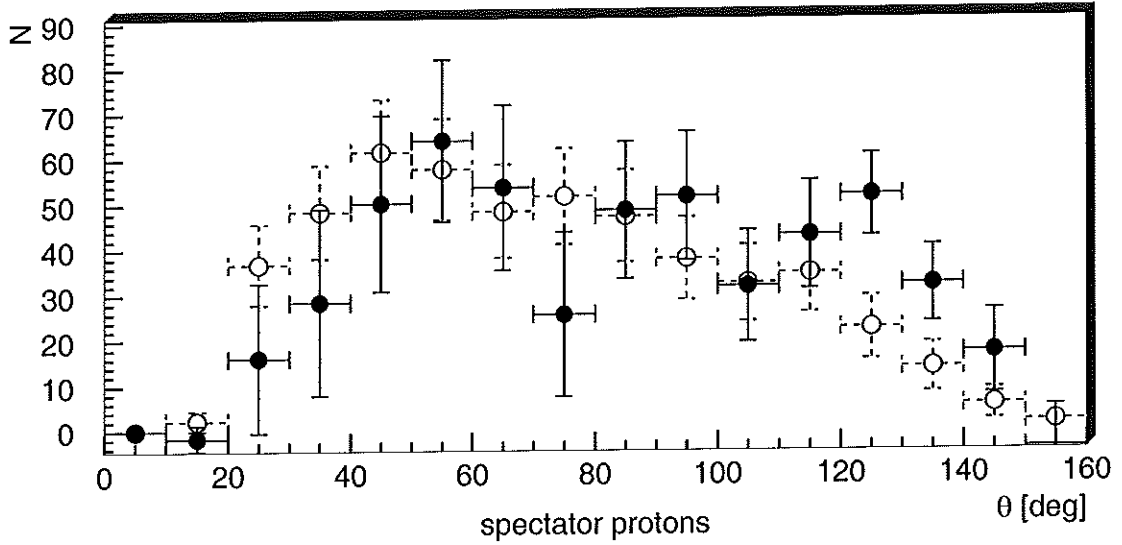
Figure 4.22: Comparison of the extracted STC $\theta$-distribution for pure spectator protons (full circles) with the Monte Carlo prediction (empty circles). The vertical error bars show the statistical uncertainty.

Given the low number of events in the measured spectrum, no significant deviation from the theoretical prediction is observed within the achievable accuracy. However, the backward–scattering $\theta$-range of $\theta > 90°$ seems to be more pronounced in the experimental data than expected from the Monte Carlo simulations, which could be explained by a difference in the proton and neutron fragmentation products in the low–energy domain. The lack of an operational backward–facing module combination in the STC, together with the low angular resolution imposed by the dependence on the HERMES $z$–vertex, does not allow a further separation of the underlying physics processes. The distinct improvement in acceptance and resolution given with the HERMES Recoil Detector would naturally facilitate this task.

## 4.3.5 Momentum Reconstruction

### Reconstruction Algorithm

The physics objective of the STC data analysis is the determination of the particle types and initial momenta from the experimental observables $\Delta E_{top}$, $\Delta E_{bot}$ and the incident angle $\alpha$. In accordance with the correlation plot shown in figure 2.3, three separate hit conditions have to be considered.

The sequence of the momentum reconstruction algorithm can be illustrated by means of the chart shown in figure 4.23. As only events with a signal in the top counter are

considered, the first discrimination is between single hits ($\Delta E_{bot} = 0$) and double hits



$\Delta E_{top} > 0$

$\Delta E_{bot} > 0$

yes        no

particle stopped in
bottom module

track in bottom
module acceptance

no        yes        yes        no

$E(\Delta E_{top} + \Delta E_{bot})$    $E = \Delta E_{top} + \Delta E_{bot}$    $E = \Delta E_{top}$    discard
event

correct for cell wall
thickness and $\alpha$

$E_{initial}$
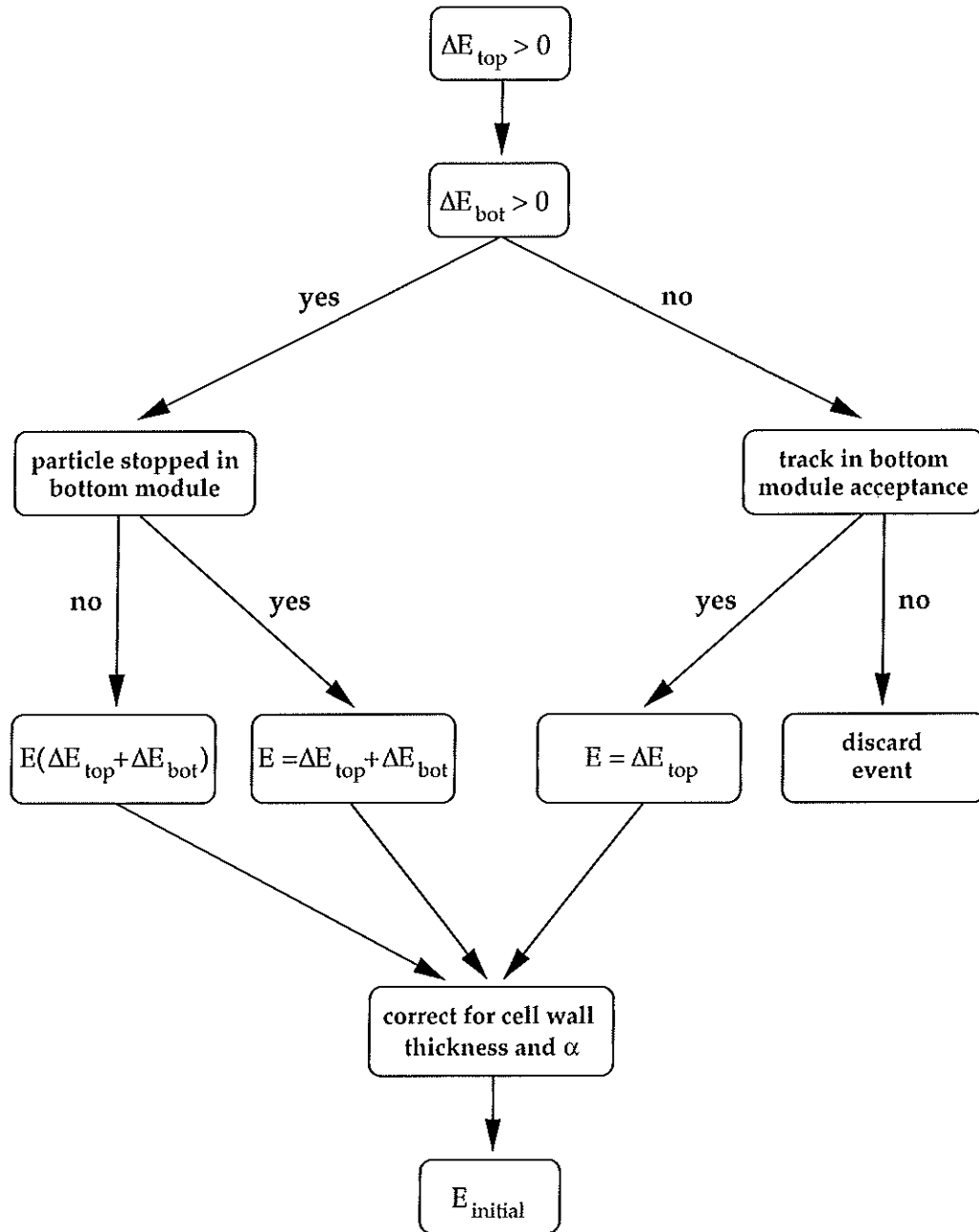
Figure 4.23: Schematic sequence of the momentum reconstruction algorithm.

($\Delta E_{bot} > 0$). In the former case, the particle can either pass the top and miss the bottom layer, or it can be stuck in the top layer. Using the tracking information, all events which are not in the geometric acceptance of the bottom layer are discarded. For the remaining sample, the particle energy $E$ before hitting the counter is given by $E = \Delta E_{top}$.

In the case of double hits, the event sample is divided into particles stuck in and particles passing the bottom layer by means of the energy deposition correlation. In the former case, the particle energy $E$ is again given by the total energy deposition, i.e. $E = \Delta E_{top} + \Delta E_{bot}$, while for the remaining sample $E$ has to be determined using the iterative inversion of equation 4.3. With the knowledge of the incident angle $\alpha$, the employed detector thickness $t_{tot}$ is given by

$$t_{tot} = \frac{t_{top} + t_{bot}}{\cos \alpha} \; .$$

Finally, the resulting particle energies $E$ have to be corrected for the energy loss in the HERMES storage cell wall to obtain the initial energies $E_{ini}$ at the interaction point. This is achieved analytically using the equation

$$E_{initial} = \left( E^b + \frac{t_{wall} \cdot \rho_{Al}}{\cos \alpha \cdot a} \right)^{1/b} ,$$

with $t_{wall}$ being the storage cell wall thickness, $\rho_{Al}$ the density of Aluminum and $a, b$ the parameterization constants for the energy loss in Aluminum[11]. As the observed particle type is known from the energy deposition correlation, a conversion of $E_{initial}$ to the initial momentum $p_{initial}$ is straightforward.

## Acceptance Corrections

In order to verify the reliability of the employed reconstruction algorithm, the Monte Carlo simulation of the STC response to pure spectator protons can be used as a test input. The result is shown in figure 4.24 in comparison to the theoretical momentum density distribution utilized in the Monte Carlo generator. While a good agreement is achieved over a wide range of momenta, the reconstruction clearly deviates for the high– and the low–momentum end of the spectrum. The reason for this behaviour is easily understood when the energy deposition thresholds applied in the STC data analysis and the influence of the HERMES storage cell are taken into account.

As figure 4.20 shows, the incidence angles observed in the STC are distributed over a wide range. A low–momentum spectator proton reaching the HERMES storage cell wall has to traverse an effective wall thickness scaling with $1/\cos \alpha$ to be detected in the STC. Therefore, a particle of fixed initial energy hitting the cell wall under $\alpha = 0°$ may pass

---

[11]As the difference in the density–weighted mass stopping power $dE/\rho \cdot dx$ for Si and Al is less than 3 % in the relevant energy range, the same constants $a, b$ can be used.
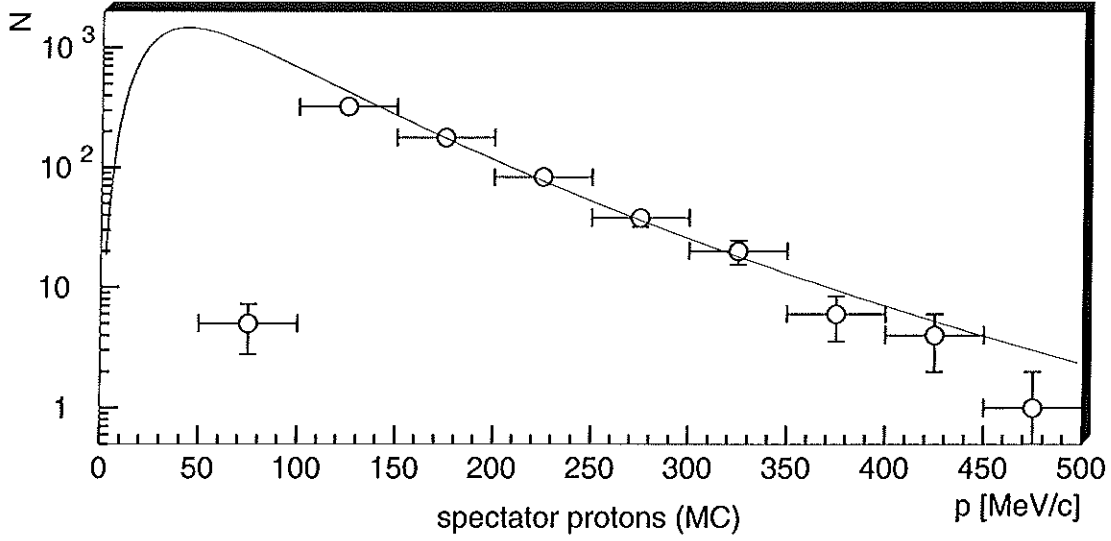
**Figure 4.24:** Momentum reconstruction of Monte Carlo generated spectator protons for double hits in the STC (data points) in comparison to the theoretical momentum density distribution (solid line). The error bars on the data points indicate the statistical uncertainty.

the wall as well as the top STC module, while under a higher incidence angle, it may be stopped in the cell wall or the top Silicon layer. This results in an underestimation of the momentum density for low spectator proton momenta.

In the high–momentum end of the spectrum, the opposite effect is observed. Given the energy deposition thresholds applied to the STC modules, a particle of fixed initial energy traversing the Silicon layers under a high incidence angle may deposit an above–threshold energy, while under $\alpha = 0°$, the corresponding event is removed by the threshold cut. Therefore, the reconstructed momentum density is too low for high spectator proton momenta.

To illustrate the influence of the incidence angle on the number of reconstructed events in a certain momentum range, figure 4.25 displays the corresponding correlation as extracted from the unpolarized $^2H$ data sample of the STC. The low–momentum bin is clearly dominated by low incidence angles, while momenta higher than $\approx 350$ MeV/c correspond to higher values of $\alpha$.

Under the assumption of a momentum–independent angular distribution, a correction factor for a given particle momentum can be determined. While this procedure finds only restricted application in the analysis of the STC data, the basic steps are outlined in the following.

Given the geometric setup of a Silicon telescope and the corresponding stopping power parameterizations, an value $\alpha_{max}$ can be derived which denotes the maximum incidence
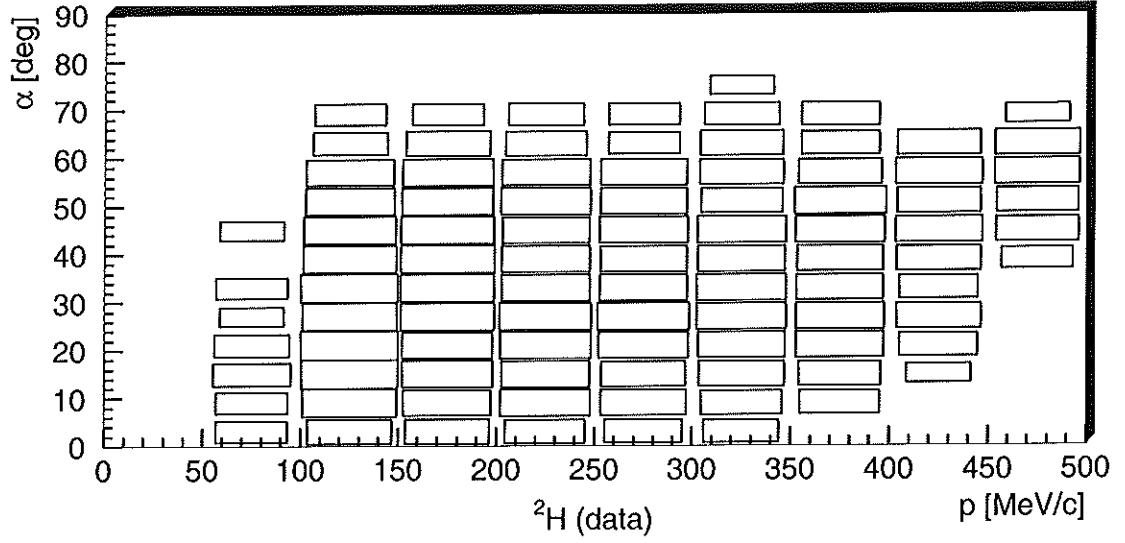
Figure 4.25: Correlation of the reconstructed incidence angles $\alpha$ and the reconstructed momenta $p$ for double hits in the unpolarized STC $^2$H data sample.

angle under which a punch–through can occur for a given particle. With $f(\alpha)$ being the angular distribution in the detector acceptance, the normalization factor $n(E)$ for a given energy $E$ is

$$n(E) = \frac{\int_0^{\alpha_{max}} f(\alpha)\,d\alpha}{\int_0^{\pi/2} f(\alpha)\,d\alpha}\,,$$

i.e. the accessible fraction of the total angular spectrum. For the case of a threshold cut, $\alpha_{min}$ can be defined accordingly, with a resulting normalization factor

$$n(E) = \frac{\int_{\alpha_{min}}^{\pi/2} f(\alpha)\,d\alpha}{\int_0^{\pi/2} f(\alpha)\,d\alpha}\,.$$

Due to the statistical limitations in the STC data sample, the analysis of the momentum distribution is restricted to the kinematical region of 100 MeV/c $< p <$ 350 MeV/c, in which only minor corrections to the low– and high–momentum bin are necessary. The determination of the correction factors is performed by means of Monte Carlo simulations.

## Single Hits

As discussed in section 4.3.1, the accessible momentum distribution can be extended in the low–momentum region by the inclusion of single hits in the analysis. The signature for this class of events is an above–threshold energy deposition in only the top STC module and a reconstructed particle vertex inside the double hit acceptance.

However, the analysability of the STC single hit data is restricted by several factors. Firstly, an additional systematic error is introduced by the large uncertainty in the HER-MES $z$–vertex needed for the application of the acceptance cut. Here, a certain fraction of the events will be wrongly considered as inside resp. outside the double hit acceptance. Using Monte Carlo techniques, the uncertainty on the total number of reconstructed single hits can be estimated to $\delta N/N \approx 17\ \%$.

When further taking into account the deviation from the Monte Carlo prediction in the single hit event sample (see section 4.3.4), an inclusion of the single hit events in the determination of the spectator momentum distribution seems inadvisable. It is noted that this omission is based on the small active area of the STC modules together with the missing $z$–vertex reconstruction, which will both not be present in the HERMES Recoil detector.

## Resolution of the Reconstructed Energy

In section 4.3.3, the energy deposition resolution $\delta(\Delta E)_{tot}$ in the STC has been presented in detail. However, to obtain the uncertainty in the *reconstructed* energy $\delta E_{ini}$ at the interaction point, the deposition error has to be propagated through the inversion of equation 4.3 using numerical methods. Furthermore, the uncertainty introduced by the energy loss and smearing introduced by the HERMES storage cell wall has to be taken into account. This can be achieved using the same approach as described in section 4.3.3, whereby the parameters corresponding to 75 $\mu$m of Aluminum are employed. In summary, the following steps are performed on an event–by–event basis:

1. The total energy deposition resolution $\delta(\Delta E)_{tot}$ is determined.

2. The corresponding uncertainty in the particle energy is calculated for the case of double hit punch–through events.

3. The error on the initial energy $\delta(E_{ini})_{dep}$ at the interaction point induced by $\delta(\Delta E)_{tot}$ is specified.

4. The contributions from energy straggling and the angular resolution are determined and added in quadrature to $\delta(E_{ini})_{dep}$.

## Spectator Momentum Distribution

Taking into account the above considerations, the momentum density distribution of the observed spectator protons in scattering off $^2H$ can be extracted. As described in section 4.3.4, the normalized spectrum obtained from the $^1H$ data sample is subtracted from the deuteron data to allow for the dilution by fragmentation products. The result based on double hits in the STC is shown in figure 4.26 in comparison to a parameterization of the deuteron momentum density $|\psi(|p_s|)|^2 \cdot p_s^2$ [Kra:76]. The displayed uncertainty in the
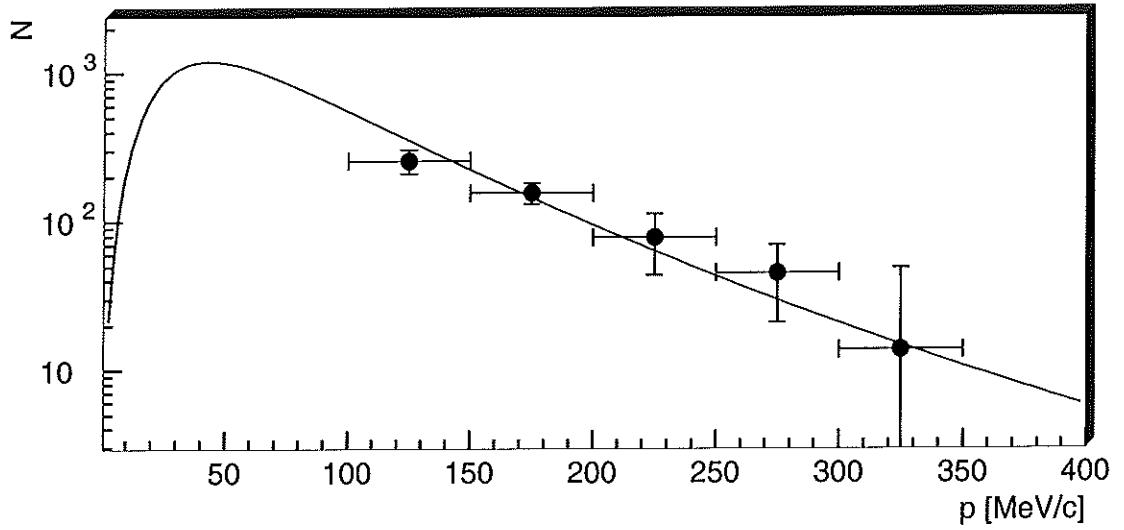
Figure 4.26: Distribution of the reconstructed spectator momenta $p$ for double hits in the unpolar-
ized STC $^2$H data sample. The solid line represents a parameterization of the deuteron
momentum density $|\psi(|p_s|)|^2 \cdot p_s^2$ [Kra:76].

number of counts is derived from the shift in a momentum bin after an error of $\pm\sigma$ is
applied to the reconstructed energy.

Despite the various uncertainties complicating the analysis of the STC data, a satisfac-
tory agreement of the measurement with the theoretical prediction can be observed. Given
the fact that the restricting factors in resolution and acceptance are exclusively based on
the limited performance of the STC, it can be concluded that the feasibility of operating a
Silicon telescope in the HERMES vacuum environment has clearly been proven.

# Summary

The HERMES experiment at the DESY research centre uses a 27.5 GeV electron beam to investigate the spin structure of the nucleon by means of polarized deep–inelastic scattering off an internal gas target. While the acceptance of the employed spectrometer is optimized for the detection of forward–scattered particles in the final state, the physics potential can be significantly expanded by the observation of particles at higher angles. This thesis presents a project to implement an additional detector at HERMES to serve this purpose.

In the first part, the benefit of extending the acceptance in the target region is motivated for several physics cases like diffractive scattering, off–forward parton distributions and nuclear corrections. Based on the resulting detector requirements and the restrictions imposed by the HERMES environment, a design for a suitable Silicon telescope is presented. Given the unique conditions at HERMES , this HERMES *Recoil Detector* can be positioned inside the target vacuum vessel and in close proximity to the electron beam. The expected detector response and the background conditions are determined by means of detailed Monte Carlo simulations.

To prove the feasibility of operating a recoil detector in the specified environment, a test device with reduced acceptance has been designed and installed for the 1998 HERMES data taking period. The second part of this thesis describes the design and the expected performance of this *Silicon Test Counter*. Afterwards, the integration of the device into the HERMES data production and the analysis routines developed to extract the physics observables are presented.

The experience with operating the Silicon Test Counter and the first results obtained with scattering off $^1$H and $^2$H are summarized in the final chapter. In spite of a clear restriction in the counters functionality, the occurrence of spectator protons is verified, and the observed momentum distribution is in agreement with theoretical predictions. In conclusion, the operability of a full–scale recoil detector at HERMES has been proven.

# Zusammenfassung

Das HERMES – Experiment am Forschungszentrum DESY benutzt einen Elektronenstrahl von 27,5 GeV zur Untersuchung der Spinstruktur des Nukleons durch tiefinelastische Streuung an einem internen Gastarget. Während die Akzeptanz des eingesetzten Spektrometers auf den Nachweis von vorwärtsgerichteten Streuprodukten optimiert ist, kann das physikalische Potential durch die Beobachtung von Teilchen unter höheren Winkeln deutlich erweitert werden. Die vorliegende Arbeit präsentiert ein Projekt zur Implementierung eines zusätzlichen, diesem Zweck dienenden Detektors in das HERMES – Experiment.

Im ersten Teil der Arbeit werden die Vorteile einer Erweiterung der Akzeptanz im Bereich des Targets anhand einiger physikalischer Fragestellungen wie diffraktive Streuung, verallgemeinerte Partonverteilungen und nukleare Korrekturen erläutert. Unter Berücksichtigung der sich ergebenden Anforderungen und der Einschränkungen aufgrund der experimentellen Rahmenbedingungen wird der Entwurf eines geeigneten Siliziumteleskops präsentiert. Aufgrund der einzigartigen Bedingungen bei HERMES kann dieser HERMES *Recoil Detector* innerhalb des Targetvakuums in direkter Nähe zum Elektronenstrahl installiert werden. Das erwartete Verhalten des Detektors und die Untergrundverhältnisse werden durch eingehende Monte–Carlo–Simulationen bestimmt.

Zur Überprüfung der Durchführbarkeit eines Detektorbetriebs unter den gegebenen Rahmenbedingungen wurde ein Testdetektor mit reduzierter Akzeptanz entworfen und 1998 zu Beginn der HERMES – Datennahme installiert. Der zweite Teil der vorliegenden Arbeit beschreibt den Aufbau und das erwartete Verhalten dieses *Silicon Test Counters*. Anschließend werden die Integration des Detektors in die HERMES – Datenproduktion und die zur Extraktion der physikalischen Observablen entwickelten Analyseroutinen erläutert.

Die Erfahrungen mit dem Betrieb des Silicon Test Counters und die ersten gewonnenen Ergebnisse aus der Streuung an $^1$H und $^2$H werden im Abschlußkapitel zusammengefaßt. Trotz der deutlich eingeschränkten Funktionalität des Detektors konnte das Auftreten von Zuschauernukleonen bestätigt werden, wobei die gemessene Impulsverteilung im Einklang mit der theoretischen Vorhersage ist. Die Möglichkeit des Betriebs eines Rückstoßdetektors mit voller Akzeptanz im HERMES – Experiment ist dadurch bewiesen worden.

# List of Figures

# List of Tables

# Bibliography

[B+:81]    A. Bussiere et al., *Momentum distribution of nucleons in the deuteron from the d(e, e'p)n reaction*, Nucl. Phys. **A365**, 349 (1981).

[B+:94]    R. Brun et al., *GEANT detector description and simulation tool (long writeup W5013)*, CERN-CN Application Software Group, Geneva, 1994.

[B+:95]    D. P. Barber et al., *The first achievement of longitudinal spin polarization in a high-energy electron storage ring*, Phys. Lett. **B343**, 436 (1995).

[B+:97]    E. Bronchalo et al., *Parametrization of charge and mass resolution for $\Delta E$–E telescopes*, Nucl. Instr. Meth. **A399**, 65 (1997).

[BBS:95]   S. J. Brodsky, M. Burkardt and I. Schmidt, *Perturbative QCD constraints on the shape of polarized quark and gluon distributions*, Nucl. Phys. **B441**, 197 (1995).

[BJ:81]    E. L. Berger and D. Jones, *Inelastic photoproduction of J/Psi and Y by gluons*, Phys. Rev. **D23**, 1521 (1981).

[Bjø:69]   J. D. Bjørken, *Asymptotic sum rules at infinite momentum*, Phys. Rev. **179**, 1547 (1969).

[BL:82]    J. Bartels and M. Loewe, *The nonforward QCD ladder diagrams*, Zeit. Phys. **C12**, 263 (1982).

[Boh:15]   N. Bohr, Philos. Mag. **30**, 581 (1915).

[BP:69]    J. D. Bjørken and E. A. Paschos, *Inelastic electron–proton and $\gamma$–proton scattering and the structure of the nucleon*, Phys. Rev. **185**, 1975 (1969).

[BR:81a]   A. Bodek and J. Ritchie, *Fermi–motion effects in deep–inelastic scattering from nuclear targets*, Phys. Rev. **D23**, 1070 (1981).

[BR:81b]   A. Bodek and J. Ritchie, *Further studies of Fermi–motion effects in lepton scattering from nuclear targets*, Phys. Rev. **D24**, 1400 (1981).

[BT:67]      H. Bichsel and C. Tschalaer, *A range–energy table for heavy particles in Silicon*, Nuclear Data **A3**, 343 (1967).

[Car:75]     R. Carlitz, *SU(6) symmetry breaking effects in deep inelastic scattering*, Phys. Lett. **B58**, 345 (1975).

[CFS:97]     J. C. Collins, L. Frankfurt and M. Strikman, *Factorization for hard exclusive electroproduction of mesons in QCD*, Phys. Rev. **D56**, 2982 (1997).

[CLS:91]     C. E. Carlson, K. E. Lassila and U. P. Sukhatme, *Backward hadrons from deep inelastic lepton scattering on nuclei*, Phys. Lett. **B263**, 277 (1991).

[Col:97]     J. Collins, *Light-cone variables, rapidity and all that*, hep-ph/9705393, 1997.

[CRR:83]     F. E. Close, R. G. Roberts and G. G. Ross, *The effect of confinement size on nuclear structure functions*, Phys. Lett. **B129**, 346 (1983).

[dAS:95]     C. C. degli Atti and S. Simula, *Nucleon-nucleon correlations and six quark cluster effects in semiinclusive deep inelastic lepton scattering off few nucleon systems*, Few Body Syst. **18**, 555 (1995).

[dJ:97]      X. dong Ji, *Deeply virtual Compton scattering*, Phys. Rev. **D55**, 7114 (1997).

[dJ:98]      X. dong Ji, *Off-forward parton distributions*, J. Phys. **G24**, 1181 (1998).

[Due:95]     M. Dueren, *The HERMES-Experiment: From the design to the first results*, Habilitationsschrift, Universität Erlangen-Nürnberg, 1995.

[EMC:83]     J. Aubert et al. (EMC Collaboration), *The ratio of the nucleon structure functions $F_2(N)$ for Iron and Deuterium*, Phys. Lett. **B123**, 275 (1983).

[EMC:88]     J. Ashman et al. (EMC Collaboration), *A measurement of the spin asymmetry and determination of the structure function $g_1$ in deep inelastic muon-proton scattering*, Phys. Lett. **B 206**, 364 (1988).

[Fey:72]     R. P. Feynman, *Photon-Hadron Interactions*, W. A. Benjamin, New York, 1972.

[For:96]     J. R. Forshaw, *Vector meson summary*, J. Phys. **G22**, 937 (1996).

[FS:81]      L. Frankfurt and M. Strikman, *High-energy phenomena, short range nuclear structure and QCD*, Phys. Rep. **76**, 215 (1981).

[FS:88]      L. L. Frankfurt and M. I. Strikman, *Hard nuclear processes and microscopic nuclear structure*, Phys. Rept. **160**, 235 (1988).

[GLR:83]      L. V. Gribov, E. M. Levin and M. G. Ryskin, *Semihard processes in QCD*, Phys. Rept. **100**, 1 (1983).

[Gui:88]      J.-P. Guillet, *A way to measure the spin dependent distribution of the gluon*, Z. Phys. **C39**, 75 (1988).

[Gut:99]      A. Gute, *Messung der polarisierten Strukturfunktion $g_1^p$ des Protons im HERMES–Experiment*, Dissertation, Universität Erlangen-Nürnberg, 1999.

[HER:90]      *A proposal to measure the spin dependent structure functions of the neutron and the proton at HERA*, HERMES Internal Note 90-002, 1990.

[HER:00]      *The HERMES Physics Program and Plans for 2001-2006*, HERMES Internal Note 00-003, 2000.

[HERMES:97a] K. Ackerstaff et al. (HERMES Collaboration), *Measurement of the neutron spin structure function $g_1^n$ with a polarized He-3 internal target*, Phys. Lett. **B404**, 383 (1997).

[HERMES:97b] G. Steenhoven et al. (HERMES Collaboration), *New silicon-detector systems for the HERMES front region*, HERMES Internal Note 97-032, 1997.

[HERMES:98a] K. Ackerstaff et al. (HERMES Collaboration), *Determination of the deep inelastic contribution to the generalised Gerasimov-Drell-Hearn integral for the proton and neutron*, Phys. Lett. **B444**, 531 (1998).

[HERMES:98b] K. Ackerstaff et al. (HERMES Collaboration), *The flavor asymmetry of the light quark sea from semi-inclusive deep inelastic scattering*, Phys. Rev. Lett. **81**, 5519 (1998).

[HERMES:98c] K. Ackerstaff et al. (HERMES Collaboration), *The HERMES Spectrometer*, Nucl. Instr. Meth. **A417**, 230 (1998).

[HERMES:98d] A. Airapetian et al. (HERMES Collaboration), *Measurement of the proton spin structure function $g_1^p$ with a pure hydrogen target*, Phys. Lett. **B442**, 484 (1998).

[HERMES:99a] K. Ackerstaff et al. (HERMES Collaboration), *Beam-induced nuclear depolarisation in a gaseous polarised hydrogen target*, Phys. Rev. Lett. **82**, 1164 (1999).

[HERMES:99b] K. Ackerstaff et al. (HERMES Collaboration), *Flavor decomposition of the polarized quark distributions in the nucleon from inclusive and semi-inclusive deep- inelastic scattering*, Phys. Lett. **B464**, 123 (1999).

[HERMES:99c]  K. Ackerstaff et al. (HERMES Collaboration), *Observation of a coherence length effect in exclusive $\rho^0$ electroproduction*, Phys. Rev. Lett. **82**, 3025 (1999).

[HERMES:00a]  K. Ackerstaff et al. (HERMES Collaboration), *Exclusive leptoproduction of $\rho^0$ mesons on hydrogen at intermediate W values*, Eur. Phys. Jour. **C17**, 389 (2000).

[HERMES:00b]  K. Ackerstaff et al. (HERMES Collaboration), *Nuclear effects on R = sigma(L)/sigma(T) in deep inelastic scattering*, Phys. Lett. **B475**, 386 (2000).

[HERMES:00c]  A. Airapetian et al. (HERMES Collaboration), *Measurement of the spin asymmetry in the photoproduction of pairs of high p(T) hadrons at HERMES*, Phys. Rev. Lett. **84**, 2584 (2000).

[HP:93]  R. Horisberger and D. Pitzl, *A novel readout chip for silicon strip detectors with analog pipeline and digitally controlled analog signal processing*, Nucl. Instrum. Meth. **A326**, 92 (1993).

[IER:97]  G. Ingelman, A. Edin and J. Rathsman, *LEPTO 6.5: A Monte Carlo generator for deep inelastic lepton - nucleon scattering*, Comput. Phys. Commun. **101**, 108 (1997).

[Kra:76]  F. Krautschneider, *Photoproduction of negative Pi–mesons between 900 MeV and 1800 MeV*, Dissertation, Universität Bonn, 1976.

[MIC:97]  MICRON, *Semiconductors data sheet*, 1997.

[MSS:97]  W. Melnitchouk, M. Sargsian and M. I. Strikman, *Probing the origin of the EMC effect via tagged structure functions of the deuteron*, Z. Phys. **A359**, 99 (1997).

[MST:94]  W. Melnitchouk, A. W. Schreiber and A. W. Thomas, *Deep inelastic scattering from off-shell nucleons*, Phys. Rev. **D49**, 1183 (1994).

[MT:96]  W. Melnitchouk and A. Thomas, *Neutron/Proton Structure Function Ratio at Large $x$*, Phys. Lett. **B337**, 11 (1996).

[NMC:97]  M. Arneodo et al. (NMC Collaboration), *Measurement of the proton and deuteron structure functions, $F_2^p$ and $F_2^d$, and of the ratio $\sigma_L/\sigma_T$*, Nucl. Phys. **B483**, 3 (1997).

[NP:84]  O. Nachtmann and H. J. Pirner, *Color conductivity in nuclei and the EMC effect*, Z. Phys. **C21**, 277 (1984).

[Par:96]     Particle Data Group, *Passage of particles through matter*, Phys. Rev. D 54, 1251 (1996).

[PTG:94]     Programming-Techniques-Group, *ADAMO – Entity-Relationship programming system, Version 3.3*, ECP Division, CERN, Geneva, 1994.

[Sak:60]     J. J. Sakurai, *Theory of strong interactions*, Annals Phys. 11, 1 (1960).

[Sim:96a]    S. Simula, *Semi-Inclusive Deep Inelastic Scattering off the Deuteron and the Neutron to Proton Structure Function Ratio*, Phys. Lett. B387, 245 (1996).

[Sim:96b]    S. Simula, *Tagged nuclear structure functions with HERMES*, nucl-th/9608056, 1996.

[ST:64]      A. A. Sokolov and I. M. Ternov, *On Polarization and spin effects in the theory of synchrotron radiation*, Phys. Dokl. 8, 1203 (1964).

[Ste:98a]    J. Steijger, Private Communication, 1998.

[Ste:98b]    J. Steijger, *Noise from Erlangen*, Internal Report, 1998.

[Sto:99]     U. Stoesslein, Private Communication, 1999.

[vB$^+$:98]   M. van Beuzekom et al., *A silicon micro-strip telescope for the HERMES experiment: A design study*, Nucl. Instr. Meth. A409, 255 (1998).

[vdS:99]     G. van der Steenhoven, Private Communication, 1999.

[VGG:98]     M. Vanderhaeghen, P. A. M. Guichon and M. Guidal, *Hard electroproduction of photons and mesons on the nucleon*, Phys. Rev. Lett. 80, 5064 (1998).

[VGG:99]     M. Vanderhaeghen, P. A. M. Guichon and M. Guidal, *Deeply virtual electroproduction of photons and mesons on the nucleon: Leading order amplitudes and power corrections*, Phys. Rev. D60, 094017 (1999).

[Vin:96]     M. Vincter, Private Communication, 1996.

[VM:98]      M. Vanttinen and L. Mankiewicz, *Exclusive J/Psi photoproduction and gluon polarization*, Phys. Lett. B440, 157 (1998).

[Wie:98]     M. Wiesmann, *Messungen an einem Siliziumdetektor für das HERMES-Experiment*, Diplomarbeit, Universität Erlangen-Nürnberg, 1998.

# Lebenslauf

**Persönliche Daten:**

Name:                   Klaus Fiedler
Geboren:                2. Mai 1971 in München
Staatsangehörigkeit:    deutsch
Familienstand:          ledig

**Schulbildung:**

09/1977 – 08/1980       Adalbert–Stifter–Grundschule Fürth
                        Überspringen der 2. Jahrgangsstufe

09/1980 – 06/1989       Helene–Lange–Gymnasium Fürth

06/1989                 Abschluß: Allgemeine Hochschulreife (Note 1,0)
07/1989                 Sonderprüfung, Verleihung eines Stipendiums der
                        bayerischen Hochbegabtenförderung

**Zivildienst:**

11/1991 – 10/1992       Mobiler Sozialer Hilfsdienst der Arbeiterwohlfahrt Fürth:
                        Individuelle Betreuung von Multiple–Sklerose–Patienten

**Studium:**

11/1989 – 10/1991 und   Studium der Physik (Diplom) an der Universität
11/1992 – 11/1995       Erlangen–Nürnberg
                        Schwerpunkt: Experimentalphysik
                        Nebenfach: Biophysik

10/1991                 Vordiplom (Note 1,25)
09/1994 – 10/1995       Diplomarbeit am Forschungszentrum DESY in Hamburg
11/1995                 Abschluß als Diplom–Physiker (Univ.) (Note 1,26)

seit 04/1996            Wissenschaftlicher Mitarbeiter am Physikalischen Institut
                        der Universität Erlangen–Nürnberg